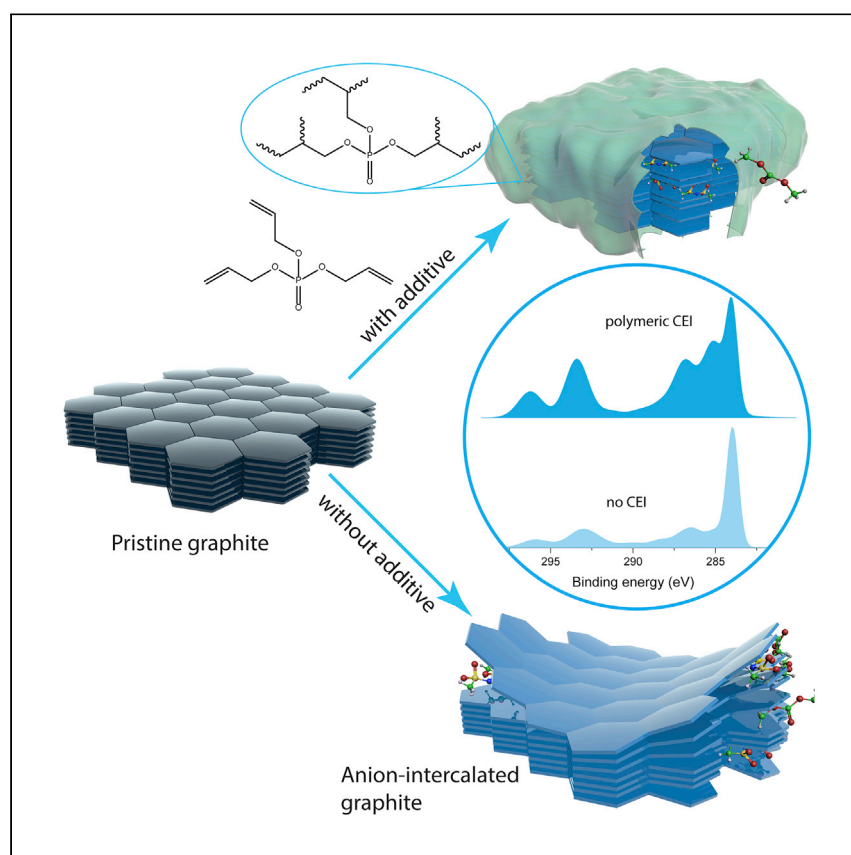


# Article

## A polymeric cathode-electrolyte interface enhances the performance of MoS<sub>2</sub>-graphite potassium dual-ion intercalation battery



A dual-ion battery operates at unusually high voltage, which is needed to intercalate anions in a graphite cathode. Asfaw et al. explore strategies to create more stable electrode-electrolyte interfaces in an effort to design potassium-based MoS<sub>2</sub>-natural-graphite dual-ion battery with high coulombic efficiency and long cycle life.

Habtom Desta Asfaw, Antonia Kotronia

habtom.desta.asfaw@kemi.uu.se

### Highlights

Design principle for high-performance MoS<sub>2</sub>-graphite dual-ion battery is proposed

Impact of electrolyte additives on the negative and positive electrodes is investigated

Triallyl phosphate is used to generate a polymeric CEI on graphite cathode

MoS<sub>2</sub> with pre-formed SEI layer ensures stable cycling and high coulombic efficiency

## Article

# A polymeric cathode-electrolyte interface enhances the performance of MoS<sub>2</sub>-graphite potassium dual-ion intercalation battery

Habtom Desta Asfaw<sup>1,2,\*</sup> and Antonia Kotronia<sup>1</sup>

## SUMMARY

Anion intercalation in the graphite cathode of a dual-ion battery (DIB) occurs at unusually high voltage ( $>4.5$  V  $K^+/K$ ). This exacerbates electrolyte degradation and corrosion of Al current collectors, leading to poor coulombic efficiency (CE), typically  $<90\%$ , and short cell life as a result. These limitations can be mitigated if a stable cathode-electrolyte interface layer (CEI) can form on the graphite electrode. In this study, we demonstrate that the performance of a potassium-based DIB can be improved with a triallyl phosphate (TAP) monomer added in 6 m  $KN(SO_2CF_3)_2$  (KTFSL)-dimethyl carbonate (DMC) electrolyte. The TAP additive forms a stable polymeric CEI on the graphite particles and thus increases the CE of the cell to 97%–99%. Together with MoS<sub>2</sub>-negative electrodes with a pre-formed solid electrolyte interphase (SEI) layer, the DIB concept has been shown to offer specific capacities from  $\sim 40$  to 80 mAh  $g^{-1}$  with an average discharge voltage of 3.7 V.

## INTRODUCTION

Emerging battery technologies, such as potassium dual-ion batteries (KDIBs), are considered cost effective and promising for use in stationary and large-scale energy storage applications.<sup>1–3</sup> This is partly due to the relative abundance of potassium-containing minerals and the redox potential of potassium ( $-2.93$  V versus standard hydrogen electrode [SHE]), which is comparable to that of lithium ( $-3.04$  versus SHE) and is suited for constructing high-energy batteries.<sup>4,5</sup> To date, KDIBs have been demonstrated to offer specific capacities reaching  $\sim 50$ – $100$  mAh  $g^{-1}$  and cell voltages averaging  $\sim 4.5$ – $4.7$  V versus  $K^+/K$ .<sup>1–3,6–8</sup> Recently, Yang et al.<sup>9</sup> reported that KDIBs with up to 232 mAh  $g^{-1}$  capacity can be realized using locally ordered graphitic carbon for anion storage. Thus, they are anticipated to complement current energy storage systems based on lithium-ion batteries in applications wherein stationary and distributed energy storage is desired. Most KDIBs utilize potassium metal, graphite, or alloys in the negative electrodes,<sup>3,6,8,10,11</sup> which pose safety risks because of aggressive reactions with the electrolytes and dendrite formation.<sup>4</sup> Substituting these materials with layered transition metal dichalcogenides (TMDCs) can potentially render KDIBs safer for widespread applications.<sup>12</sup> The major interest in TMDCs lies in their van der Waals interlayer gaps that can readily be enlarged to reversibly store large ions, such as  $K^+$ .<sup>4,13</sup> In contrast to graphite, most TMDCs operate above 0.5 V versus  $K^+/K$ , which helps minimize electrolyte degradation and avoid K metal plating, and thus, stable performance can be ensured.<sup>13–16</sup> A classic example of TMDCs widely studied as a host for potassium ions is MoS<sub>2</sub> (interlayer gap  $\sim 6.15$  Å), which can reversibly deliver up to 80 mAh  $g^{-1}$ , corresponding to the formation of

<sup>1</sup>Department of Chemistry, Ångström Laboratory, Uppsala University, Lägerhyddsvägen 1, Uppsala 75121, Sweden

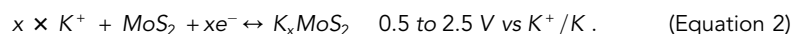
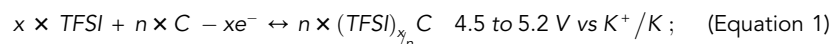
<sup>2</sup>Lead contact

\*Correspondence: [habtom.desta.asfaw@kemi.uu.se](mailto:habtom.desta.asfaw@kemi.uu.se)  
<https://doi.org/10.1016/j.xcrp.2021.100693>

K<sub>0.5</sub>MoS<sub>2</sub>.<sup>15</sup> Few examples of DIBs using TMDC electrodes exist in the literature. For instance, an MoS<sub>2</sub>-graphite sodium DIB reported by Zhu et al.<sup>17</sup> could provide a specific capacity of 65 mAh g<sup>-1</sup> at 100 mA g<sup>-1</sup> within 1–4 V. Similarly, TiSe<sub>2</sub> was used as a host for sodium ions in a full-cell DIB for which up to 80 mAh g<sup>-1</sup> was obtained at 100 mA g<sup>-1</sup> in the voltage range 1.5–3.5 V versus Na<sup>+</sup>/Na.<sup>18</sup> Besides, the interlayer gap in TMDCs can be further expanded to enhance intercalation kinetics. For instance, Bellani et al.<sup>19</sup> demonstrated that a lithium-based DIB consisting of few layers WS<sub>2</sub> nanosheets in the negative electrode could deliver 80 mAh g<sup>-1</sup> at 100 mA g<sup>-1</sup>.

Common prototypes of KDIBs often utilize highly concentrated electrolytes (HCEs) of KN(SO<sub>2</sub>F)<sub>2</sub> (KFSI) and KN(SO<sub>2</sub>CF<sub>3</sub>)<sub>2</sub> (KTFSI) salts as high oxidative stability is required for reversible anion intercalation into graphite occurring above 4.5 V versus K<sup>+</sup>/K.<sup>1,11</sup> However, such HCEs do not form stable cathode-electrolyte interface (CEI) layer, which is key to the design of KDIBs with high coulombic efficiency and long cycle life by suppressing Al dissolution and graphite exfoliation over extended cycles. Thus, it is necessary to formulate electrolyte systems that incorporate salt and solvent additives that help generate stable CEI layer on graphite.<sup>20</sup> Various types of additives have been proposed for the enhancement of coulombic efficiency and cycling life in lithium DIBs. Wang et al.<sup>21</sup> reported recently that lithium difluoro(oxalate)borate salt additives in 3 M LiPF<sub>6</sub> could enhance stability of the CEI layer and cells retained nearly 88% of the capacity after 4,000 cycles at 0.5 A g<sup>-1</sup>. Other additives used along with HCEs include fluoroethylene carbonate,<sup>22</sup> tris(hexafluoro-iso-propyl)phosphate,<sup>23</sup> and ethylene sulfite.<sup>24</sup>

This paper reports the design of MoS<sub>2</sub>-natural-graphite KDIB enabled by a polymeric CEI layer generated *in situ* on graphite particles. An electrolyte formulation based on 6 m (molal = mol kg<sup>-1</sup>) KTFSI in dimethyl carbonate (DMC) with 1–10 wt % triallyl phosphate (TAP) monomer additive was used to achieve stable performance. It has been documented that TAP could improve the cycle life and coulombic efficiency of Li(Ni<sub>0.4</sub>Mn<sub>0.4</sub>Co<sub>0.2</sub>)O<sub>2</sub>-graphite and Li(Ni<sub>0.6</sub>Mn<sub>0.2</sub>Co<sub>0.2</sub>)O<sub>2</sub>-graphite cells at high voltages and high temperatures.<sup>25–27</sup> The polymeric layer formed in such devices can be employed to enhance the CEI in KDIBs. To avert the impact of the solid electrolyte interphase (SEI) formation at the negative electrode, a stable SEI was pre-formed on the MoS<sub>2</sub> prior to MoS<sub>2</sub>-graphite assembly by cycling it in 1 M KTFSI in DMC, dimethoxy ethane (DME), and ethylene carbonate solvent (EC) mixtures. In a typical MoS<sub>2</sub>-natural-graphite KDIB, the cell reactions occurring during charging entail TFSI anion intercalation into graphite and K<sup>+</sup> intercalation in MoS<sub>2</sub> as shown below:



In Equations 1 and 2, the symbols *n* and *x* indicate the number of moles of graphite and TFSI anion (and K<sup>+</sup>) involved in the reaction, respectively. The formulated electrolytes were tested in prototype pouch cells cycled at room temperature at different specific currents. To determine the impact of the polymerizing additive TAP on the CEI layer, electrochemical impedance spectroscopy (EIS), X-ray photoelectron spectroscopy (XPS), and scanning electron microscopy coupled with energy-dispersive spectroscopy (SEM-EDX) were conducted on cycled electrodes. Further

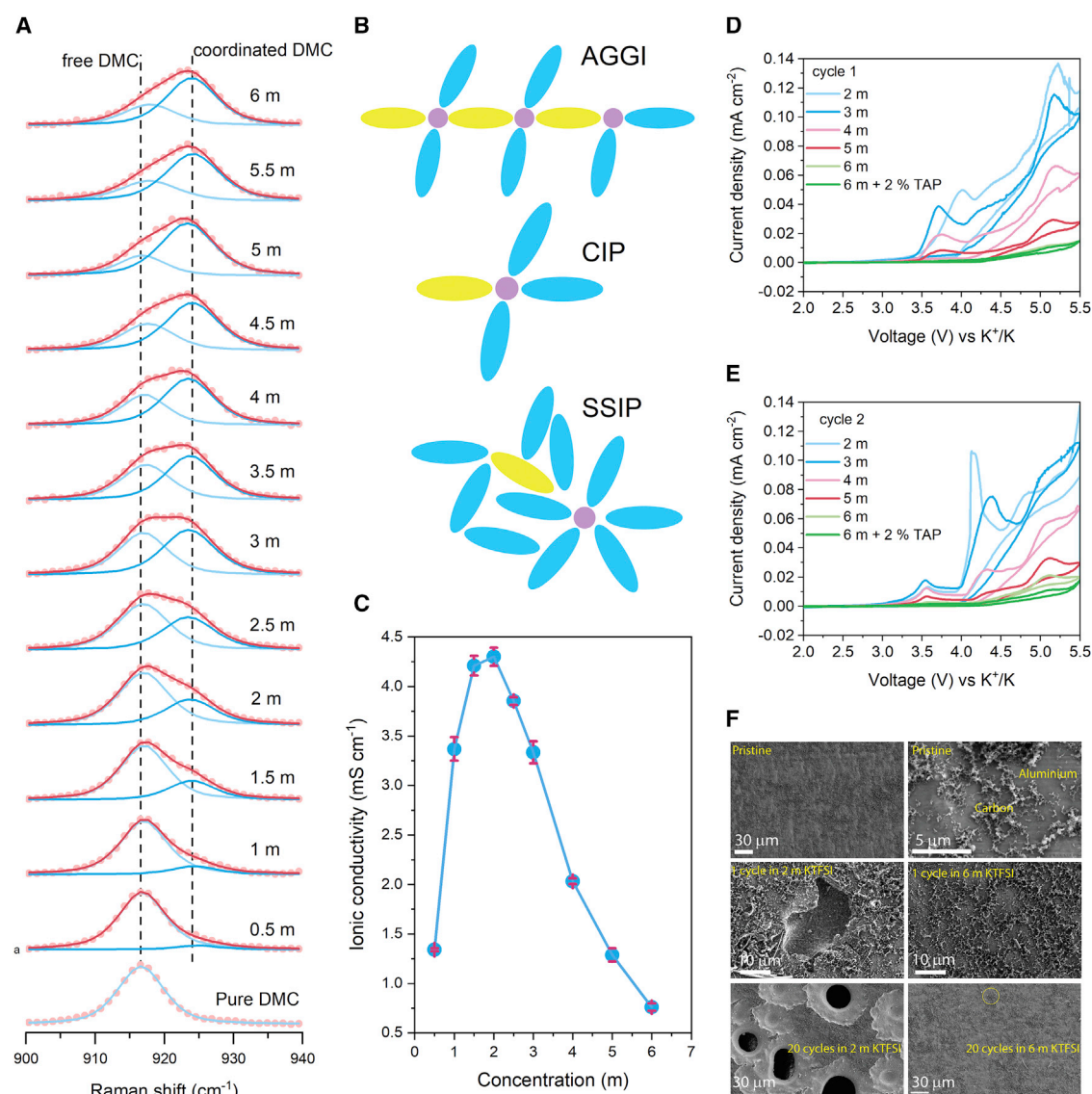


**Figure 1. Concentrated electrolytes suppress Al dissolution in addition to provision of ions for energy storage**

(A–F) Solvent-ion coordination and electrochemical stability of Al current collectors. (A) The Raman spectra of pure DMC solvent and after addition of varying amounts of KTFSI salt (0.5–6 m concentration), see also Figure S1; (B) illustration of the ion-solvent solvate species expected in the electrolytes; (C) ionic conductivities for selected electrolytes averaged over five measurements and given along with error bars representing the respective standard deviations; (D) the first cyclic voltammograms at 1 mV s<sup>-1</sup>, showing anodic stability of electrolytes on Al current collectors; (E) the second cyclic voltammograms showing anodic stability of electrolytes on Al current collectors (see also Figures S3 and S6); and (F) SEM images of C-coated Al electrodes after the 1<sup>st</sup> and 20<sup>th</sup> CVs in 2 m and 6 m KTFSI in DMC (see also Figures S4 and S5).

investigation was carried out using *ex situ* Raman spectroscopy to assess whether electrochemical cycling affects the bulk structure of the graphite and MoS<sub>2</sub> active materials.

## RESULTS AND DISCUSSION

### Concentrated electrolytes suppress Al dissolution in addition to provision of ions for energy storage

Raman spectroscopy was used to track ion coordination in the electrolytes consisting of KTFSI salt in DMC solvent. With a symmetry point group of C<sub>2v</sub>, a DMC molecule has 30 normal modes (all being Raman active) with the irreducible symmetry

representation given as  $10A_1 + 5A_2 + 9B_1 + 6B_2$ .<sup>28,29</sup> As shown in Figures 1 and S1, it exhibits particularly intense bands at  $\sim 915\text{ cm}^{-1}$  ( $A_1$  symmetry) and  $\sim 516\text{ cm}^{-1}$  ( $A_1$  symmetry) due to  $\text{H}_3\text{C}-\text{O}$  stretching vibrations and  $\text{O}-(\text{C}=\text{O})\text{O}$  bending (deformation) modes, respectively.<sup>28,30</sup> After salt addition, the bands shifted to higher frequencies (see Figures 1A and S1) due to solvent-ion coordination to form solvent-separated ion pairs (SSIPs), contact ion pairs (CIPs), and aggregated ions (AGGIs), as illustrated in Figure 1B.<sup>31,32</sup> The ionic conductivity was observed to increase with increasing salt concentration until 2 m, where it peaked at  $\sim 4.2\text{ mS cm}^{-1}$  (Figures 1C and S2). The subsequent decline in the conductivity could be correlated to the formation of salt aggregates in which the mobility of charge carriers was impeded. In addition, the impact of electrolyte salt concentration (2, 3, 4, 5, 6 m, and 6 m KTFSI in DMC with 2% TAP) on the Al current collector and solvent decomposition was verified using cyclic voltammetry (CV), as summarized in Figures 1D, 1E, and S3. The areal current at 5.5 V versus  $\text{K}^+/\text{K}$  decreased progressively with increasing salt concentration. Such a trend could be attributed to the lower solubility of  $\text{Al}(\text{TFSI})_3$  in more concentrated electrolytes and the retardation of DMC decomposition due to coordination of its lone pairs to salt cations.<sup>31</sup> For 2 and 6 m KTFSI-DMC electrolytes, for instance, the corresponding currents were  $\sim 0.14\text{ mA cm}^{-2}$  and  $\sim 0.01\text{ mA cm}^{-2}$  (an order of magnitude lower). Cycling in the 2 m electrolyte caused structural damage to the Al current collector in the form of pitting over 20 cycles as shown in Figures 1F, S4, and S5. In contrast, Al electrodes cycled in 6 m KTFSI-DMC appeared intact during the first cycle CV and only few pittings were observed after 20 cycles, demonstrating that Al dissolution is only kinetically suppressed, and it can potentially be exacerbated over long-term cycling. The anodic stability of the electrolytes was additionally studied using glassy carbon electrodes. The CVs shown in Figure S6 demonstrated that the stability of the electrolytes generally increased with increasing salt concentration. Thus, the most concentrated electrolyte, 6 m KTFSI in DMC, was selected in this study for use in KDIBs.

### Pre-formed solid electrolyte interphase on MoS<sub>2</sub> enhances its performance in concentrated electrolytes

In this study, crystalline flakes of MoS<sub>2</sub> and natural graphite (Figures S7 and S8) are used as hosts for  $\text{K}^+$  and TFSI anions in the design of a KDIB. The characteristic galvanostatic curves in Figure 2A show that most of the electrochemical intercalation and extraction processes in MoS<sub>2</sub> occurred within 0.5–1.6 V range. Previous studies<sup>15,33</sup> have indicated that conversion reactions dominated below 0.5 V, for which higher specific capacities can be obtained but with considerable irreversibility and lower initial coulombic efficiency (iCE).

Only the intercalation process was utilized in this study. The intercalation capacity at  $10\text{ mA g}^{-1}$  for the first cycle was  $\sim 96\text{ mAh g}^{-1}$  with an iCE of 79%. The CE increased to  $\sim 99\%$  in the subsequent cycles while the specific capacity stabilized at  $78\text{ mAh g}^{-1}$ . In contrast, in the 6 m KTFSI-DMC electrolyte, the electrode exhibited sharp capacity fading with only 19% capacity retention over 20 cycles (Figure 2B). The performance degradation could be due to an unabated electrolyte degradation as no stable SEI formed during the initial cycle. After 10 formation cycles in 1 M KTFSI-DMC-DME-EC electrolyte, the electrodes were rinsed in DME and cycled in the concentrated electrolyte and more stable cycling performance was achieved. The observation demonstrated that a stable SEI was a requisite to improve the reversibility of potassium intercalation in MoS<sub>2</sub> in concentrated electrolytes where no SEI-forming solvents are employed. In addition, *post mortem* SEM characterization shown in Figure S9 suggested that interlayer expansion and particle size reduction occurred in the course of cycling. In contrast to the initial cycle, remarkable

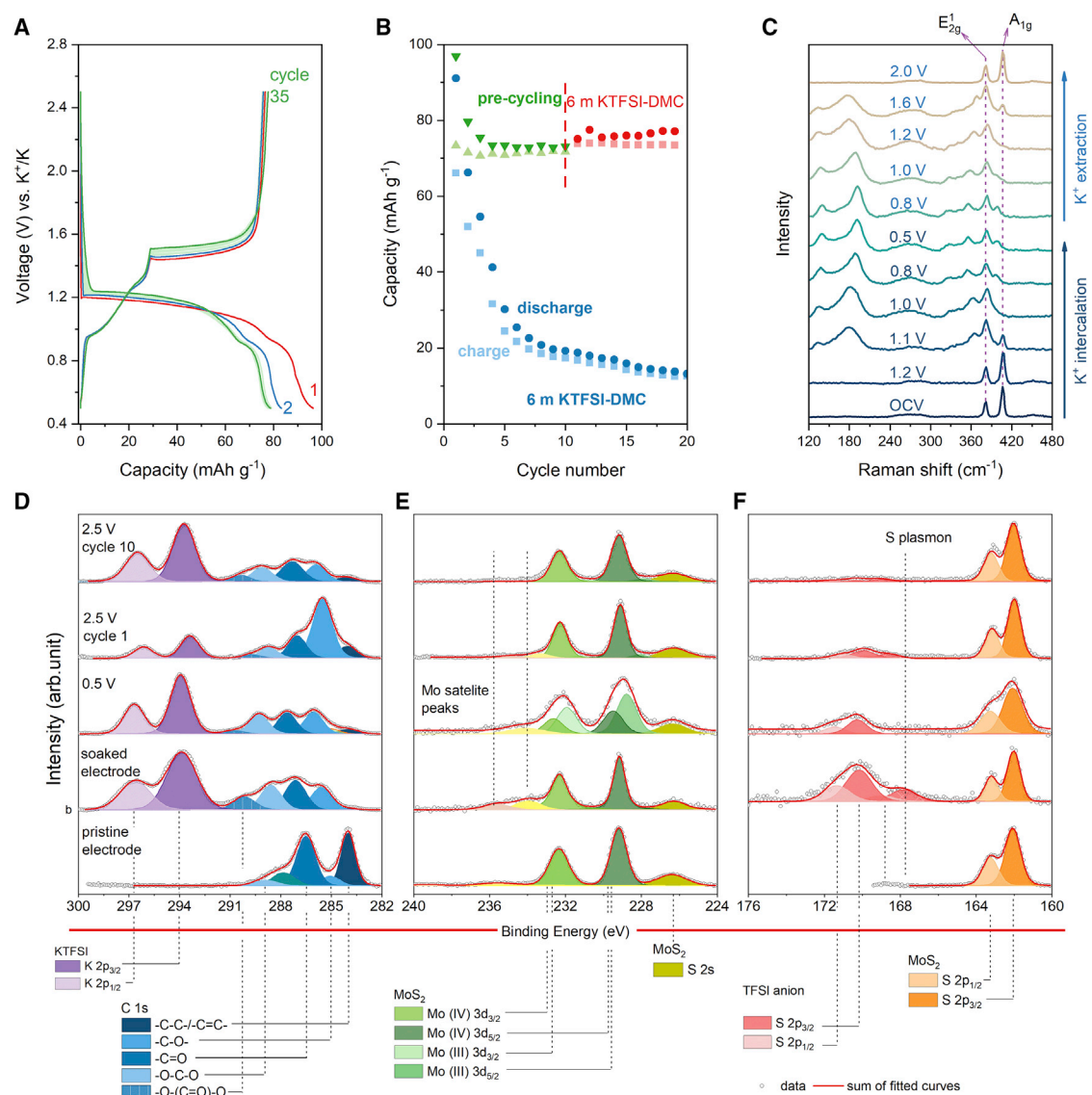


**Figure 2. Pre-formed solid electrolyte interphase on MoS<sub>2</sub> enhances its performance in concentrated electrolytes**

(A–F) Electrochemical K<sup>+</sup> intercalation and extraction in MoS<sub>2</sub> in 1 M KTFSI DMC-DME-EC: (A) galvanostatic voltage-capacity curves measured at 10 mA g<sup>−1</sup> showing the K<sup>+</sup> intercalation in MoS<sub>2</sub> versus K<sup>+</sup>/K; (B) impact of pre-cycling in SEI-forming electrolyte on the cycling performance of MoS<sub>2</sub> in concentrated electrolytes; (C) *in situ* Raman spectroscopy showing changes in the main vibrational modes and appearance or disappearance of new bands at different state-of-charge; and (D–F) XPS showing the nature of surface components on MoS<sub>2</sub> electrodes before and after cycling (see also Figure S10).

exfoliation took place as shown for the 10<sup>th</sup> cycle, which could be caused by solvent co-intercalation as potassium ions entered the interlayer gaps. The Raman spectrum of bulk MoS<sub>2</sub> (Figures 2C and S8C) exhibited characteristic Raman scattering modes located around 382 cm<sup>−1</sup> and 407 cm<sup>−1</sup>. The former arises from in-plane vibration mode of two sulfur atoms opposite to each other with E<sub>2g</sub><sup>1</sup> symmetry, and the latter is due to out-of-plane vibration of two sulfur atoms with A<sub>1g</sub> symmetry.<sup>34–37</sup> As shown in Figure 2C, the modes shifted in frequency and new ones emerged during K<sup>+</sup> intercalation, specially at 1.1 V and below. It is interesting to note that the E<sub>2g</sub><sup>1</sup> mode at 383 cm<sup>−1</sup> in MoS<sub>2</sub> shifted slightly to higher frequency, while the A<sub>1g</sub> mode underwent red shift progressively from 407 to 397 cm<sup>−1</sup> at 0.5 V. The

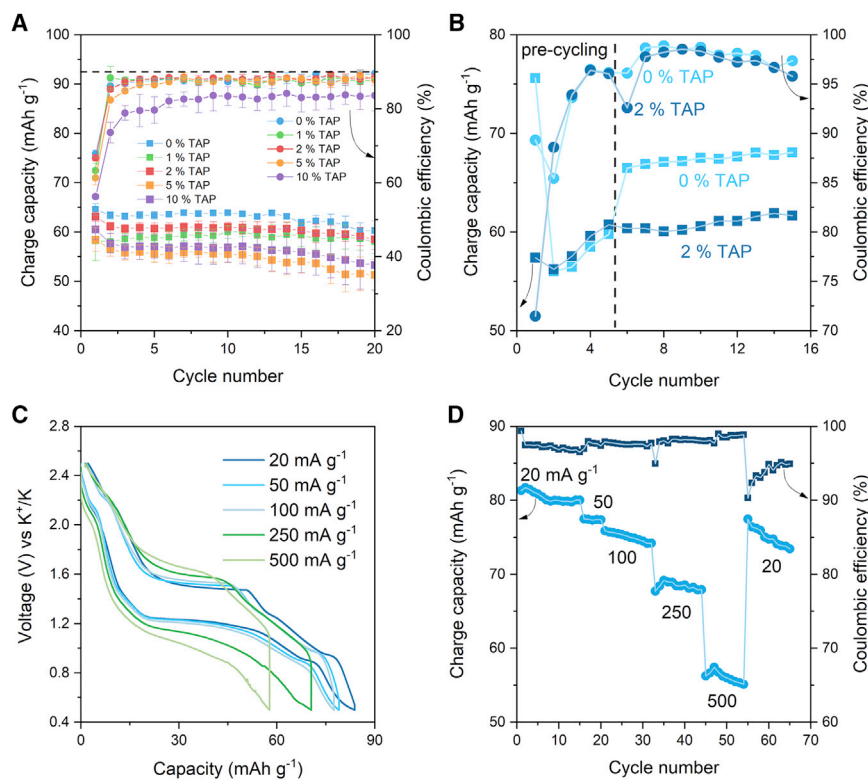


**Figure 3. The effect of triallyl phosphate additives on K<sup>+</sup> cycling in MoS<sub>2</sub> electrodes in concentrated electrolytes**

(A–D) (A) The influence of various amounts of TAP additives on the capacity and coulombic efficiency of K<sup>+</sup> intercalation into MoS<sub>2</sub> electrodes (three measurements were done at 20 mA g<sup>-1</sup> for each electrolyte, and the average values are given along with the standard deviations), (B) impact of cycling MoS<sub>2</sub> with pre-formed SEI layer in concentrated electrolytes with and without TAP additive (see also Figures S11–S18), (C) the galvanostatic curves (for 3-electrode cells) for K<sup>+</sup> intercalation and extraction in pre-cycled MoS<sub>2</sub> electrodes performed at 20–500 mA g<sup>-1</sup> in 6 m KTFSI in DMC with 2% TAP additive, and (D) long-term rate capability data and coulombic efficiency related to (C).

softening of the A<sub>1g</sub> mode suggested reduction in the interlayer van der Waals forces, which was indicative of expanding interlayer gaps, leading to the formation of the single trilayer 1T-MoS<sub>2</sub> phase with the Mo coordination changing from trigonal prismatic to octahedral.<sup>36,38,39</sup> Upon full de-potassiation to 2.5 V, the original structure of MoS<sub>2</sub> was regained, as evidenced by the characteristic modes reappearing at the initial Raman shifts.

Analysis of the cycled electrodes using XPS verified that the surface composition changed during potassium intercalation and at the end of the 1<sup>st</sup> and 10<sup>th</sup> cycles, as shown in Figures 2D–2F and S10. The C 1s spectra displayed the progressive increase in the intensity of oxygen-containing organic compounds (–C–O–, –C=O, and CO<sub>3</sub><sup>2-</sup> functional groups) and the concomitant decrease in the intensity of the sp<sup>3</sup>-hybridized carbon from the conductive additive as it was buried underneath decomposition products. The surface coverage was reminiscent of the SEI film that forms on graphite electrodes employed in lithium-ion batteries and persisted even after full de-potassiation at the 1<sup>st</sup> and 10<sup>th</sup> cycles. In the pristine electrode, the sulfur species pertaining to the peak at ~162 eV originated entirely from MoS<sub>2</sub>, and in the cycled electrodes, additional sulfur species from the electrolyte were detected at higher binding energies (~170 eV).<sup>40</sup> Further insight can be gained on closer inspection

of the Mo 3d spectra, which exhibited peaks centered around  $\sim 229$  eV.<sup>40</sup> The additional Mo 3d doublets originated from the 1T-MoS<sub>2</sub> (formed due to reduction of 2H-MoS<sub>2</sub> upon K<sup>+</sup> intercalation at 0.5 V). At the end of the de-intercalation process of the 1<sup>st</sup> and 10<sup>th</sup> cycles, the intensity of the additional peaks diminished considerably, hinting at the full reversibility of K<sup>+</sup> intercalation. Next, the impact of the TAP additives (0, 1, 2, 5, and 10 wt %) on the potassium-ion storage capacity, CE, and rate performance of the MoS<sub>2</sub> electrodes was assessed and summarized in Figure 3. On average, the specific capacity (Figure 3A) and coulombic efficiency (Figure 3B) values decreased with increasing amount of the TAP additives. Worse performance was observed particularly in the electrolytes containing 5% and 10% TAP; this could be due to excessive buildup of polymeric products on the surface of the electrodes as can be seen in the SEM images (see Figure S11), whereas the Raman spectra (see Figure S12) indicated that the bulk structure of MoS<sub>2</sub> remained largely intact at the end of the intercalation-extraction cycles. In agreement with the data in Figure 2B, MoS<sub>2</sub> electrodes cycled in the SEI-forming electrolyte (5 cycles in 1 M KTFSI in DMC-DME-EC) were less affected by the TAP additives and could achieve higher CE as shown in Figure 3B. This conclusion is supported by the XPS data given in Figures S13–S15 for pristine MoS<sub>2</sub> electrodes cycled in concentrated electrolytes and those for pre-cycled MoS<sub>2</sub> electrodes tested in the concentrated electrolyte with and without the TAP additive (see Figures S16–S18). The SEI layer remained stable after 15 charge-discharge cycles in the concentrated electrolytes as evidenced by the peaks, which were similar to those observed in Figures 2D–2F. It can be concluded that the TAP additive should not exceed 2% and pre-cycling in an SEI-forming electrolyte was needed to ensure optimum K<sup>+</sup> storage performance. Furthermore, the rate capability of pre-cycled MoS<sub>2</sub> electrodes was investigated in 6 m KTFSI-DMC electrolyte with a 2% TAP additive. As can be seen in Figures 3C and 3D, the electrodes exhibited good capacity retention as the current increased from 20 to 500 mA g<sup>−1</sup>.

### A 3.7 V MoS<sub>2</sub>-graphite KDIB concept is demonstrated

As illustrated in Figure 4A, on charge, the KDIB involved K<sup>+</sup> intercalation in MoS<sub>2</sub> and TFSI intercalation in graphite, and the reverse on discharge. The characteristic galvanostatic curves associated with both electrode materials in a 3-electrode KDIB are shown in Figure 4B. Accordingly, most of the intercalation process of TFSI occurred in the 4.5–5.2 V versus K<sup>+</sup>/K range. The plateaus in the galvanostatic curves displayed the staging behavior characteristic of TFSI anion intercalation in natural graphite. These features were further indicated as peaks (charge: 4.5; 4.6; 4.65; 4.79; 4.87; 5; and 5.15 V and discharge: 5.1; 4.91; 4.85; 4.73; 4.6; and 4.3 V) in the differential capacity plots for the first two cycles (Figure 4C). With an average discharge voltage of  $\sim 3.7$  V and a capacity of  $\sim 64$  mAh g<sup>−1</sup>, the graphite-MoS<sub>2</sub> KDIB could provide a specific energy  $> 230$  Wh kg<sup>−1</sup> with respect to the mass of graphite. The CVs provided in Figure S19 demonstrated that the MoS<sub>2</sub>-natural-graphite cell involved different redox processes as indicated by the multiple peaks attributable to anion intercalation in graphite and K<sup>+</sup> intercalation in MoS<sub>2</sub> during charge and removal of the ions when discharging the cell. The most prominent redox processes occurred at 3.5, 3.9, 4.1, and 4.3 V during charging and 4.1, 3.9, 3.6, and 3.3 V during discharging.

*Ex situ* Raman spectra of the electrodes cycled to various charge and discharge states are given in Figure 4D and are used to assess the reversibility of the TFSI intercalation in graphite. The pristine natural graphite had a sharp band at  $\sim 1,580$  cm<sup>−1</sup> assigned to the G band (E<sub>2g2</sub> mode) and second-order scattering (2D) bands at 2,679 and 2,719 cm<sup>−1</sup>. In the course of TFSI intercalation, the defect (D) band appeared

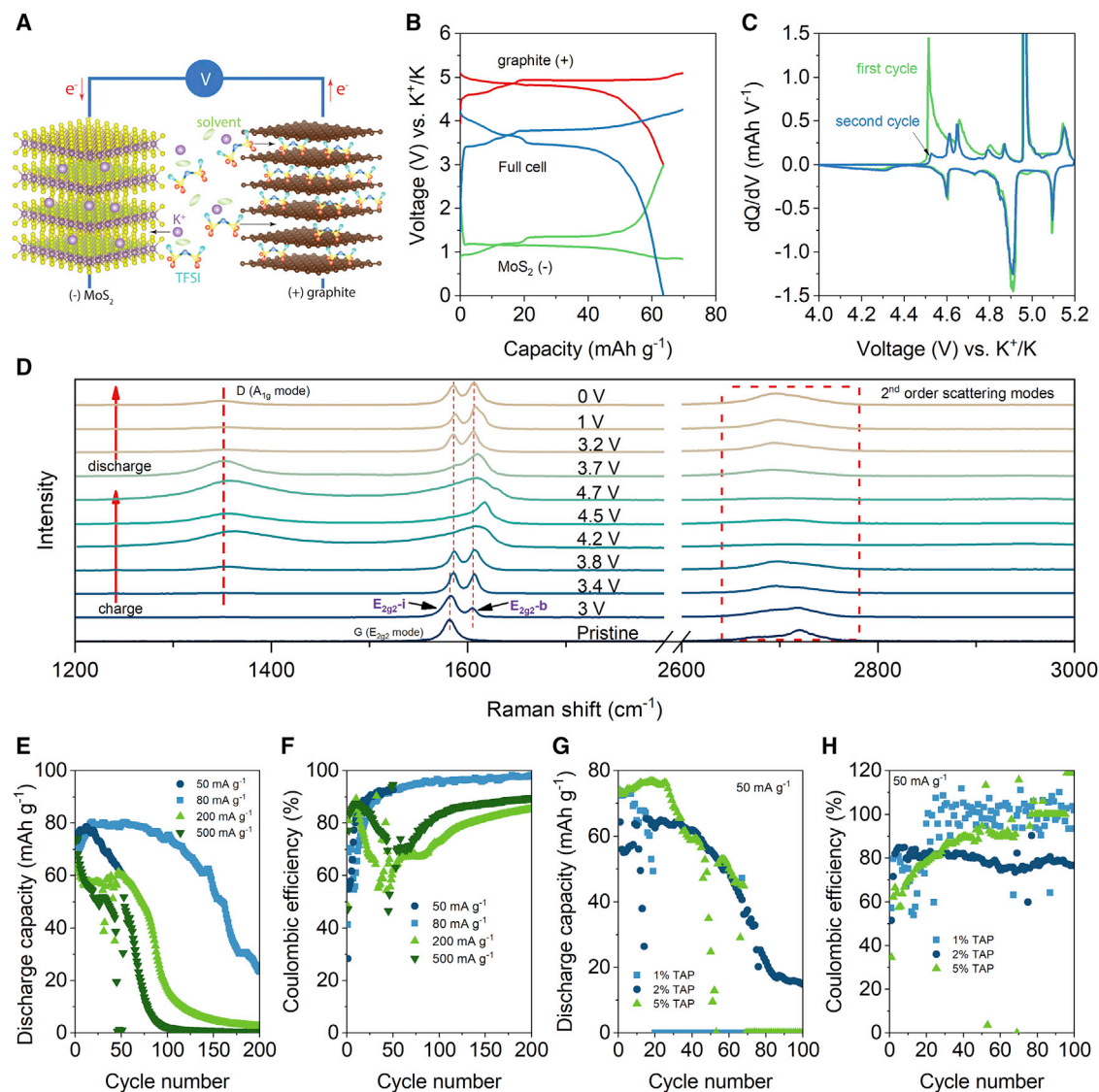


**Figure 4. A 3.7 V MoS<sub>2</sub>-graphite KDIB concept is demonstrated**

(A–H) (A) A schematic illustration of the TFSI anion intercalation into graphite and K<sup>+</sup> intercalation into MoS<sub>2</sub>; (B) typical galvanostatic curves at 50 mA g<sup>-1</sup>, showing the voltage-capacity relationships in a 3-electrode cell consisting of natural graphite positive electrode and MoS<sub>2</sub> negative electrode (see also Figure S19); (C) the differential capacity plots corresponding to the galvanostatic curves of the working electrode in (B); (D) *ex situ* Raman spectra of anion intercalated graphite at various voltages during charge and discharge steps (see also Figures S20–S23); and (E–H) discharge capacities and associated coulombic efficiencies for galvanostatic cycling tests on the dual-ion battery using MoS<sub>2</sub> electrode, which lacked stable SEI layer in electrolytes with and without TAP additive.

between 1,340 and 1,354 cm<sup>-1</sup>, signifying the onset of structural disorder. Characteristic of anion-intercalated graphite, the G band split into two bands corresponding to internal graphene layers that remained unaffected by the intercalant (E<sub>2g2-i</sub>) and boundary graphene layers, which interacted with the intercalating TFSI through charge transfer process (E<sub>2g2-b</sub> mode).<sup>41</sup> The second band located at ~1,605 cm<sup>-1</sup> emerged around 3 V and increased in intensity as more anions were intercalated. Above 4.2 V, more drastic disorder was observed as more anions, and possibly solvent molecules, intercalated, causing interlayer expansion, buckling of the graphene layers, and turbostratic disorder. The corresponding XPS measurements (Figures S20 and S21) verified that the most distinctive changes occurred at 4.2 V and above

where additional peaks (especially in the N 1s and S 2p spectra) were observed, which could pertain to surface adsorbed and intercalated TFSI anions.<sup>20</sup> Upon subsequent de-intercalation processes at 3.8, 3.2, 1, and 0 V, the D band diminished in intensity continuously while the D' band (E<sub>2g2</sub>-b mode) persisted in intensity but shifted to lower wavenumbers, hinting at the presence of trapped anions or solvent molecules in the graphite electrode. *Ex situ* XRD (see Figure S22) performed on the graphite electrodes at fully intercalated state verified that the (002) peak shifted to lower angles as anticipated for anion-intercalated graphite compounds.<sup>42</sup> The XRD pattern in Figure S23 for the corresponding MoS<sub>2</sub> electrodes indicated that K<sup>+</sup> ions could be reversibly intercalated and de-intercalated as shown by the positions of the (002) peaks, which moved from  $2\theta \approx 14.4^\circ$  to  $10.6^\circ$  upon potassium intercalation and to  $14.3^\circ$  after full de-intercalation. It is worth noting that irreversible reactions at the negative electrode could result in entrapment of anions in graphite. Thus, it is indispensable to use MoS<sub>2</sub> electrodes with stable SEI layer pre-formed prior to cell assembly. In the KDIB using MoS<sub>2</sub> without pre-formed SEI (Figures 4E–4H), cycling at 50 mA g<sup>−1</sup> exhibited an iCE of ~30% with a specific capacity that increased from ~76 to ~79 mAh g<sup>−1</sup> over 12 cycles and decreased to ~60 mAh g<sup>−1</sup> after 50 cycles while the corresponding CE was ~93%. Similar trend was also observed for electrodes cycled at 80 mA g<sup>−1</sup>, where the iCE was ~40% and a maximum discharge capacity, ~80 mAh g<sup>−1</sup>, was attained after 20 cycles (the CE being ~80%). Over 100 cycles, the capacity dropped to 75 mAh g<sup>−1</sup> with a CE of ~96%. Only 23 mAh g<sup>−1</sup> was observed after 200 charge-discharge cycles. Increasing cycling currents to 200 and 500 mA g<sup>−1</sup> resulted in fast capacity fading and CEs that remained lower than 85% throughout the cycles. The specific capacities at 200 and 500 mA g<sup>−1</sup> decreased, respectively, from ~67 to ~17 mAh g<sup>−1</sup> and ~73 to ~2 mAh g<sup>−1</sup> over 100 cycles. Furthermore, cycling at 50 mA g<sup>−1</sup> in the presence of 1 to 5 wt % TAP additives exacerbated the capacity fading and worse CE values were observed, as displayed in Figures 4G and 4H. The lower CEs could point to the ill-behaved MoS<sub>2</sub> electrodes in the concentrated electrolyte as they lacked stable SEI layer, as discussed above, leading to structural damage due to exfoliation and conversion reactions expected when the voltage cutoff was forced to swing to below 0.5 V.

#### Pre-formed SEI layer on MoS<sub>2</sub> electrode and TAP additive improve both cycle life and CE

Various amounts of the TAP additive (1, 2, 3, 4, 5, and 10 wt %) were used along with MoS<sub>2</sub> electrodes (cycled 5 times at 20 mA g<sup>−1</sup> in SEI-forming electrolyte) to design full-cell KDIBs. Selected galvanostatic curves measured at 50 mA g<sup>−1</sup> are provided in Figures 5A–5C (see also Figure S24). It should be pointed out that the cells tested in the absence of additives exhibited comparatively larger voltage hysteresis in the galvanostatic cycles, which might be due to increased cell resistance or changes in the structure of the graphite electrode. Accordingly, the 1%–4% TAP delivered the most optimum performance during the first two cycles and while 1%–2% TAP were sufficient over long-term cycling. The electrodes pre-cycled at 10 mA g<sup>−1</sup> over 10 cycles were further used in the design of full-cell KDIBs. To determine the impact on the initial CE and extended cycling performance, pre-cycled MoS<sub>2</sub> electrodes with stable SEI layer were incorporated in full-cell KDIB using same electrolyte with and without additives as shown in Figures 5D and 5E. For galvanostatic tests at 50 mA g<sup>−1</sup> in the electrolyte without additive, the iCE increased from ~33% without pre-cycling to ~57% with surface-passivated MoS<sub>2</sub>. The discharge capacity stabilized over 10 cycles, reaching ~75 mAh g<sup>−1</sup> at 94% CE (in contrast to only ~68 mAh g<sup>−1</sup> and a CE of ~74% for MoS<sub>2</sub> without pre-cycling), thereby demonstrating the benefit of the MoS<sub>2</sub>

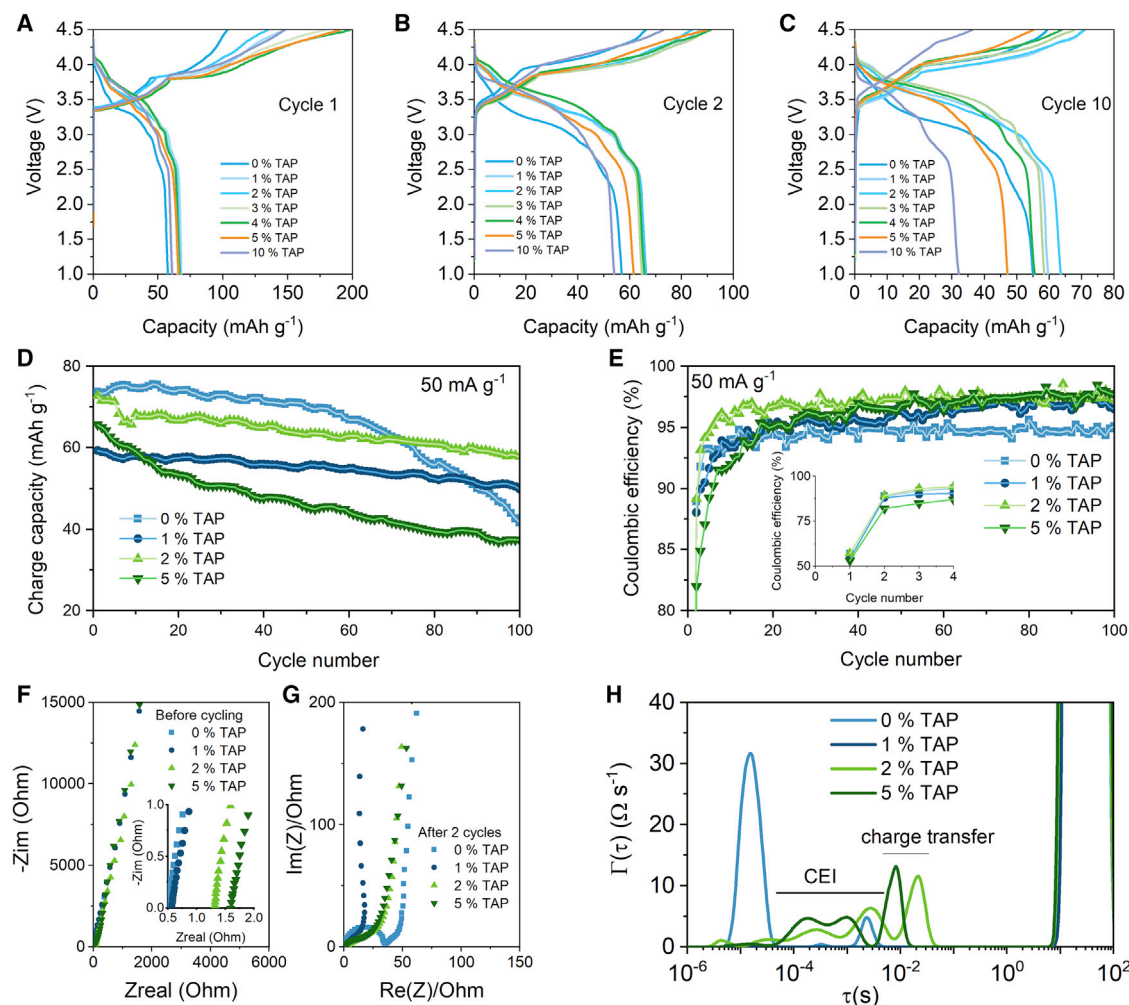


**Figure 5. An MoS<sub>2</sub> electrode with pre-formed SEI layer and the use of triallyl phosphate additive improve both cycle life and coulombic efficiency of an MoS<sub>2</sub>-natural-graphite dual-ion intercalation battery**

(A–H) The galvanostatic curves for the (A) 1<sup>st</sup>, (B) 2<sup>nd</sup>, and (C) 10<sup>th</sup> cycles measured at 50 mA g<sup>-1</sup> show the impact of varying amounts of TAP additives in control electrolyte (6 m KTFPI in DMC) on cycling stability (see also Figure S24 and Table S1), (D) extended cycle life of full-cell KDIB with pre-cycled MoS<sub>2</sub> in concentrated electrolytes with 0%–5% TAP, (E) the coulombic efficiency corresponding to the data in (D), (F) the Nyquist diagrams for EIS data measured for 3-electrode KDIBs before galvanostatic cycling (see also Figures S25 and S26) and (G) after 2 charge-discharge galvanostatic cycles at 50 mA g<sup>-1</sup> in various electrolytes, and (H) DRT plots obtained from the EIS data in (G) (see also Figure S27).

electrode stabilized with pre-formed SEI layer. Further improvements to the cycle life and CE could be achieved through electrolyte additives. A 1–5 wt % of TAP additive was included in the 6 m KTFPI-DMC electrolyte to generate a stable CEI on the graphite electrode. As can be seen in Figure 5E, the additives had marginal effect on the iCE, which ranged from 53% to 57%, while the specific discharge capacities shown in Figure 5D were approximately 74 (0% TAP), 59 (1% TAP), 73 (2% TAP), and 66 mAh g<sup>-1</sup> (5% TAP). Over the first 20 cycles, the specific capacity and CE for the control electrolyte appeared to stabilize at ~74 mAh g<sup>-1</sup> and 95%. In the presence of the TAP additive, the corresponding specific capacity and CE were ~58 mAh g<sup>-1</sup> and ~96% for 1% TAP, ~67 mAh g<sup>-1</sup> and ~97% for 2% TAP, and ~53 mAh g<sup>-1</sup> and 95% for 5% TAP (see Table S1 comparing performance metrics of various KDIBs reported in the literature). It is worth noting that the 1% and 2% TAP additives provided higher capacity retention after 100 cycles, namely 85% and 79%, respectively, whereas the 0%- and 5%-TAP-containing

electrolytes showed 56%–57% retention. In terms of CE, however, the presence of the additive delivered better efficiency (~97%–98%), as compared to the control electrolyte (~95%). The results indicated that 1%–2% TAP additive could be sufficient to achieve desirable performance over extended cycles.

It is worth mentioning that previous studies on high-voltage batteries demonstrated that increasing amounts of TAP additive resulted in higher cell resistance associated to the buildup of thicker SEI or CEI layer on the active materials.<sup>26</sup> The Nyquist plots given in Figures 5F and 5G were measured on the graphite electrodes in 3-electrode cells after relaxation at open circuit voltage (OCV) for 12 h and after 2 galvanostatic charge-discharge cycles. The distribution function of relaxation times (DRT) plots extracted from the EIS data help resolve the different interfacial and bulk processes based on their timescale (see Note S1), as shown in Figures 5H and S25. The peak around 0.1  $\mu$ s in the plot for the electrolyte with no TAP additive could be attributed to the contact resistance due to the mechanical degradation of the electrode coating caused by huge volume variations as a result of anion intercalation and de-intercalation processes. The smaller peak in between 1 ms and 10 ms could be associated to charge transfer reactions due to potential entrapment of anions in the graphite structure. In the presence of TAP additives, the EIS data showed that the graphite electrodes behaved mostly as blocking, with some smaller peaks observed in the DRT plots corresponding to ion conduction across the CEI layer, charge transfer reactions, solid-state ion diffusion, and differential capacitance. Similar measurements were done on full cells before and after 100 cycles (see Figures S26 and S27). As expected, the electrodes exhibited largely capacitive behavior in all electrolyte systems prior to cycling. After 100 cycles, the Nyquist plots showed more features (several peaks in the DRT plots) with semi-circles indicative of interfacial processes and charge transfer reactions. Because the EIS data are the sum of the impedance contributions from the positive and negative electrodes, making accurate measurements might be difficult; however, the polarization signified by the peaks in the range 10–100  $\mu$ s increased with increasing amount of TAP additives, which could be related to the formation of the poly(TAP)-containing CEI layer. The features from 1 ms to 100 ms could be ascribed to the charge transfer processes at the positive and negative electrodes, and diffusion of ions in the bulk of the electrode materials exhibited polarization peaks at time constants >100 ms.

Increasing the current to 100 mA g<sup>-1</sup> (Figure 6A) evidently resulted in lower specific capacities (63 mAh g<sup>-1</sup> for 1% TAP, 51 mAh g<sup>-1</sup> for 2% TAP, and 50 mAh g<sup>-1</sup> for 5% TAP, while the iCE values remained nearly the same, ranging from 54% to 58%. Notably, the CE (Figure 6B) improved significantly over 100 cycles, reaching 98%–99%, though the capacity retentions were 96% for 1% to 2% TAP and 56% for the electrolyte containing 5% TAP additive. More investigation may be needed to further optimize the amount of TAP and the concentration of KTFSl, in the presence of efficient Al-passivating salt additive, to fully tackle capacity fading and to improve CE. In this work, the electrolyte with 2% TAP additive was selected for rate capability tests performed at 25, 50, 100, 250, and 500 mA g<sup>-1</sup>. As shown in Figures 6C and S28, in the first instance, the average reversible capacity appeared to decrease progressively (as the current increased from 25 to 500 mA g<sup>-1</sup>) as ~70, ~61, ~58, ~50, and ~44 mAh g<sup>-1</sup>, while the associated CE values, in general, increased to ~78%, ~90%, ~94%, and ~99%. In addition, from the galvanostatic curves in Figure S28, one can conclude that there were some trapped anions that could be extracted when the cell was held at 1 V (until the current decayed to <1  $\mu$ A). It was likely that trapping of anions could be decreased if smaller graphite particles were used, though the increase in surface area might aggravate undesirable reactions.

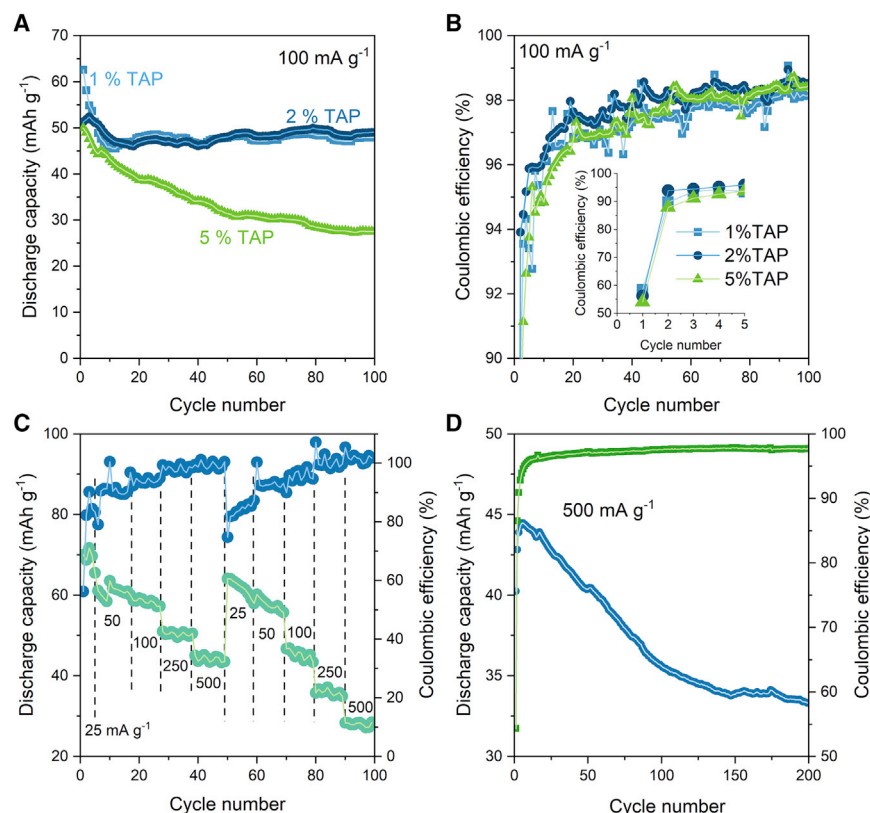


**Figure 6. The rate capability and long-term cycling of an MoS<sub>2</sub>-natural-graphite dual-ion intercalation battery**

(A–D) (A) The capacity-cycle number at 100 mA g<sup>−1</sup> in electrolytes containing additives, (B) evolution of the CE values as a function of cycle number associated to data in (A), (C) rate performance measured at 25–500 mA g<sup>−1</sup> for the full-cell KDIB based on 6 m KTFSI in DMC electrolyte with 2% TAP (see also Figure S28), and (D) extended cycling data and CE values for galvanostatic cycling at 500 mA g<sup>−1</sup>.

Repetition of the rate test showed that the cell suffered from lower capacity retention (~64%–86%) as the current increased beyond >100 mA g<sup>−1</sup>, even if the CE values improved continuously from ~83% at 25 mA g<sup>−1</sup> and ~95%–100% in the range 100–500 mA g<sup>−1</sup>. At 25 and 50 mA g<sup>−1</sup>, approximately 89% and 95% of the initial discharge capacities were retained. Furthermore, over long-term cycling at 500 mA g<sup>−1</sup> (Figure 6D), the cell sustained a decrease in the specific capacity from 44 to 36 and 33 mAh g<sup>−1</sup> at the 100<sup>th</sup> and 200<sup>th</sup> cycles, respectively, which amounted to 80% and 75% retention, although the coulombic efficiency stabilized at ~98% from the 100<sup>th</sup> cycle onward.

#### A TAP additive forms a polymeric CEI on graphite particles

After 100 cycles at 50 mA g<sup>−1</sup>, the graphite electrodes were taken out of the cells and cleaned in DMC and characterized to probe potential changes in particle morphology, surface composition, and bulk structure. The anticipated role of TAP monomer was to polymerize on the surface of graphite particles to form a thin layer of CEI that can prevent solvent co-intercalation during the anion intercalation process as illustrated in Figure 7A. The SEM images (Figures 7B–7E) display that electrodes cycled in the absence of the TAP additive exhibited considerable expansion (and exfoliation) with no surface coverage. Mainly carbon was detected in the EDX spectra and elemental maps provided in Figures S29 and S30. In contrast, those treated in the additive-containing

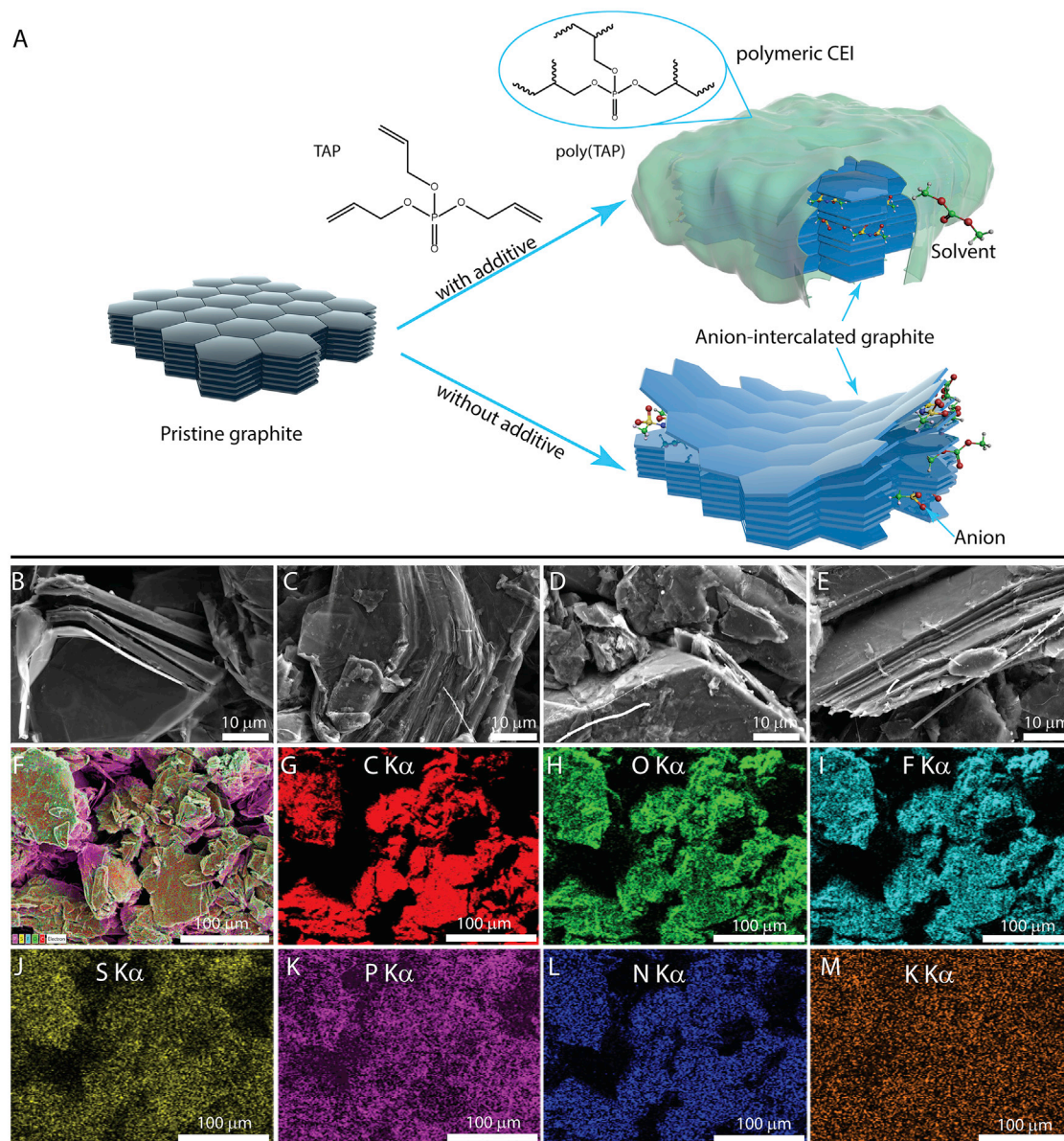


**Figure 7. A triallyl phosphate additive forms a polymeric CEI on graphite particles as verified using SEM-EDX analysis**

(A–M) A schematic illustration of how the CEI layer suppresses graphite exfoliation, (B) graphite particle after 100 cycles in 6 m KTFSI-DMC with no additive, (C) graphite particle after 100 cycles in 6 m KTFSI-DMC with 1 wt % TAP, (D) graphite particle after 100 cycles in 6 m KTFSI-DMC with 2 wt % TAP, (E) graphite particle after 100 cycles in 6 m KTFSI-DMC with 5 wt % TAP, and (F) an overlay of EDX maps for graphite electrodes cycled in the presence of 2 wt % TAP (see also [Figure S29](#)); the individual elemental maps are shown in (G) carbon K $\alpha$ , (H) oxygen K $\alpha$ , (I) fluorine K $\alpha$ , (J) sulfur K $\alpha$ , (K) phosphorus K $\alpha$ , (L) nitrogen K $\alpha$ , and (M) potassium K $\alpha$  (see also [Figures S30–S32](#)).

electrolytes appeared to be coated in some form of polymeric layer and no exposed graphite surface or edges were visible. Elemental EDX mapping was helpful in identifying the composition of the CEI film as shown in [Figures 7F–7M](#) and [S29](#) for a 2% TAP additive and [Figures S30–S32](#) for those electrodes cycled in electrolytes consisting of 1% and 5% TAP. Accordingly, the surface layer contained a nearly uniform distribution of the elements expected from the electrolyte and the graphite electrodes, except P, which appeared to accumulate around the edges of the graphite particles ([Figure 7F](#)), where increased reactivity is expected as opposed to the basal planes of the graphene

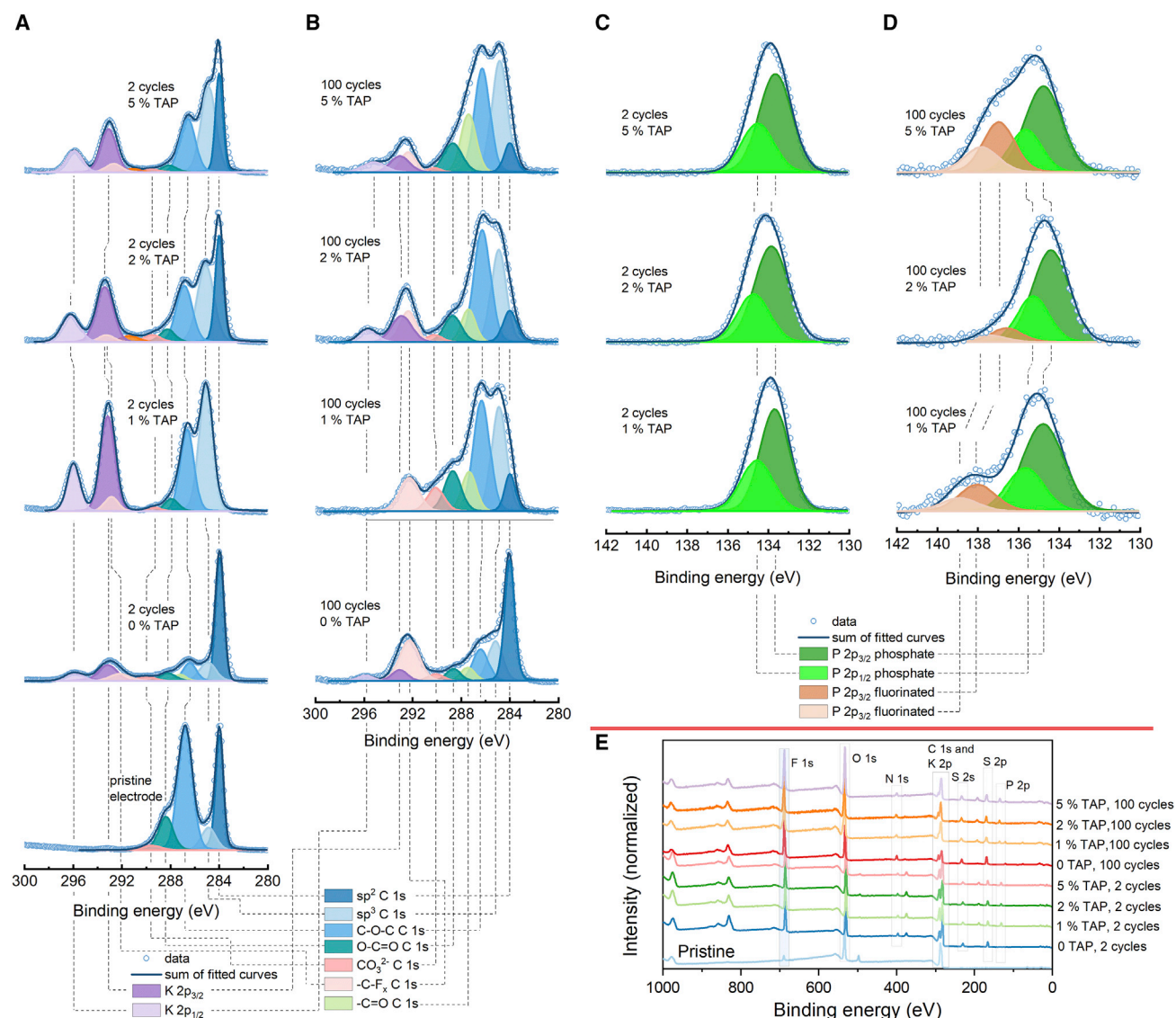


**Figure 8. A triallyl phosphate additive forms a polymeric CEI on graphite particles based on XPS analysis**

(A–E) (A) The C1s spectra of pristine electrode, and those cycled in electrolytes with and without TAP additives after the 2<sup>nd</sup> cycle; (B) the C1s spectra of graphite electrodes cycled in electrolytes with and without TAP additives after 100 cycles; (C) the P2p spectra of electrodes cycled for 2 cycles; (D) the P2p spectra after 100 cycles; and (E) wide-scan survey spectra for pristine and cycled graphite electrodes (see also Figures S34–S36).

layers. The overall EDX spectra shown in Figure S29 also showed that the intensity of P increased with increasing TAP additive. The formation of polymeric layer in the electrodes is also anticipated to help keep the particles bound to each other and the Al current collector; this is particularly important as the sodium carboxymethylcellulose (CMC) binder can potentially degrade over time, causing detachment of graphite particles, which could be a source of additional capacity fading. Raman spectra (Figure S33) of the electrodes measured *ex situ* indicated that the bulk structure of the graphite particles cycled in the absence of TAP additive sustained more marked degradation than graphite particles coated in the polymerized TAP as evidenced by broad D bands and the higher intensity of the D' band near the G band. In particular, the electrolyte with 1%–5% TAP helped preserve the graphite structure better, as indicated by diminished D bands and less intense D' (E<sub>2g2</sub>-b modes) bands.

To further confirm the formation of stable CEI layers on the graphite particles, XPS analyses (Figure 8) were performed on the electrodes after the 2<sup>nd</sup> and 100<sup>th</sup> cycles in electrolytes with and without TAP additives. The C 1s spectrum of the pristine electrode showed peaks coming mainly from the sp<sup>2</sup>-hybridized carbon of graphite at a binding energy of 284 eV and the –C–O–C– bonds of CMC binder at 286.8 eV. Other smaller peaks were also observed due to sp<sup>3</sup>-hybridized –C–C– bonds at 284.8 eV, –O–C=O at 288.4 eV, and a very small peak centered on 289.6 eV indicative of trace amounts of metal carbonate. As shown in Figure 8 (the O 1s, F 1s, N 1s, and S 2p spectra can be found in Figure S34), without TAP additive, the characteristic peaks of the sp<sup>2</sup>-hybridized carbon of graphite were clearly visible in the C 1s spectra, although the intensity of the peaks from the binder diminished considerably over two cycles. There were also additional peaks originating from the salt. The peaks from the salt included the doublet from K<sup>+</sup> (2p<sub>3/2</sub> at 293.2 eV) and C 1s from –CF<sub>x</sub> of TFSI located around 292 to 292.9 eV. Based on the C 1s spectra (see Figures 8A and 8B), it can be concluded that the CMC binder underwent decomposition reaction in which part of the –C–O– bonds were lost. This suggests the absence of stable CEI in the case of 6 m KTFSl-DMC electrolyte and hence the poor CE and faster capacity fading as discussed above. More or less similar spectra were observed for the electrodes after 100 cycles except that the intensities of the sp<sup>3</sup> –C–C–, –C–O–, and –C–F<sub>x</sub> species increased, but no stable CEI formed as evidenced by the sp<sup>2</sup> C peak, which was still the most intense. The allyl groups in TAP readily polymerize electrochemically on the graphite electrodes, resulting in better CEI layer than the control electrolyte. The C 1s spectra of electrodes cycled in 1–5 wt % TAP additives generally exhibited considerably increased amount of sp<sup>3</sup>-hybridized –C–C– bonds at 284.9–285.1 eV and –C–O– bonds at 286.5–286.9 eV arising from the polymerized allyl groups. The emergence of the peaks was evidence for the formation of the polymeric CEI on the surface. With the exception of the electrode cycled in 1 wt % TAP additive, which was covered in more salt, in all cases, the graphitic carbon at 284 eV was clearly visible. After 100 cycles, the deconvoluted peaks in the C 1s spectra exhibited significant increase in the intensities of the peaks from the TAP and the intensity of the graphite peak diminished considerably. In addition, the peaks at 133.6–133.8 eV in the P 2p spectra shown in Figures 8C and 8D indicated the presence of phosphate species of the TAP in the CEI, which confirmed that the TAP additive formed a CEI coating on the graphite particles. The thickness of the CEI was roughly estimated using the XPS data (see Note S2 and Figures S35 and S36). Accordingly, the CEI formed in the presence of the TAP additive tended to grow thicker in the presence of the TAP additive and with increasing cycles. After 100 cycles, additional type of phosphorous was observed at 136.5–138 eV, possibly due to partial fluorination of the poly(TAP) to form –P–O–F bonds. Further study is needed to understand the reaction pathways of the TAP monomer and the aging mechanism of the poly(TAP) layer.

Thus, it can be concluded that this research sheds light on the importance of polymerizing electrolyte additives in modifying the surface of graphite electrodes and thus ensuring more stable electrochemical performance in DIBs. A significant improvement in the CE and cycle life of DIBs can be achieved by mitigating interfacial reactions at the negative and positive electrodes. In the future, we intend to investigate factors that impact the formation, stability, and aging of the polymeric CEI layer on graphite electrodes. Various types of additives similar to TAP (such as polymerizing ionic liquids) will be selected and studied in KDIBs. Furthermore, it is worth investigating other strategies to chemically modify the surface of graphite and TMDC electrodes in order to boost their applicability and performance in DIBs. The concept of polymeric CEI explored in this work could further be applied

in high-voltage lithium-ion batteries in which limited anodic stability of the electrolytes causes short cycle life and poor CE.

## EXPERIMENTAL PROCEDURES

### Resource availability

#### Lead contact

Further information and requests for resources and reagents should be directed to Habtom Desta Asfaw ([habtom.desta.asfaw@kemi.uu.se](mailto:habtom.desta.asfaw@kemi.uu.se)).

#### Materials availability

This study did not generate new unique materials.

#### Data and code availability

All of the data associated with the study are included in the paper and the [supplemental information](#) or are available from the lead contact upon reasonable request.

### Materials

The electrolyte KTFSI salt used in the electrolytes was purchased from Solvionic France, and the anhydrous solvents DME, DMC, and EC were supplied by Sigma-Aldrich and Gotion. The mixture of solvents was dried over activated molecular sieves to remove trace amounts of water prior to use for electrolyte preparation. The triallyl phosphate (with >96% purity) was obtained from TCI Chemicals and used as received.

### Electrode fabrication

To prepare the electrodes, 90% by weight of MoS<sub>2</sub> (Riedel-deHaën; 99.5%) or 95% natural graphite (Ted Pella; 100 mesh; trace metal impurities <2 ppm), 5% SuperP carbon (Alfa Aesar) for MoS<sub>2</sub>, and 5% of sodium carboxymethylcellulose (CMC) binder (Leclanché) were mixed in deionized water and absolute ethanol in a 9:1 volume ratio. The mixture was homogenized to form a slurry using Vortex mixer (Vortex Genie2 from Scientific Industries) and then cast onto carbon-coated aluminum foil using a doctor blade to set the coating thickness to 50–100 μm for MoS<sub>2</sub> half-cell test and 150–200 μm for full-cell KDIB tests. The coating was dried at ambient conditions, and 13–20 mm disk electrodes were punched out using a perforator. The electrodes were further dried at 120°C for 12 h in a vacuum oven (Büchi Glass Oven B-585) and stored in a glovebox (GS Glovebox Systemtechnik) with both O<sub>2</sub> and H<sub>2</sub>O levels maintained at <1 ppm. Potassium disk electrodes (~13 mm in diameter) were prepared by pressing cleaned K pieces (Alfa Aesar) on Al foils. The areal mass loadings varied from 3.3 to 4.4 mg cm<sup>-2</sup> for graphite and 4.7 to 7.2 mg cm<sup>-2</sup> for MoS<sub>2</sub> electrodes to maintain a mass ratio in the range 0.6–0.7.

### Electrochemical testing

Prototype electrochemical cells were assembled in pouch-cell formats using the MoS<sub>2</sub> and graphite electrodes and potassium metal disks. Both 2- and 3-electrode half-cell designs were tested. In all the cells, Celgard 2325 separators (25 μm in thickness, 9 cm<sup>2</sup> area, and 39% porosity) with 50–100 μL of 1 M KTFSI in 1:1:1 DMC:DME:EC electrolyte were used. In the case of DIBs, a 6 m KTFSI in DMC was used as the control electrolyte along with glass fiber separators (Whatman; 250 μm in thickness). In addition, 6 m KTFSI with 1, 2, 3, 4, 5, and 10 wt % of TAP (TCI Chemicals) with respect to the mass of the solvent were prepared to achieve passivation of the positive electrode. To attain stable SEI in the DIBs, MoS<sub>2</sub> electrodes were cycled five to ten times in 1 M KTFSI electrolyte prior to use in the KDIBs. The cells were allowed to relax at OCV for 12 h before starting the electrochemical

testing. CV and galvanostatic tests were conducted using Bio-Logic MPG2, Arbin BTS, and Neware cyclers. Correction for uncompensated resistance was incorporated in the CV measurements based on current interruption method with 85% correction. In addition, EIS was conducted (voltage amplitude 3 mV with 1 MHz–10 mHz frequency range) at OCV on 2- and 3-electrode cells after 2 and 100 cycles using Bio-Logic SP240 and MPG2-128 potentiostats. The EIS data were further analyzed to extract DRTs based on the DRTtools as explained in [Note S1](#).<sup>43,44</sup> To evaluate electrolyte conductivities, EIS measurements were conducted using a sinusoidal excitation signal with a voltage amplitude of 10 mV in a frequency range of 1 MHz–10 mHz. The conductivities were calculated using the resistance obtained at ~19 kHz as shown in the Bode admittance plots in [Figure S2](#). A Bio-Logic HTTC conductivity cell with two planar platinized Pt electrodes and a cell constant of 1 cm<sup>-1</sup> was used for all measurements.

### Electron microscopy

The changes in microstructures and morphologies of the electrodes before and after electrochemical cycling were studied using Zeiss Merlin SEM. The electrodes were mounted on an aluminum stub using carbon tapes (Agar Scientific). All imaging was carried out at a working distance of 7 mm using a 5-keV electron beam and a probe current of 100 pA and by collecting secondary electrons with the InLens and the HE-SE2 detectors. The cycled electrodes were transported in an air-tight, remotely controlled sample transfer shuttle (Semilab Germany) out of the glovebox to the electron microscope without exposure to air. EDX analyses were performed on cycled graphite electrodes using X-MAX EDS System (Oxford Instruments) detector with Aztec software at an acceleration voltage of 5 keV, a probe current of 100 pA, and a working distance of 8.5 mm.

### Raman spectroscopy

Raman spectra of the pristine natural graphite and MoS<sub>2</sub> powder and the cycled electrodes were collected on a Renishaw InVia Ramanscope using 50-mW, 532-nm and 785-nm lasers operated at 0.5%–1% power. A pouch cell was built with a glass window for *in situ* characterization of the MoS<sub>2</sub> electrodes cycled to different state-of-charge. Before each measurement, the cell was allowed to rest until stable OCV was attained. The electrodes were cycled at 10 mA g<sup>-1</sup> to pre-determined cutoff voltages during discharge and charge: discharge to 1.2, 1.1, 1.0, 0.8, and 0.5 V and charge to 0.8, 1.0, 1.2, 1.6, and 2.0 V versus K<sup>+</sup>/K. Raman spectra were collected using a 50-mW, 532- and 785-nm laser at a 0.5%–1% power. In each experiment, 8–16 samples spots were probed to ensure signals recorded were representative of the samples. *Ex situ* Raman spectra measurements were conducted on cycled graphite and MoS<sub>2</sub> electrodes to gain insight into structural changes involved during extended cycling. In addition, graphite electrodes were retrieved from full-cell KDIBs after charge and discharge to different states (charge: 3, 3.4, 3.8, 4.2, 4.5, and 4.7 V; discharge: 3.7, 3.2, 1, and 0 V) for analysis with Raman spectroscopy. The Raman spectra were measured *ex situ* using a 50-mW, 532- and 785-nm laser at a 0.05%–1% power. In addition, the electrolytes (0.5–6 m KTFPI in DMC) were investigated using a 785-nm laser to understand solvent-ion interactions at different salt concentrations. All electrodes were transferred from an Ar-filled glovebox to the spectrometer in an air-tight cell, and measurements were made through a thin quartz glass window.

### XPS

The XPS measurements were performed on PHI 5500 and Kratos Axis Supra+ spectrometers equipped with a monochromatic Al K $\alpha$  radiation (1,487 eV). Pieces of the cycled electrodes were placed on a copper tape to fix them on the sample holders.

The electrodes from cells interrupted at various states of charge were studied. Pieces of the electrodes were soaked in DME or DMC for 1 to 2 min and rinsed with the same solvent to remove excess electrolyte salt and solvent and were transferred to the spectrometer after drying in an airtight sample transfer shuttle. The peaks in the XPS spectra were shifted with reference to the 285 eV C 1s peak or the K 2p peak at 293 eV. To estimate the CEI thickness on cycled electrodes, sputtering was performed using a monoatomic Ar<sup>+</sup> source operated at 5 keV and etch time of 100 s as described in [Note S2](#). Non-linear least-squares peak fitting was performed using pseudo-Voigt functions in Igor Pro software.

## XRD

Pristine graphite and MoS<sub>2</sub> powder samples were dispersed on Si sample holders and analyzed using Bruker D8 Advance diffractometer. Air-sensitive samples (graphite and MoS<sub>2</sub> electrodes at fully charged and discharged states) were covered with Kapton tape and analyzed in a transmission mode using STOE diffractometer equipped with a Cu X-ray source ( $\lambda = 1.5406 \text{ \AA}$ ) and three Dectris Mythen 3K DSC4 detectors. The reflections corresponding to the Al current collector were used as an internal calibration standard, and measurements took place in a range between 10° and 120°, with a step size of 0.015°.

## SUPPLEMENTAL INFORMATION

Supplemental information can be found online at <https://doi.org/10.1016/j.xcrp.2021.100693>.

## ACKNOWLEDGMENTS

This research was funded by the ÅForsk Foundation under award number 19-650. The electron microscopy studies were conducted at the Ångström Microstructure Laboratory of the Myfab-MSL network housed within Uppsala University. The authors thank Dr. Girma H. Gebresenbut (Uppsala University) for assistance with XRD measurements.

## AUTHOR CONTRIBUTIONS

H.D.A. conceived the project, carried out the experiments, and wrote the paper. A.K. conducted the acquisition and processing of the XPS and *ex situ* XRD data.

## DECLARATION OF INTERESTS

The authors declare no competing interests.

Received: July 23, 2021

Revised: November 1, 2021

Accepted: November 22, 2021

Published: December 17, 2021

## REFERENCES

1. Kravchik, K.V., Bhauriyal, P., Piveteau, L., Guntlin, C.P., Pathak, B., and Kovalenko, M.V. (2018). High-energy-density dual-ion battery for stationary storage of electricity using concentrated potassium fluorosulfonylimide. *Nat. Commun.* 9, 4469.
2. Fan, L., Liu, Q., Chen, S., Lin, K., Xu, Z., and Lu, B. (2017). Potassium-based dual ion battery with dual-graphite electrode. *Small* 13, 1701011.
3. Ji, B., Zhang, F., Song, X., and Tang, Y. (2017). A novel potassium-ion-based dual-ion battery. *Adv. Mater.* 29, 1700519.
4. Hosaka, T., Kubota, K., Hameed, A.S., and Komaba, S. (2020). Research development on K-ion batteries. *Chem. Rev.* 120, 6358–6466.
5. Komaba, S., Hasegawa, T., Dahbi, M., and Kubota, K. (2015). Potassium intercalation into graphite to realize high-voltage/high-power potassium-ion batteries and potassium-ion capacitors. *Electrochem. Commun.* 60, 172–175.
6. Ji, B., Zhang, F., Wu, N., and Tang, Y. (2017). A dual-carbon battery based on potassium-ion electrolyte. *Adv. Energy Mater.* 7, 1700920.
7. Tan, H., Zhai, D., Kang, F., and Zhang, B. (2021). Synergistic PF<sub>6</sub><sup>−</sup> and FSI<sup>−</sup> intercalation enables

- stable graphite cathode for potassium-based dual ion battery. *Carbon* 178, 363–370.
8. Li, X., Ou, X., and Tang, Y. (2020). 6.0 V high-voltage and concentrated electrolyte toward high energy density K-based dual-graphite battery. *Adv. Energy Mater.* 10, 2002567.
9. Yang, K., Liu, Q., Zheng, Y., Yin, H., Zhang, S., and Tang, Y. (2021). Locally ordered graphitized carbon cathodes for high-capacity dual-ion batteries. *Angew. Chem. Int. Ed. Engl.* 60, 6326–6332.
10. Zhu, J., Li, Y., Yang, B., Liu, L., Li, J., Yan, X., and He, D. (2018). A dual carbon-based potassium dual ion battery with robust comprehensive performance. *Small* 14, e1801836.
11. Beltrop, K., Beuker, S., Heckmann, A., Winter, M., and Placke, T. (2017). Alternative electrochemical energy storage: potassium-based dual-graphite batteries. *Energy Environ. Sci.* 10, 2090–2094.
12. Kotronia, A., Edström, K., Brandell, D., and Asfaw, H.D. (2021). Ternary ionogel electrolytes enable quasi-solid-state potassium dual-ion intercalation batteries. *Adv. Energy Sustain. Res.* Published online October 8, 2021. <https://doi.org/10.1002/aesr.202100122>.
13. Zhou, J., Liu, Y., Zhang, S., Zhou, T., and Guo, Z. (2020). Metal chalcogenides for potassium storage. *InfoMat* 2, 437–465.
14. Zhang, R., Bao, J., Pan, Y., and Sun, C.-F. (2018). Highly reversible potassium-ion intercalation in tungsten disulfide. *Chem. Sci. (Camb.)* 10, 2604–2612.
15. Ren, X., Zhao, Q., McCulloch, W.D., and Wu, Y. (2017). MoS<sub>2</sub> as a long-life host material for potassium ion intercalation. *Nano Res.* 10, 1313–1321.
16. Wang, L., Zou, J., Chen, S., Zhou, G., Bai, J., Gao, P., Wang, Y., Yu, X., Li, J., Hu, Y.-S., and Li, H. (2018). TiS<sub>2</sub> as a high performance potassium ion battery cathode in ether-based electrolyte. *Energy Storage Mater.* 12, 216–222.
17. Zhu, H., Zhang, F., Li, J., and Tang, Y. (2018). Penne-like MoS<sub>2</sub>/carbon nanocomposite as anode for sodium-ion-based dual-ion battery. *Small* 14, e1703951.
18. Zheng, R., Yu, H., Zhang, X., Ding, Y., Xia, M., Cao, K., Shu, J., Vlad, A., and Su, B.-L. (2021). A TiSe<sub>2</sub>-graphite dual ion battery: fast Na-ion insertion and excellent stability. *Ang. Chem. Int. Ed.* 60, 18430–18437.
19. Bellani, S., Wang, F., Longoni, G., Najafi, L., Oropesa-Nuñez, R., Del Rio Castillo, A.E., Prato, M., Zhuang, X., Pellegrini, V., Feng, X., and Bonaccorso, F. (2018). WS<sub>2</sub>-graphite dual-ion batteries. *Nano Lett.* 18, 7155–7164.
20. Kotronia, A., Asfaw, H.D., Tai, C.-W., Hahlin, M., Brandell, D., and Edström, K. (2021). Nature of the cathode-electrolyte interface in highly concentrated electrolytes used in graphite dual-ion batteries. *ACS Appl. Mater. Interfaces* 13, 3867–3880.
21. Wang, Y., Zhang, Y., Wang, S., Dong, S., Dang, C., Hu, W., and Yu, D.Y.W. (2021). Ultrafast charging and stable cycling dual-ion batteries enabled via an artificial cathode–electrolyte interface. *Adv. Funct. Mater.* 31, 2102360.
22. Wang, Y., Zhang, Y., Duan, Q., Lee, P.-K., Wang, S., and Yu, D.Y.W. (2020). Engineering cathode-electrolyte interface of graphite to enable ultra long-cycle and high-power dual-ion batteries. *J. Power Sources* 471, 228466.
23. Read, J.A., Cresce, A.V., Ervin, M.H., and Xu, K. (2014). Dual-graphite chemistry enabled by a high voltage electrolyte. *Energy Environ. Sci.* 7, 617–620.
24. Rothermel, S., Meister, P., Schmuelling, G., Fromm, O., Meyer, H.-W., Nowak, S., Winter, M., and Placke, T. (2014). Dual-graphite cells based on the reversible intercalation of bis(trifluoromethanesulfonyl)imide anions from an ionic liquid electrolyte. *Energy Environ. Sci.* 7, 3412–3423.
25. Xia, J., Ma, L., Nelson, K.J., Nie, M., Lu, Z., and Dahn, J.R. (2016). A study of Li-ion cells operated to 4.5 V and at 55°C. *J. Electrochem. Soc.* 163, A2399–A2406.
26. Xia, J., Madec, L., Ma, L., Ellis, L.D., Qiu, W., Nelson, K.J., Lu, Z., and Dahn, J.R. (2015). Study of triallyl phosphate as an electrolyte additive for high voltage lithium-ion cells. *J. Power Sources* 295, 203–211.
27. Ge, S., Leng, Y., Liu, T., Longchamps, R.S., Yang, X.-G., Gao, Y., Wang, D., Wang, D., and Wang, C.-Y. (2020). A new approach to both high safety and high performance of lithium-ion batteries. *Sci. Adv.* 6, eaay7633.
28. Bohets, H., and van der Veken, B.J. (1999). On the conformational behavior of dimethyl carbonate. *Phys. Chem. Chem. Phys.* 1, 1817–1826.
29. Harris, D.C., and Bertolucci, M.D. (1989). *Symmetry and Spectroscopy: An Introduction to Vibrational and Electronic Spectroscopy* (Courier).
30. Katon, J.E., and Cohen, M.D. (1975). The vibrational spectra and structure of dimethyl carbonate and its conformational behavior. *Can. J. Chem.* 53, 1378–1386.
31. McOwen, D.W., Seo, D.M., Borodin, O., Vatamanu, J., Boyle, P.D., and Henderson, W.A. (2014). Concentrated electrolytes: decrypting electrolyte properties and reassessing Al corrosion mechanisms. *Energy Environ. Sci.* 7, 416–426.
32. Seo, D.M., Boyle, P.D., Sommer, R.D., Daubert, J.S., Borodin, O., and Henderson, W.A. (2014). Solvate structures and spectroscopic characterization of LiTFSI electrolytes. *J. Phys. Chem. B* 118, 13601–13608.
33. Du, X., Huang, J., Guo, X., Lin, X., Huang, J.-Q., Tan, H., Zhu, Y., and Zhang, B. (2019). Preserved layered structure enables stable cyclic performance of MoS<sub>2</sub> upon potassium insertion. *Chem. Mater.* 31, 8801–8809.
34. Li, H., Zhang, Q., Yap, C.C.R., Tay, B.K., Edwin, T.H.T., Olivier, A., and Baillargeat, D. (2012). From bulk to monolayer MoS<sub>2</sub>: evolution of Raman scattering. *Adv. Funct. Mater.* 22, 1385–1390.
35. Frey, G.L., Tenne, R., Matthews, M.J., Dresselhaus, M.S., and Dresselhaus, G. (1999). Raman and resonance Raman investigation of MoS<sub>2</sub> nanoparticles. *Phys. Rev. B* 60, 2883–2892.
36. Zou, J., Li, F., Bissett, M.A., Kim, F., and Hardwick, L.J. (2020). Intercalation behaviour of Li and Na into 3-layer and multilayer MoS<sub>2</sub> flakes. *Electrochim. Acta* 331, 135284.
37. Zhang, X., Tan, Q.-H., Wu, J.-B., Shi, W., and Tan, P.-H. (2016). Review on the Raman spectroscopy of different types of layered materials. *Nanoscale* 8, 6435–6450.
38. Li, F., Zou, J., Cao, L., Li, Z., Gu, S., Liu, Y., Zhang, J., Liu, H., and Lu, Z. (2019). In situ study of K<sup>+</sup> electrochemical intercalating into MoS<sub>2</sub> flakes. *J. Phys. Chem. C* 123, 5067–5072.
39. Carvalho, B.R., and Pimenta, M.A. (2020). Resonance Raman spectroscopy in semiconducting transition-metal dichalcogenides: basic properties and perspectives. *2D Mater.* 7, 042001.
40. Wang, X., Cormier, C.R., Khosravi, A., Smyth, C.M., Shallenberger, J.R., Addou, R., and Wallace, R.M. (2020). In situ exfoliated 2D molybdenum disulfide analyzed by XPS. *Surf. Sci. Spectra* 27, 014019. <https://doi.org/10.1116/6.0000153>.
41. Enoki, T., Suzuki, M., and Endo, M. (2003). *Graphite Intercalation Compounds and Applications* (Oxford University).
42. Xiang, L., Ou, X., Wang, X., Zhou, Z., Li, X., and Tang, Y. (2020). Highly concentrated electrolyte towards enhanced energy density and cycling life of dual-ion battery. *Angew. Chem. Int. Ed. Engl.* 59, 17924–17930.
43. Wan, T.H., Saccoccio, M., Chen, C., and Ciucci, F. (2015). Influence of the discretization methods on the distribution of relaxation times deconvolution: implementing radial basis functions with DRTtools. *Electrochim. Acta* 184, 483–499.
44. Ciucci, F., and Chen, C. (2015). Analysis of electrochemical impedance spectroscopy data using the distribution of relaxation times: a Bayesian and hierarchical Bayesian approach. *Electrochim. Acta* 167, 439–454.

**Cell Reports Physical Science, Volume 3**

**Supplemental information**

**A polymeric cathode-electrolyte interface  
enhances the performance of MoS<sub>2</sub>-graphite  
potassium dual-ion intercalation battery**

**Habtom Desta Asfaw and Antonia Kotronia**

## Supplemental Information

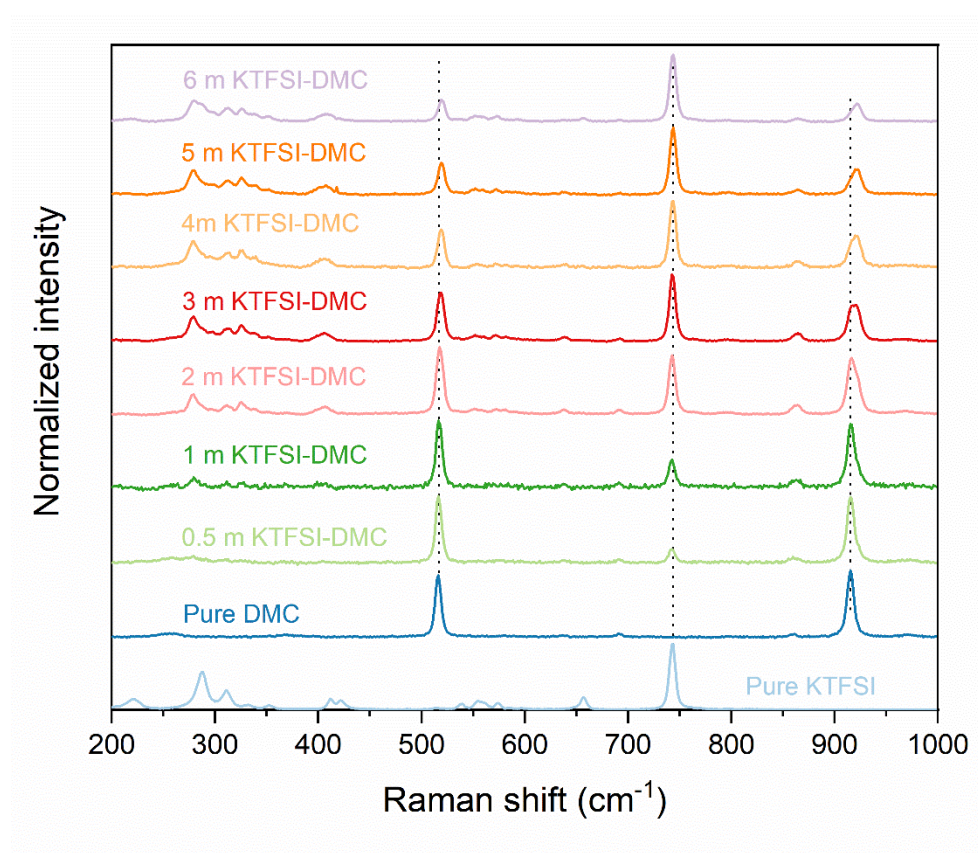


Figure S1: Raman scattering analysis of electrolytes containing varying amounts of KTFSI salt, related to Figure 1: From bottom to top: the Raman spectra of pure KTFSI, pure DMC, and electrolytes containing varied amounts of KTFSI in DMC (molal concentrations)

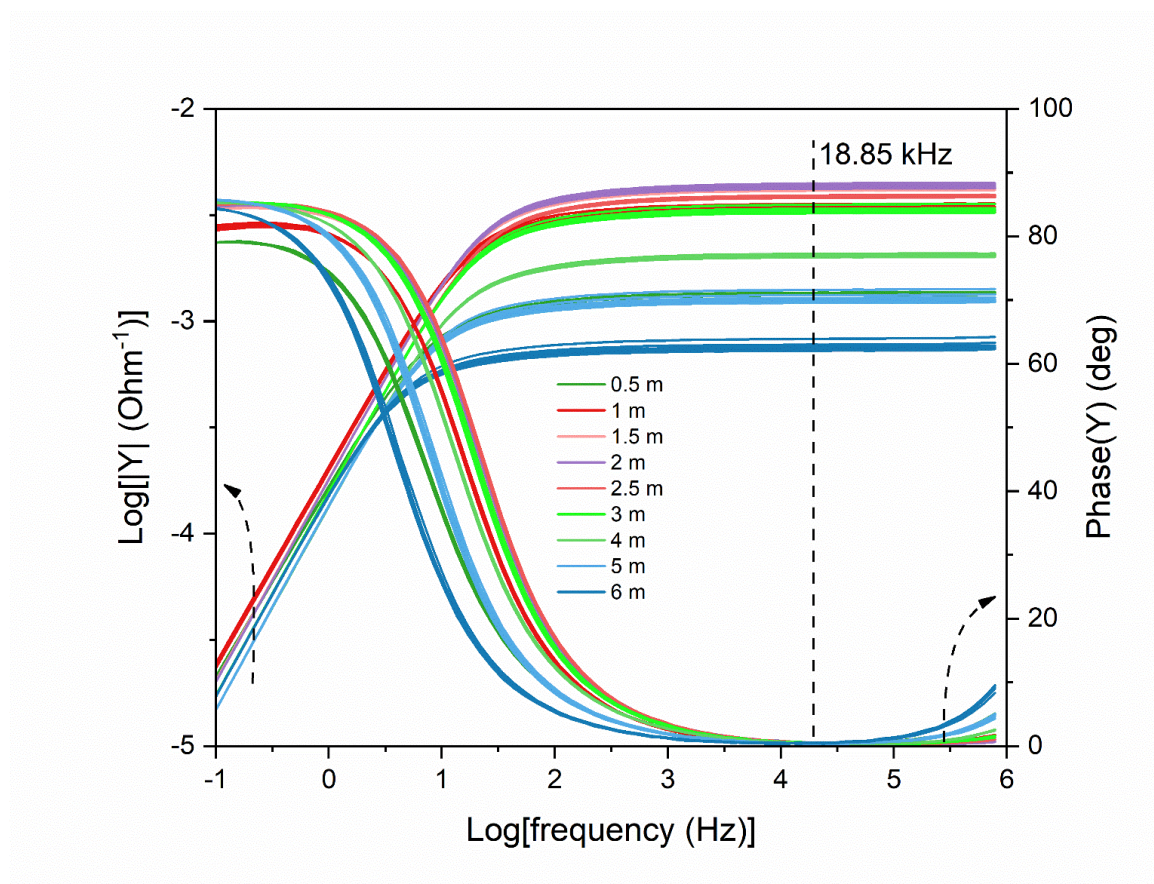


Figure S2: **Evaluation of the ionic conductivity of electrolytes with various salt concentrations, related to Figure 1H:** Bode admittance plots for 0.5 to 6 m KTFSI salt concentration in DMC with a line at ~19 kHz at which the measurement data were used to calculate ionic conductivity

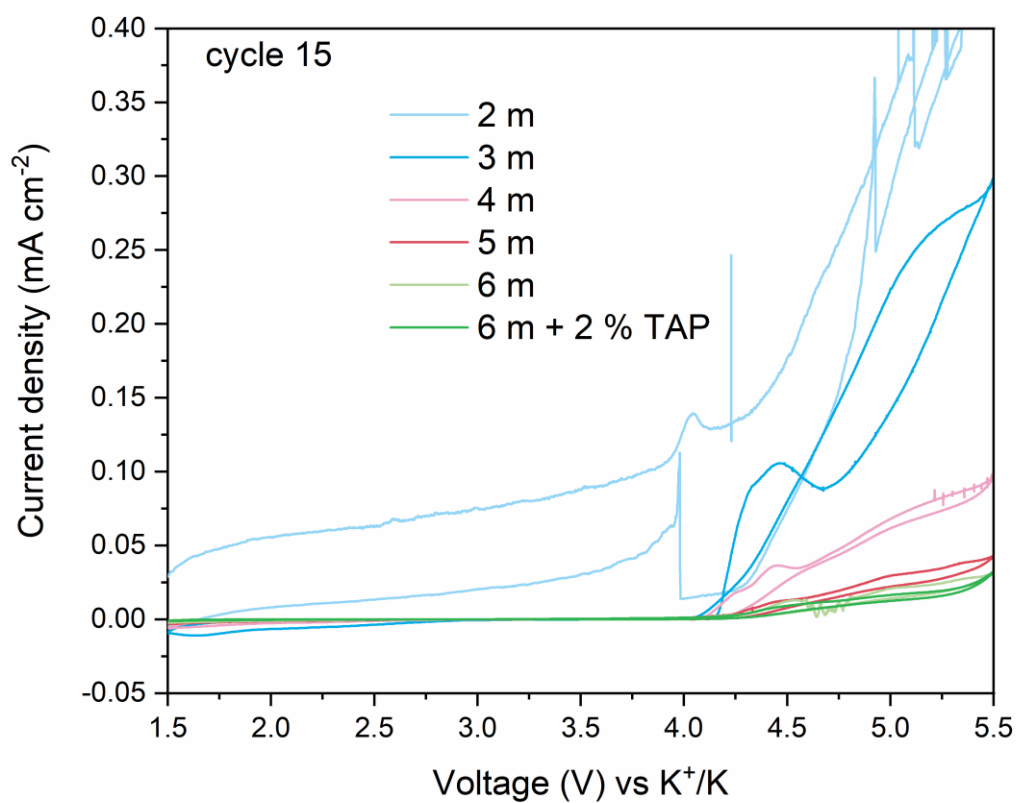


Figure S3: **Anodic stability of aluminium current collectors in DMC-based electrolytes containing different concentrations of KTFSI salt, related to Figure 1:** the cyclic voltammograms at  $1 \text{ mV s}^{-1}$  for the 15<sup>th</sup> cycle show the anodic stability of electrolytes and Al current collectors in the 1.5 to 5.5 V vs.  $\text{K}^+/\text{K}$  range.

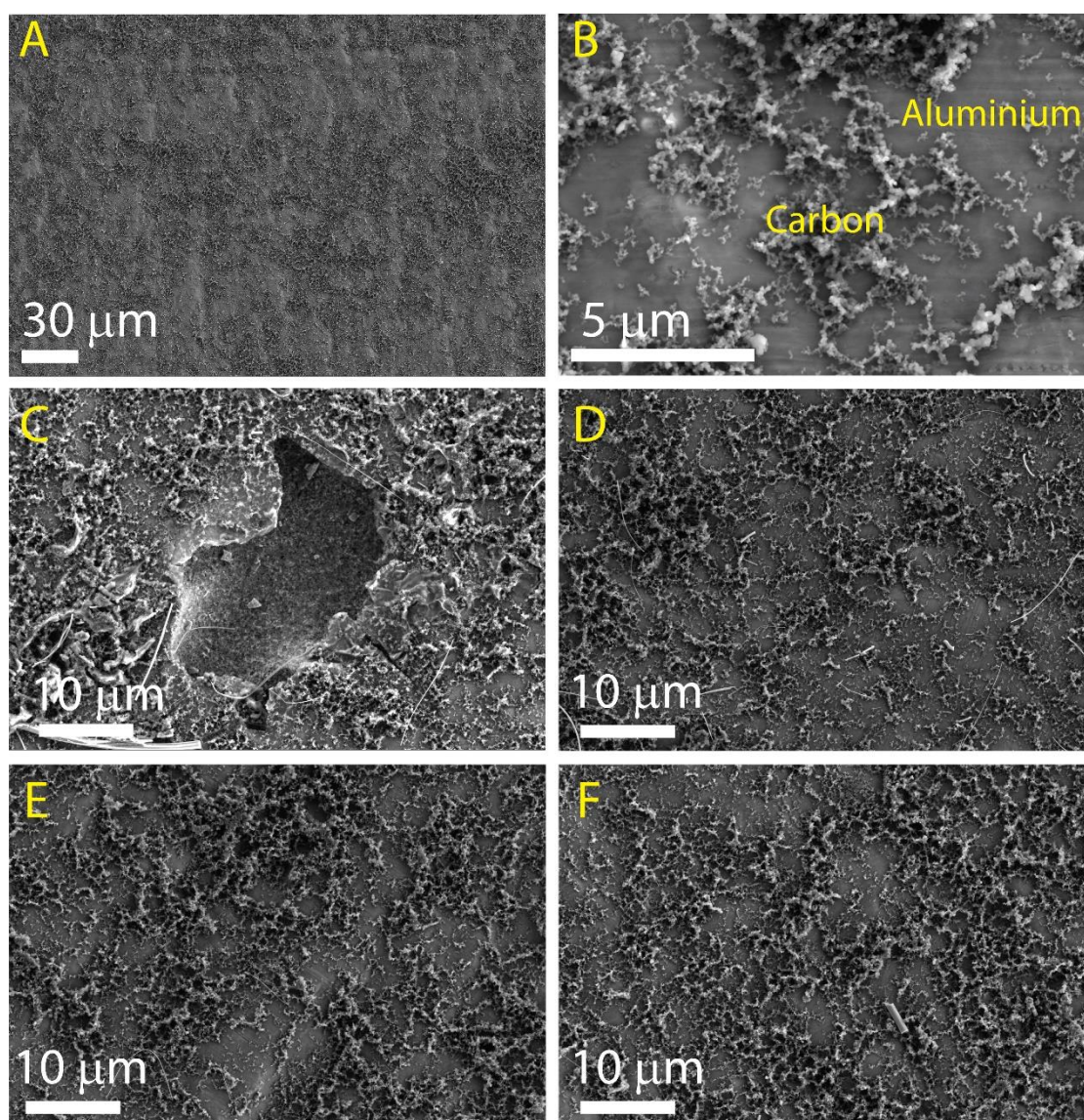


Figure S4: **SEM images showing the impact of electrolyte salt concentration on the anodic stability and structural integrity of carbon-coated Al current collectors, related to Figure 1:** SEM images of (A) pristine carbon-coated Al foil, (B) pristine foil showing the carbon coating on aluminium foil, (C) after 1 cycle in 2 molal KTFSI-DMC, (D) after 1 cycle in 4 molal KTFSI-DMC, (E) after 1 cycle in 5 molal KTFSI-DMC, and (F) after 1 cycle in 6 molal KTFSI-DMC

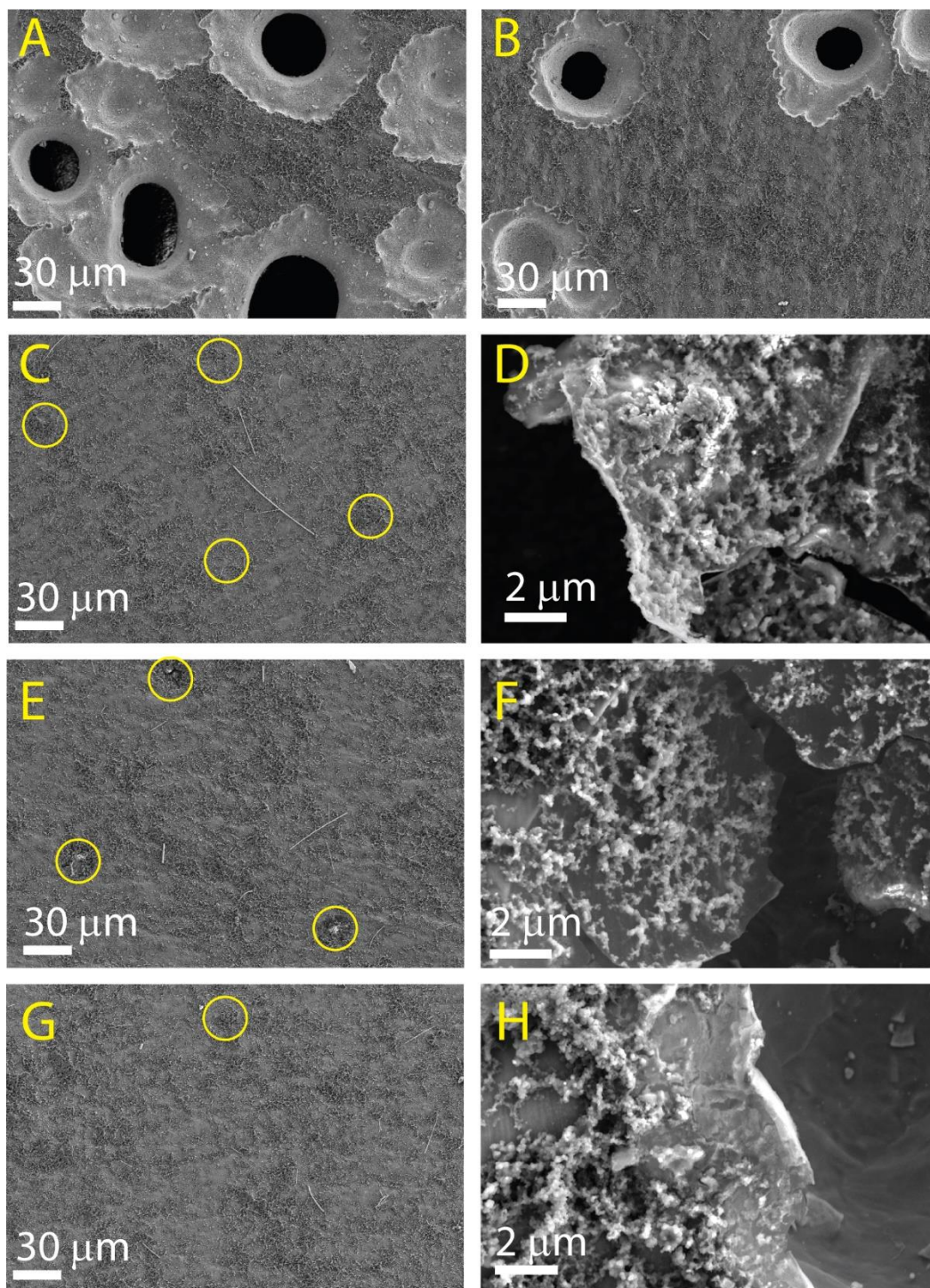


Figure S5: **SEM images showing the impact of electrolyte salt concentration on the anodic stability and structural integrity of carbon-coated Al current collectors, related to Figure 1:** Carbon-coated Al foil after 20 CV cycles in (A) 2 molal KTFSI-DMC, (B) 3 molal KTFSI-DMC, (C) and (D) 4 molal KTFSI-DMC, (E) and (F) 5 molal KTFSI-DMC, and (G) and (H) 6 molal KTFSI-DMC

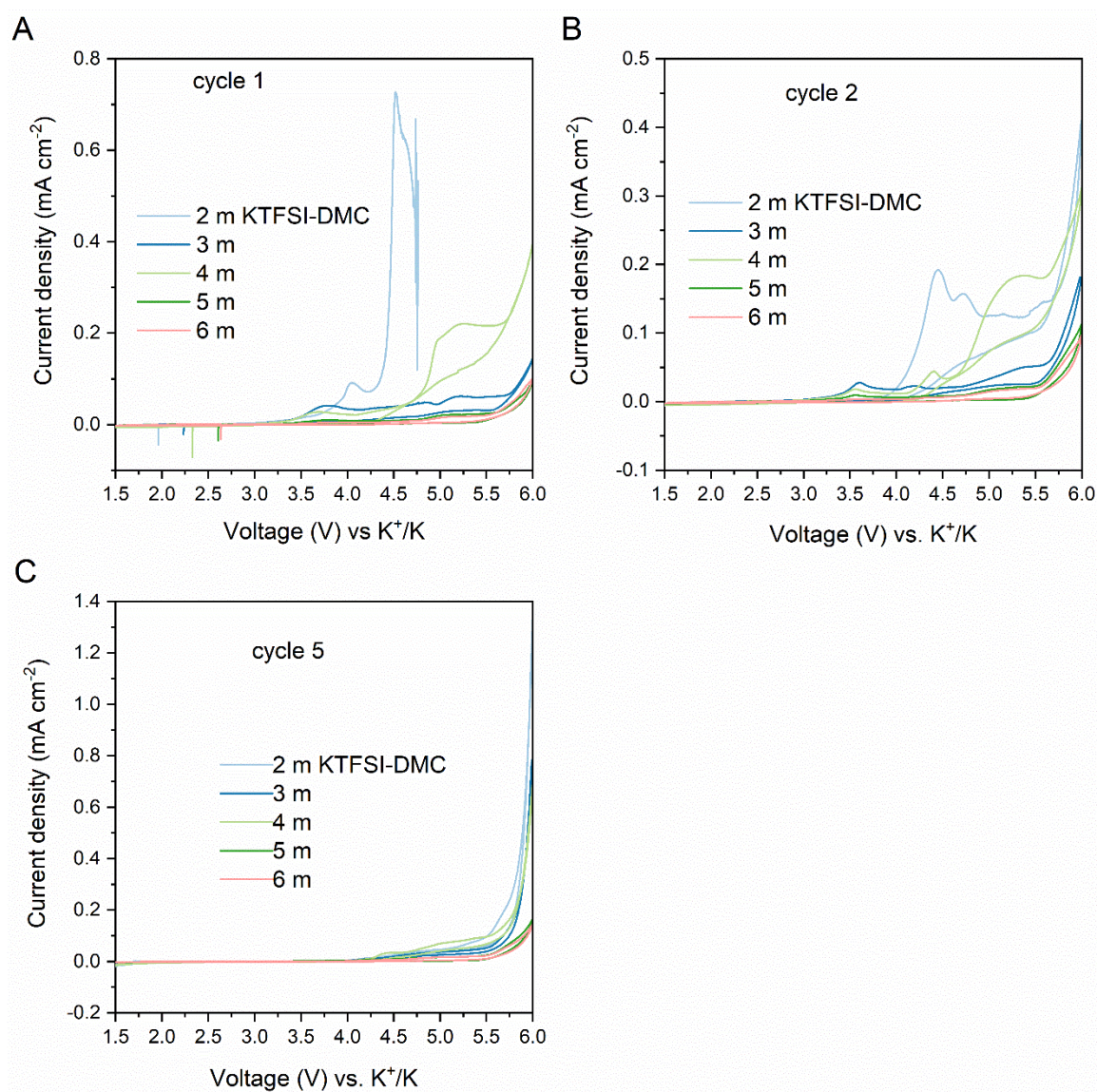


Figure S6: **Anodic stability of DMC-based electrolytes containing different concentrations of KTFSI salt, related to Figure 1:** The 1<sup>st</sup>, 2<sup>nd</sup> and 5<sup>th</sup> CVs at 1 mV s<sup>-1</sup> showing anodic stability of electrolytes on glassy carbon electrodes measured in the range 1.5 to 6 V versus K<sup>+</sup>/K

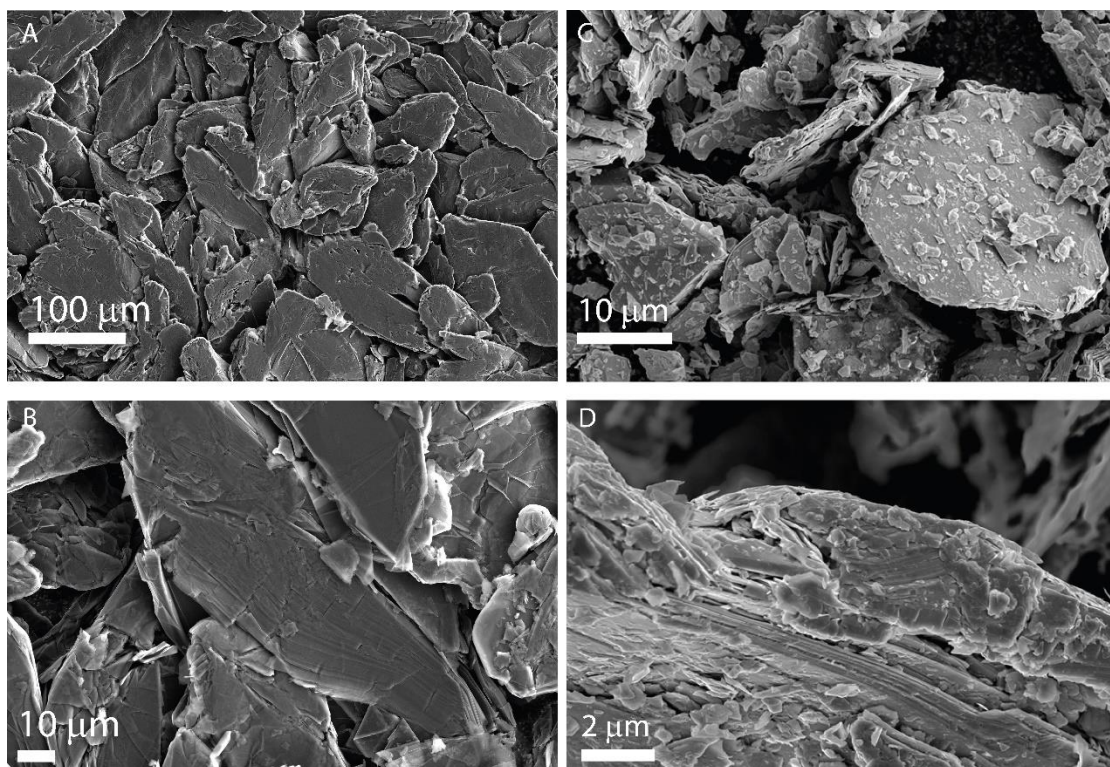


Figure S7: **Morphological characterization of pristine natural graphite and MoS<sub>2</sub> flakes used in the positive and negative electrodes of the KDIB, related to Figure 1, Figure 4, and Figure 7:** The SEM images for pristine powder samples of (A) and (B) natural graphite, and (C) and (D) MoS<sub>2</sub>

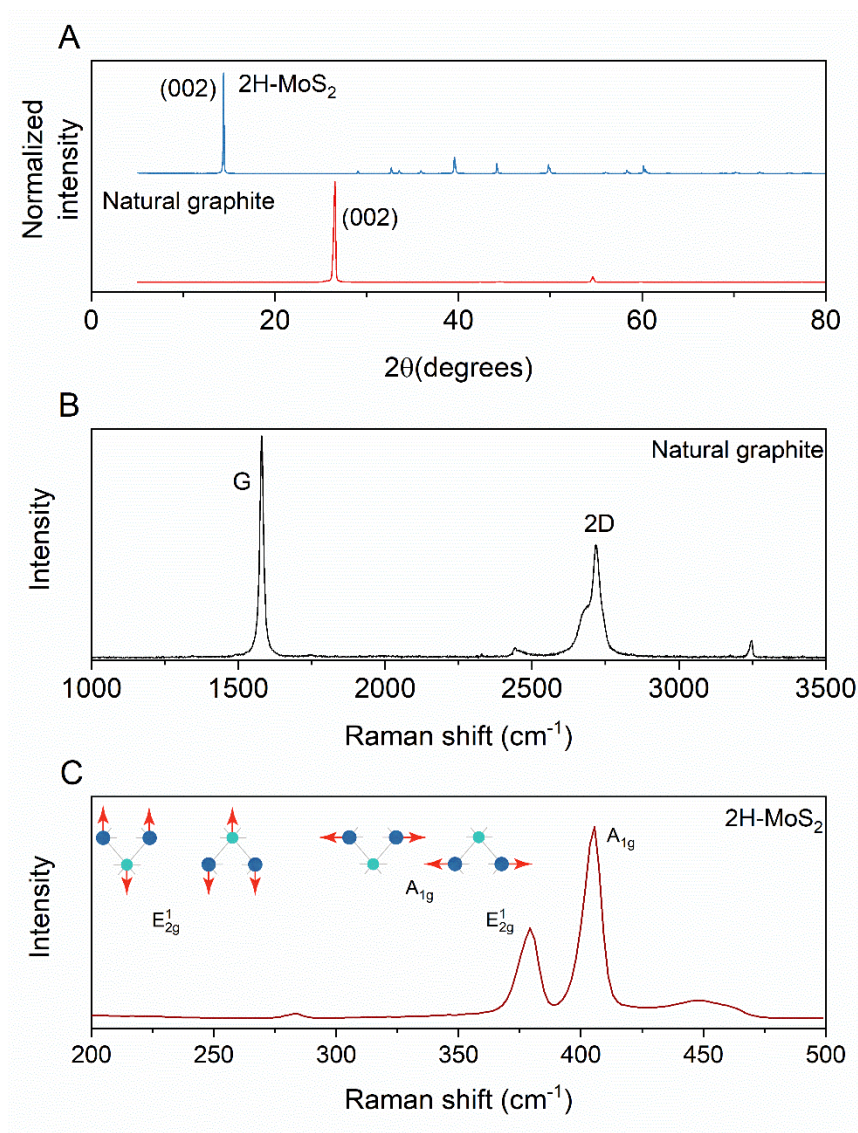


Figure S8: **Structural characterization of pristine MoS<sub>2</sub> and natural graphite powder using X-ray diffraction and Raman spectroscopy, related to Figure 2 and Figure 4:** (A) XRD patterns of 2H-MoS<sub>2</sub> and natural graphite, (B) Raman spectrum of natural graphite, and (C) Raman spectrum of MoS<sub>2</sub>

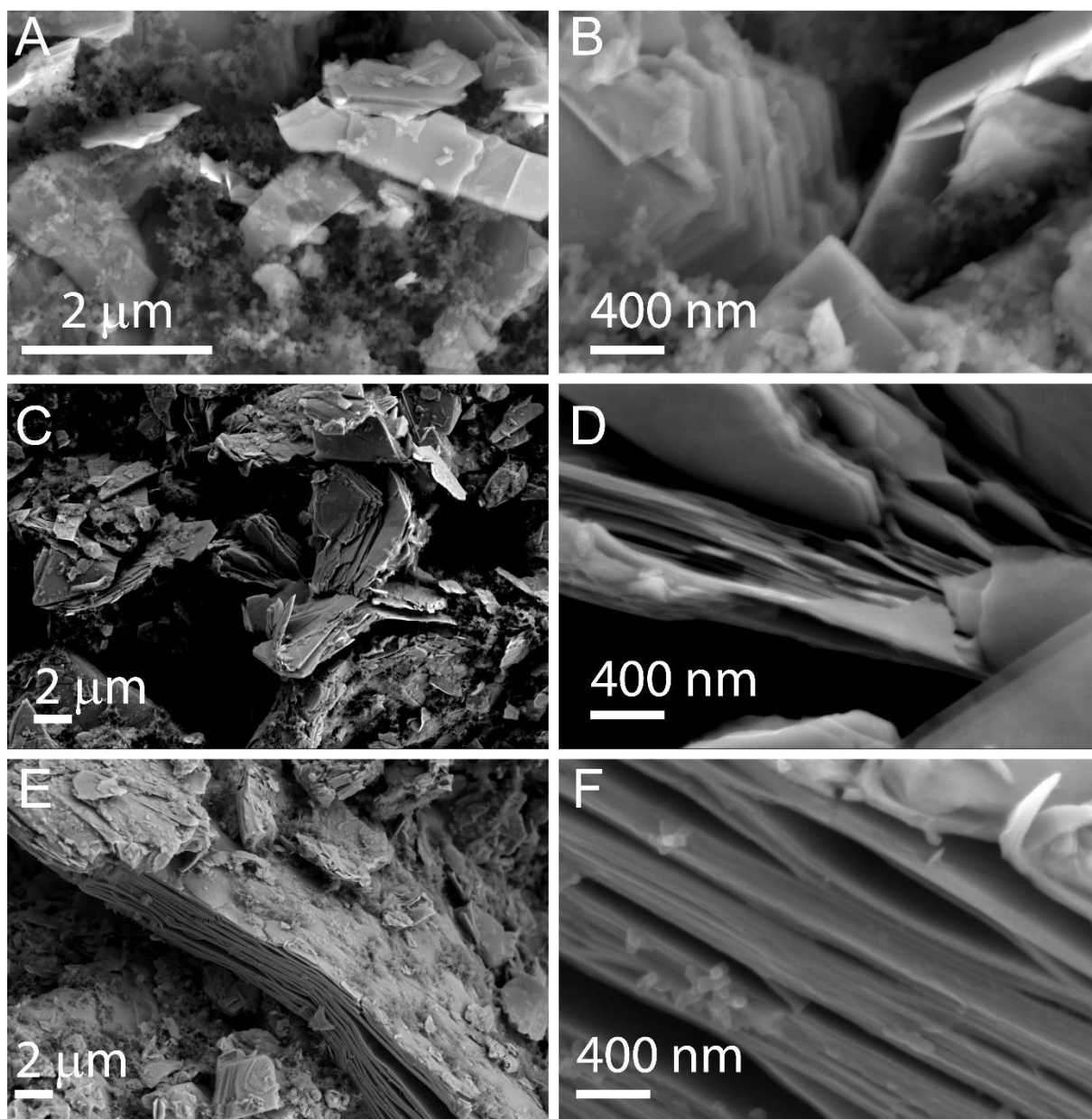


Figure S9: **The influence of  $K^+$  cycling on the morphology of  $MoS_2$  flakes characterized using SEM, related to Figure 2:** The SEM images of (A) and (B) pristine  $MoS_2$  electrodes prior to electrochemical intercalation, (C) and (D) after the 1<sup>st</sup> cycle, and (E) and (F) after the 10<sup>th</sup> cycle in 1 M KTFSI DMC-DME-EC electrolyte

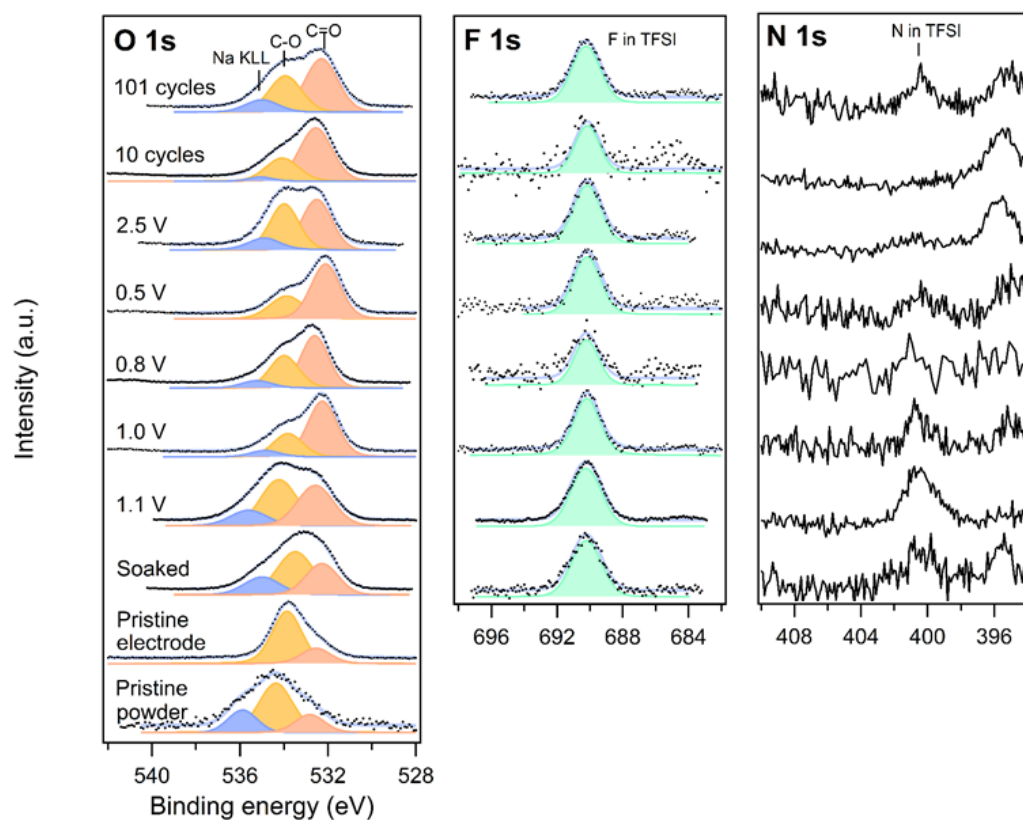


Figure S10: **X-ray photoelectron spectroscopy of MoS<sub>2</sub> electrodes cycled in 1 M KTFSI in DMC-DME-EC electrolyte, related to Figure 2:** The XPS plots for MoS<sub>2</sub> electrodes at various state-of-charge and cycles: O 1s, F 1s and N 1s

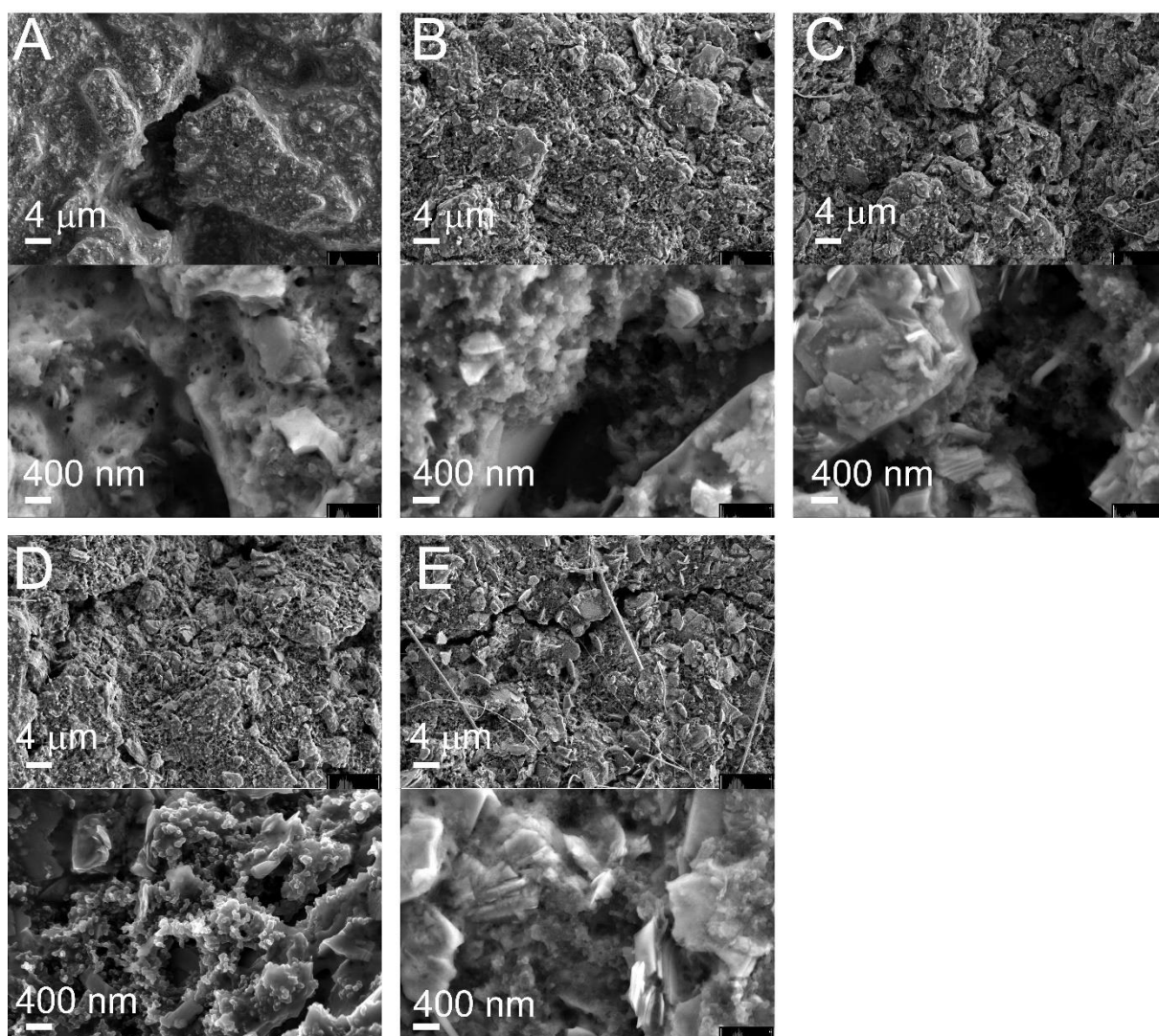


Figure S11: **Morphological changes in MoS<sub>2</sub> electrodes ensuing galvanostatic cycling in concentrated electrolytes, related to Figure 3:** SEM images of MoS<sub>2</sub> electrodes after 20 cycles in 6 m KTFSI-DMC electrolytes containing different amounts of TAP additives (weight percent): A) 0 %, B) 1 %, C) 2 %, D) 5 %, and E) 10 %

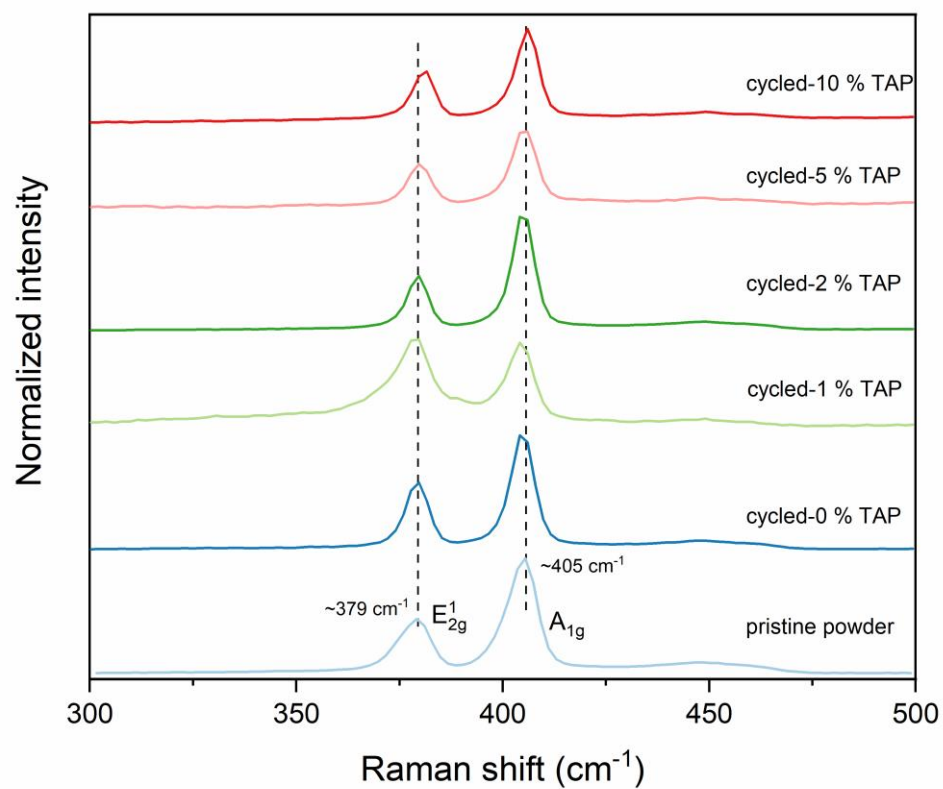


Figure S12: **Structural analysis of MoS<sub>2</sub> electrodes ensuing galvanostatic cycling in concentrated electrolytes, related to Figure 3:** The Raman spectra for MoS<sub>2</sub> electrodes cycled in 6 m KTFSI-DMC electrolytes containing different amounts of TAP additives

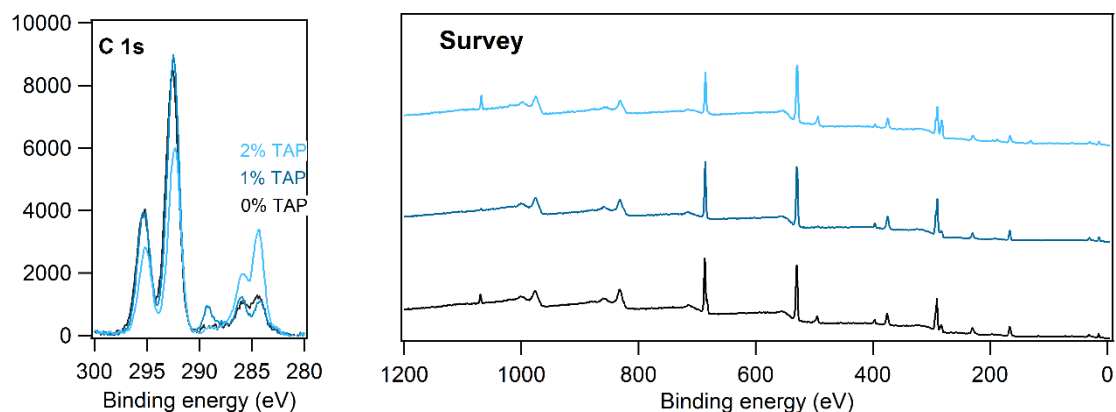


Figure S13: **The nature of the SEI on MoS<sub>2</sub> electrodes cycled in concentrated electrolyte 6 m KTFSI DMC with 0, 1, and 2 % TAP additives, related to Figure 3:** The C 1s core-level and survey spectra of MoS<sub>2</sub> electrode cycled in 6 m KTFSI in DMC with 0, 1 and 2 % TAP additive and retrieved at the discharged state after 2 cycles.

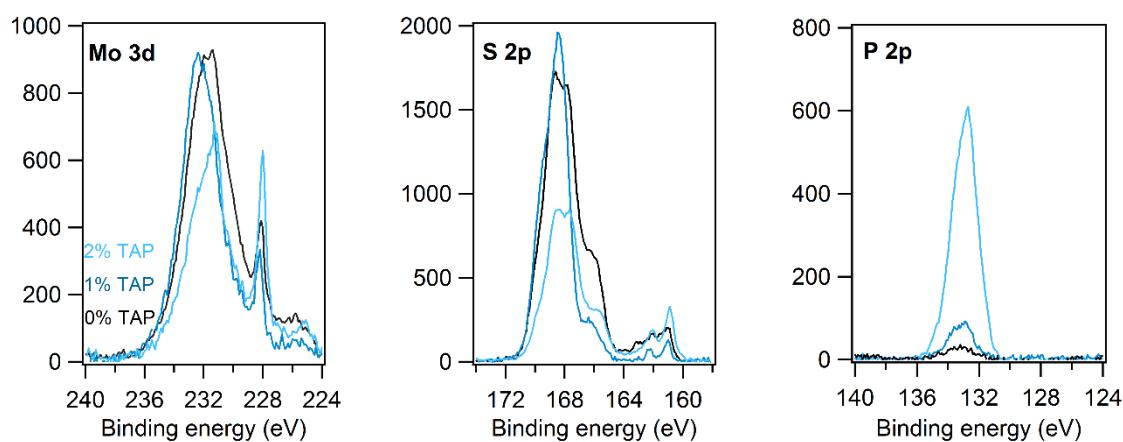


Figure S14: **The nature of the SEI on MoS<sub>2</sub> electrodes cycled in concentrated electrolyte 6 m KTFSI DMC with 0, 1, and 2 % TAP additives, related to Figure 3:** The Mo 3d, S 2p and P 2p core-level spectra of MoS<sub>2</sub> electrode cycled in 6 m KTFSI in DMC with 0, 1 and 2 % TAP additive and retrieved at the discharged state after 2 cycles.

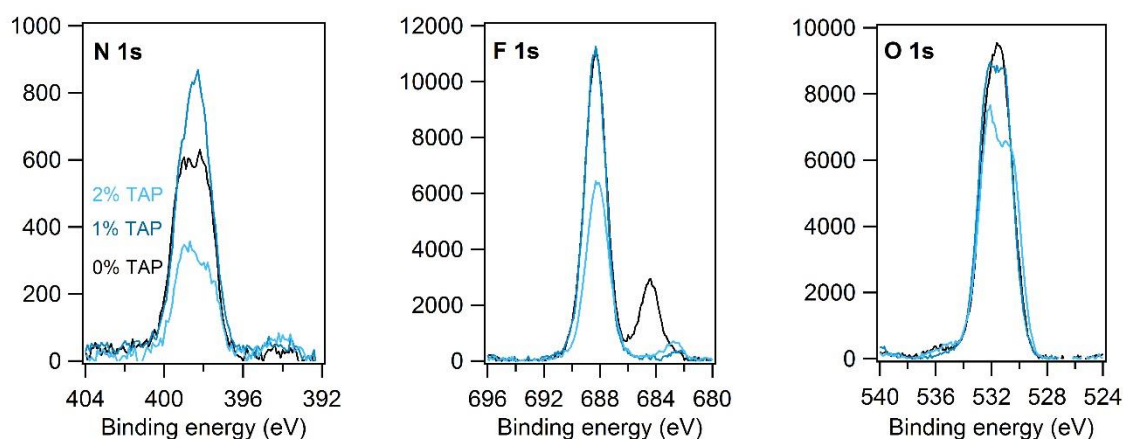


Figure S15: **The nature of the SEI on MoS<sub>2</sub> electrodes cycled in concentrated electrolyte 6 m KTFSI DMC with 0, 1, and 2 % TAP additives, related to Figure 3:** The N 1s, F 1s and O 1s core-level spectra of MoS<sub>2</sub> electrode cycled in 6 m KTFSI in DMC with 0, 1 and 2 % TAP additive and retrieved at the discharged state after 2 cycles.

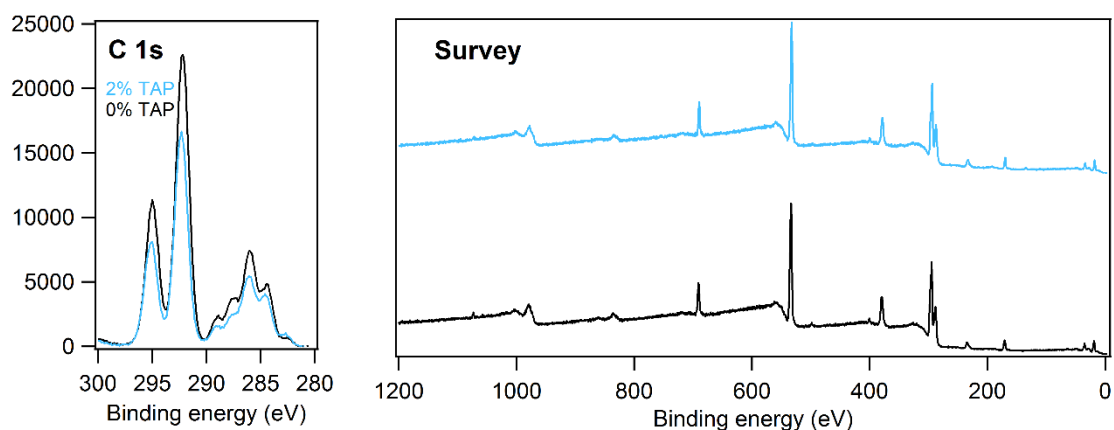


Figure S16: **Evaluation of how the TAP additives affect the SEI layer on pre-cycled MoS<sub>2</sub> electrodes, related to Figure 2 and Figure 3:** The C 1s core-level and survey spectra of pre-cycled MoS<sub>2</sub> electrode cycled in 6 m KTFSI in DMC with 0 and 2 % TAP additive and extracted at the discharged state after 10 cycles.

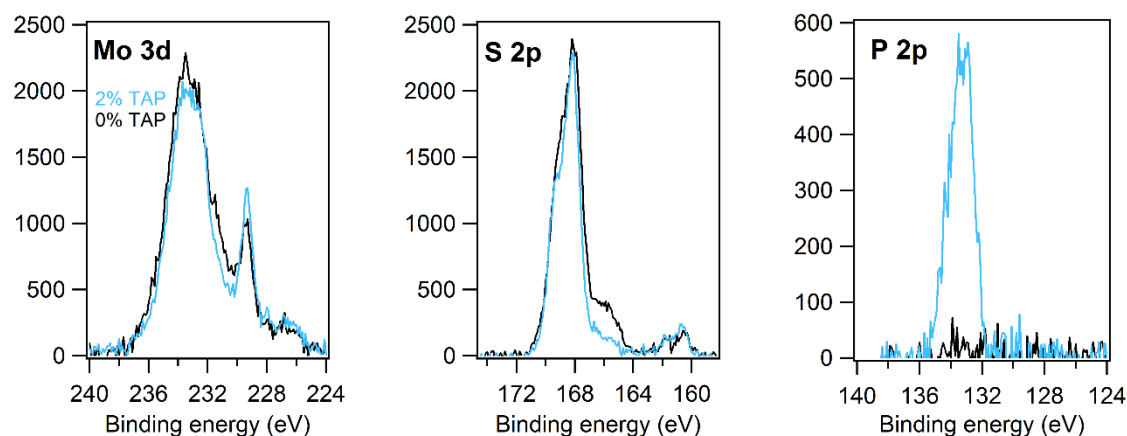


Figure S17: **Evaluation of how the TAP additives affect the SEI layer on pre-cycled MoS<sub>2</sub> electrodes, related to Figure 2 and Figure 3:** The Mo 3d, S 2p and P 2p core-level spectra of pre-cycled MoS<sub>2</sub> electrode cycled in 6 m KTFSI in DMC with 0 and 2 % TAP additive after 10 cycles.

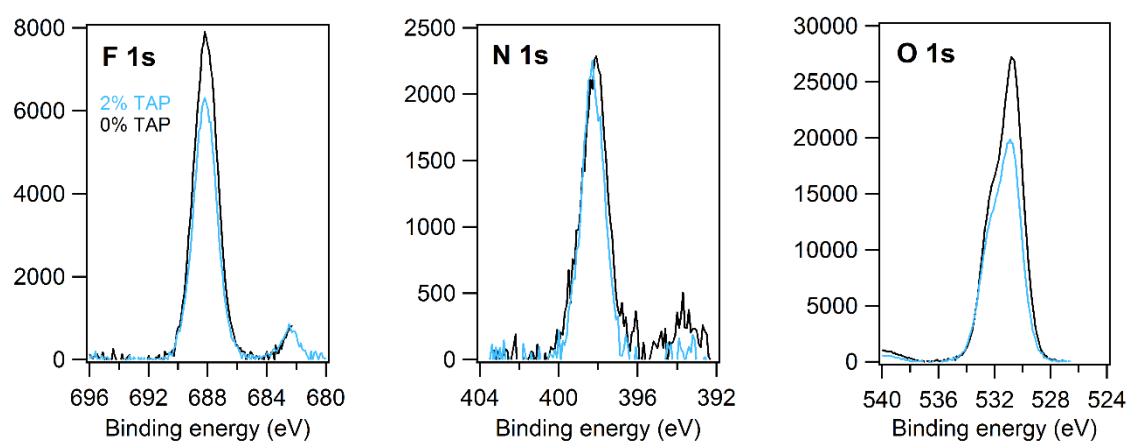


Figure S18: **Evaluation of how the TAP additives affect the SEI layer on pre-cycled MoS<sub>2</sub> electrodes, related to Figure 2 and Figure 3:** The N 1s, F 1s and O 1s core-level spectra of MoS<sub>2</sub> electrode cycled in 6 m KTFSI in DMC with 0 and 2 % TAP additive and extracted at the discharged state after 10 cycles.

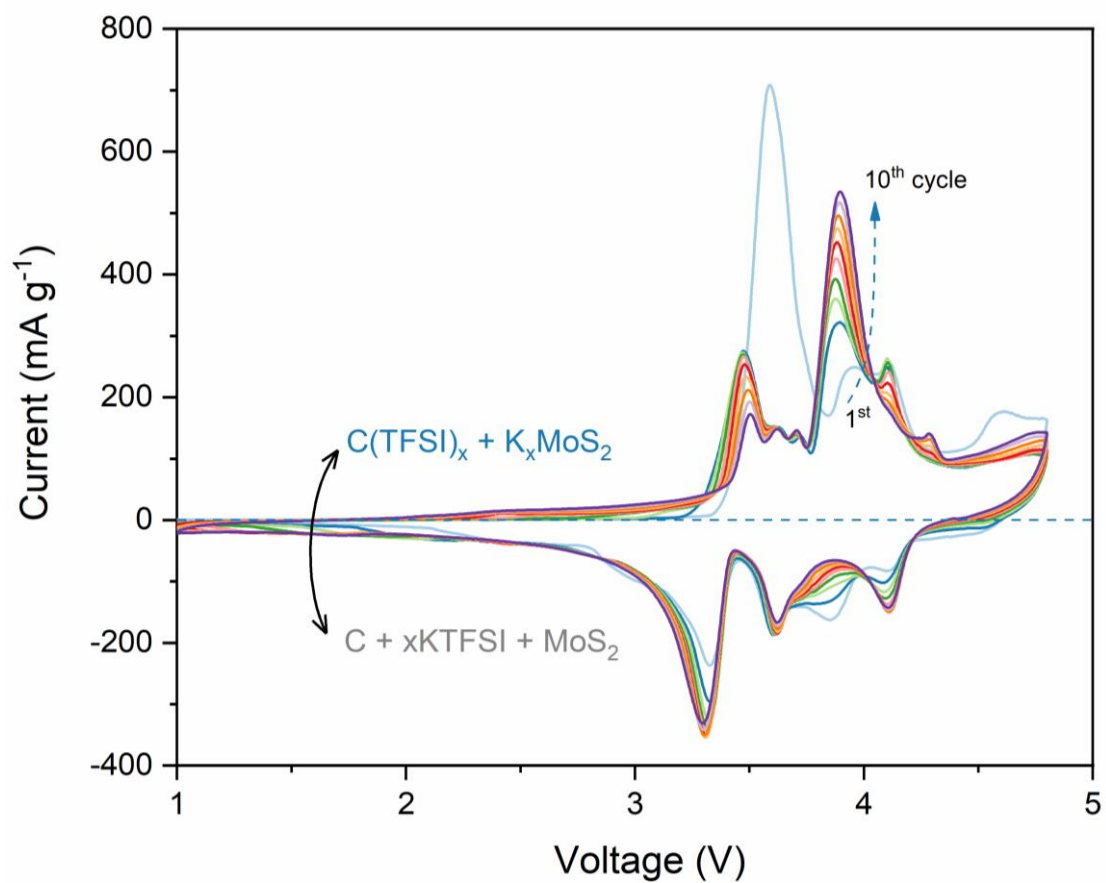


Figure S19: **Electrochemical characterization of a full-cell KDIB in 6 m KTFSI in DMC electrolyte, related to Figure 4 and Figure 5:** Cyclic voltammograms for 10 cycles of a full-cell dual-ion battery in 6 m KTFSI in DMC measured at a scan rate of  $1 \text{ mV s}^{-1}$

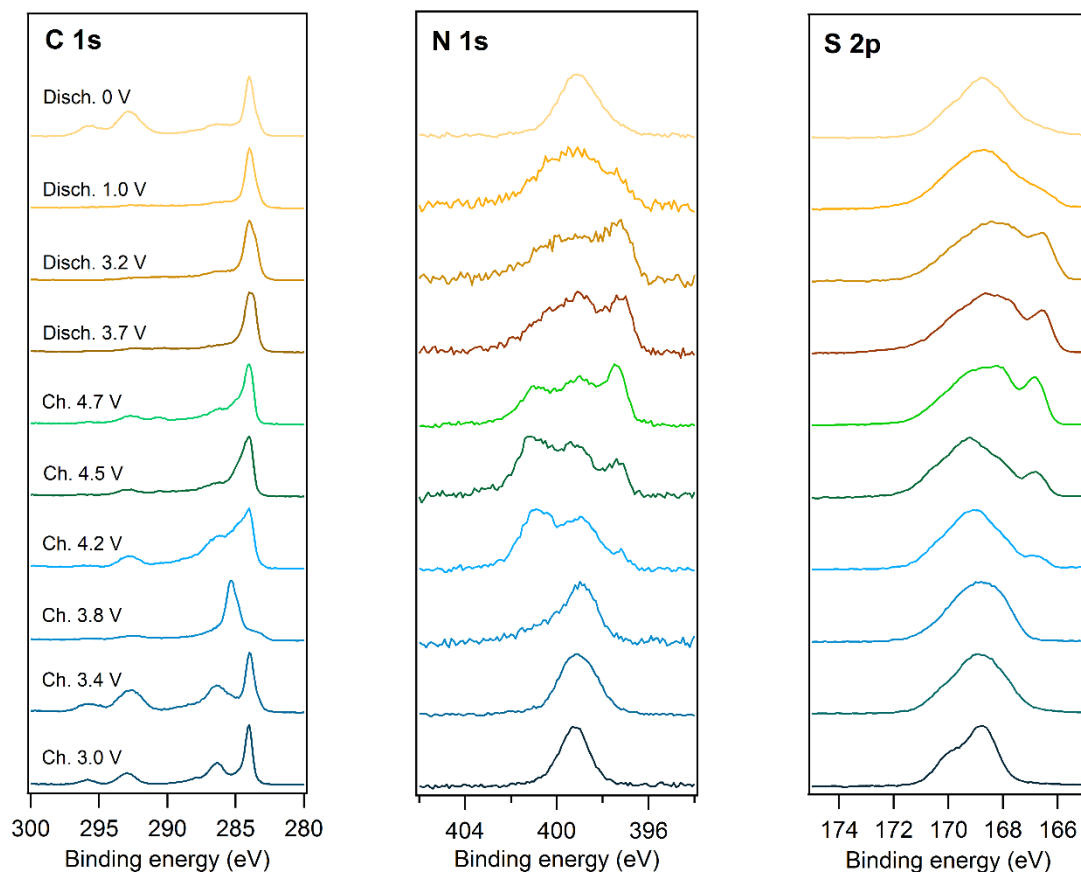


Figure S20: **X-ray photoelectron spectra of TFSI-intercalated natural graphite electrodes, related to Figure 4:** The C 1s, N 1s and S 2p core-level spectra of graphite cathodes cycled in 6 m KTFSI in DMC and extracted at different potentials during the first charge and discharge. Systematic changes are observed in the spectra of both the graphite host and the TFSI anion, which are attributed to differences in the chemical environment of the anion in the intercalated, intermediate and de-intercalated states.

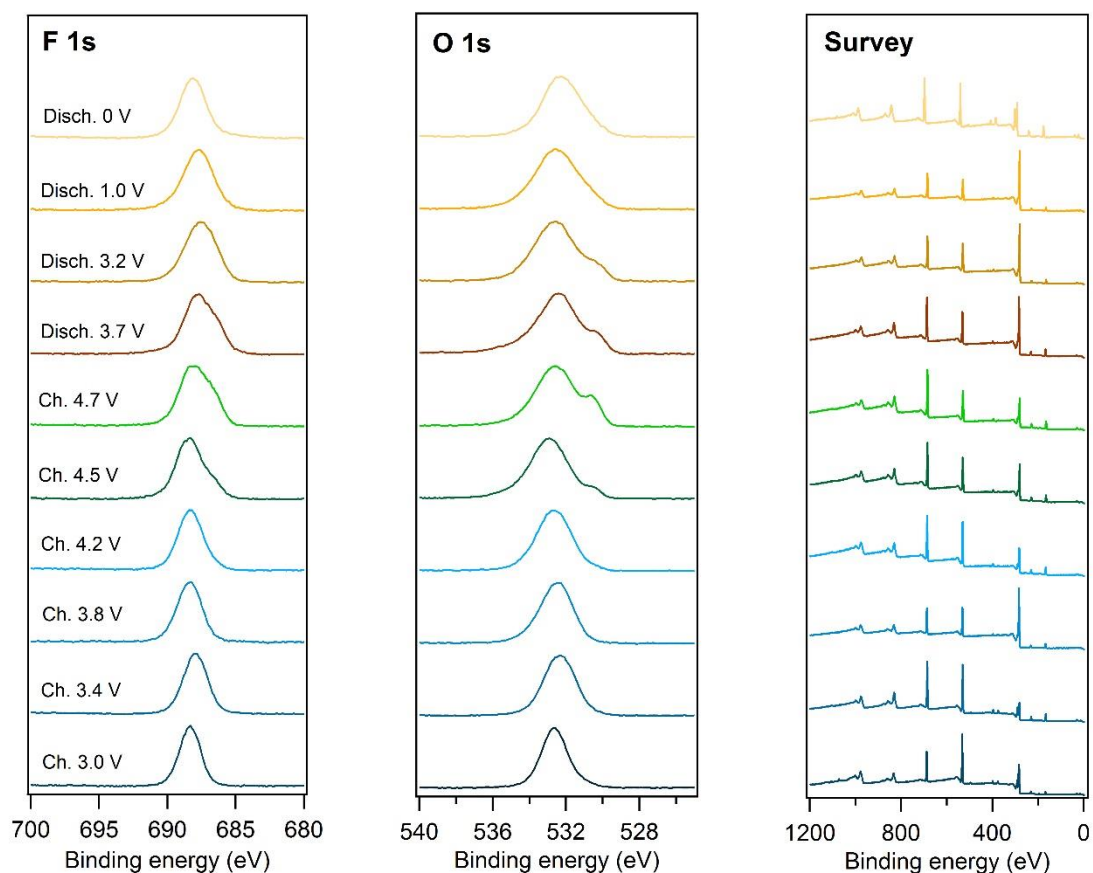


Figure S21: **X-ray photoelectron spectra of TFSI-intercalated natural graphite electrodes, related to Figure 4:** The F 1s, O 1s core-level spectra and survey spectra of graphite cathodes cycled in 6 m KTFSI in DMC and extracted at different potentials during the first charge and discharge.

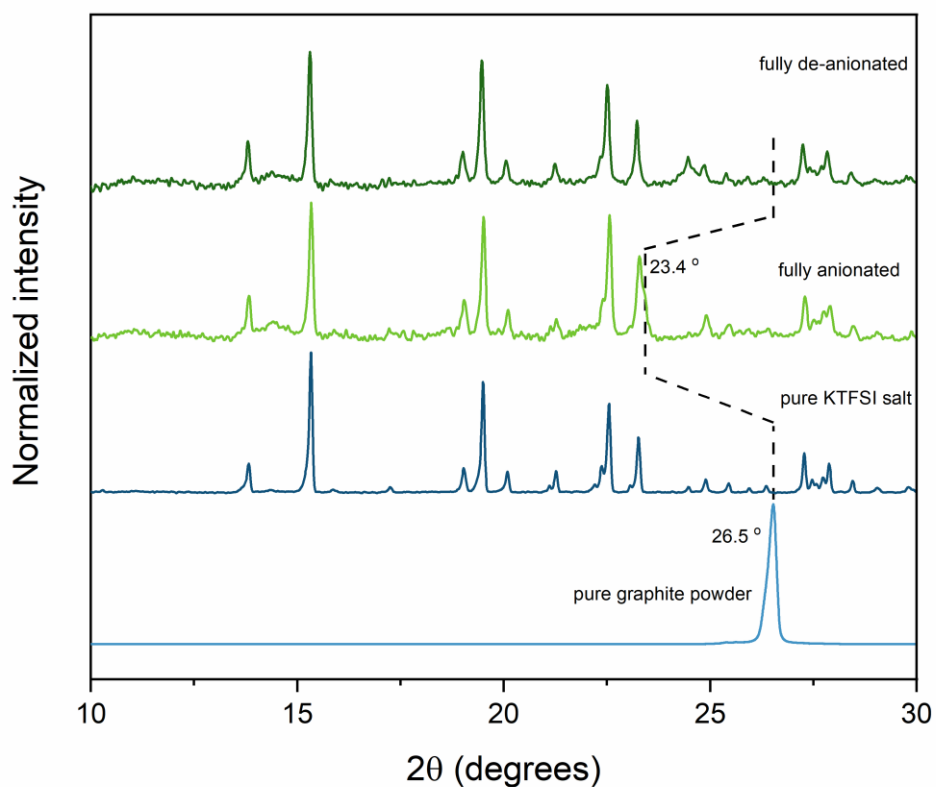


Figure S22: **Using X-ray diffraction to track structural changes involved during TFSI anion intercalation and extraction in graphite electrodes retrieved from KDIB full-cells, related to Figure 4:** XRD patterns of pure graphite powder, KTFSI powder, anionated graphite and de-anionated graphite. While most reflections originate in the presence of KTFSI salt trace, an intensity increase is observed at  $22.0^\circ$ ,  $23.4^\circ$  and  $34.1^\circ$  for the graphite electrode extracted at the fully charged state, indicating the formation of TFSI-intercalated graphite.<sup>1</sup>

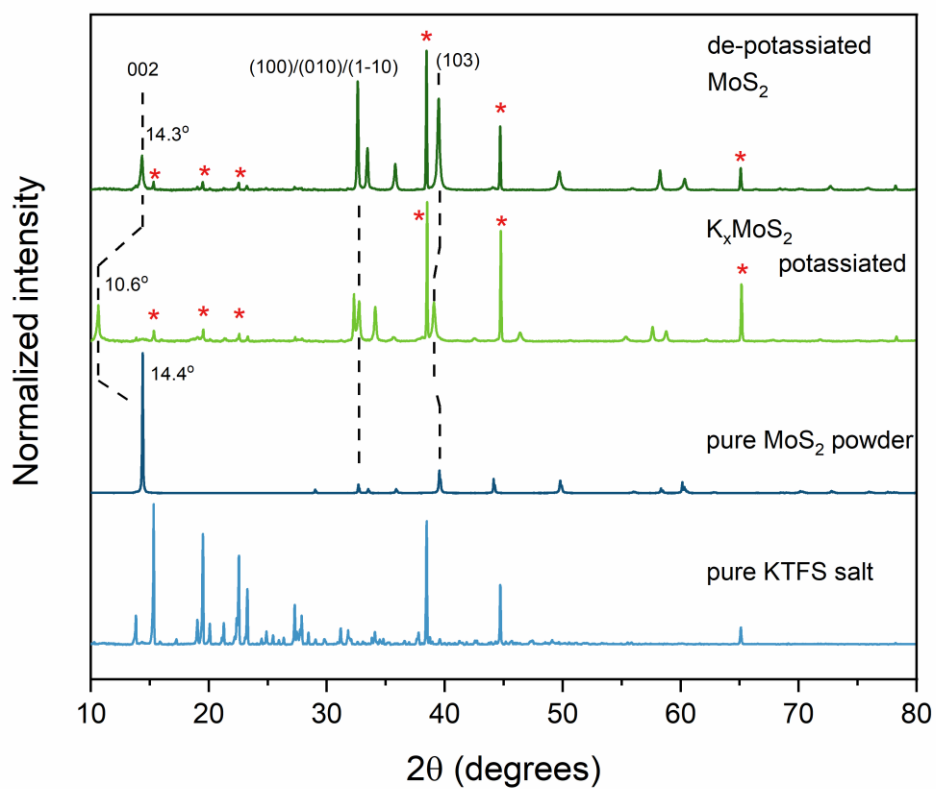


Figure S23: **Using X-ray diffraction to track structural changes involved during potassium-ion intercalation and extraction in  $\text{MoS}_2$  electrodes retrieved from KDIB full-cells, related to Figure 4:** XRD patterns of negative electrodes extracted at the fully charged and discharged states, indicating the reversible formation of the  $\text{K}_x\text{MoS}_2$  and  $\text{MoS}_2$ . The '\*'s represent diffraction peaks from the salt.

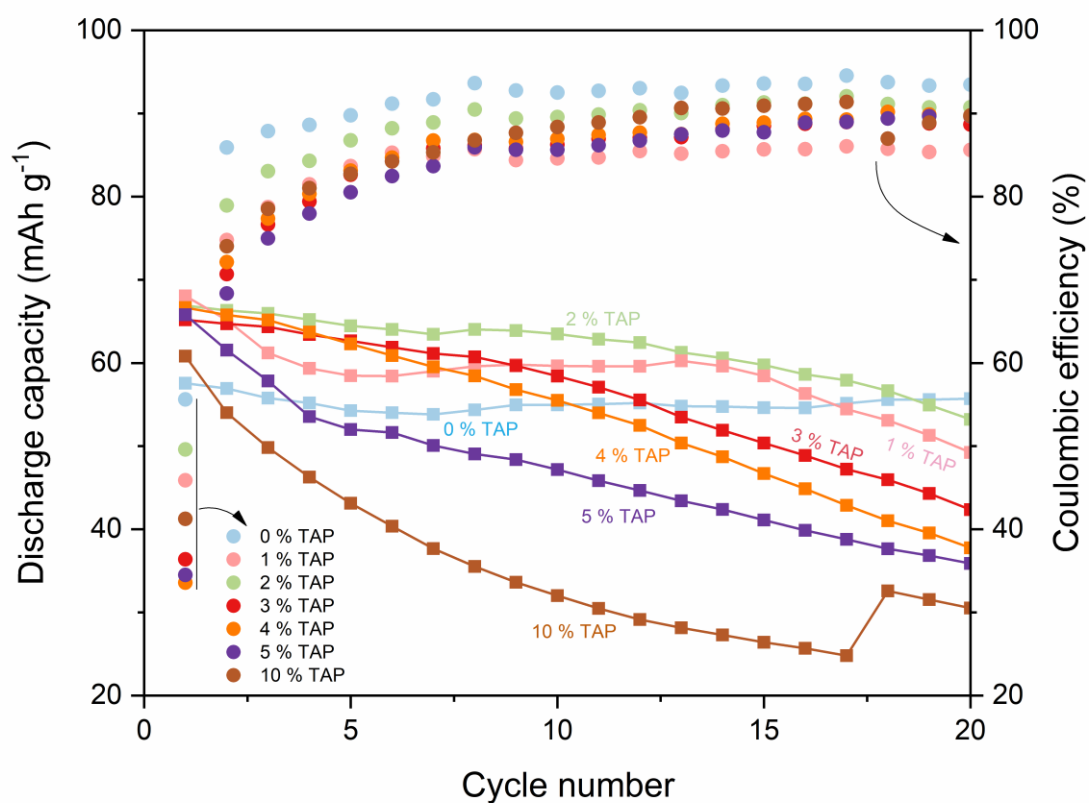


Figure S24: **Impact of TAP additive on the galvanostatic cycling of full-cell KDIB with pre-cycled MoS<sub>2</sub> electrodes, Figure 5:** The specific discharge capacity and coulombic efficiency values of full-cell KDIBs employing 6 m KTFSI-DMC with 0-10 weight % of TAP additives. The corresponding galvanostatic curves for the 1<sup>st</sup>, 2<sup>nd</sup>, and 10<sup>th</sup> cycles are shown in Figure 5A-C. The cells were cycled between 1 and 4.5 V.

**Note S1: Distribution relaxation times, related to Figure 5 F-H and Figure S21-S23**

The method of the distribution of relaxation times (DRT) derived from impedance measurements allows for separation of electrochemical processes on the basis of their different time constants, and simplifies interpretation of EIS data without fitting to physics-based models. The impedance data is expressed as an integral equation

$$Z(\omega) = R_o + R_p \int_0^{\infty} \frac{\Gamma(\tau)}{1 + j\omega\tau} d\tau$$

where  $\Gamma(\tau)$  represents the distribution of relaxation times. The polarization resistance  $R_p$  can be calculated as

$$R_p = \int \Gamma(\tau) d\tau$$

by integrating the area under the DRT peaks.

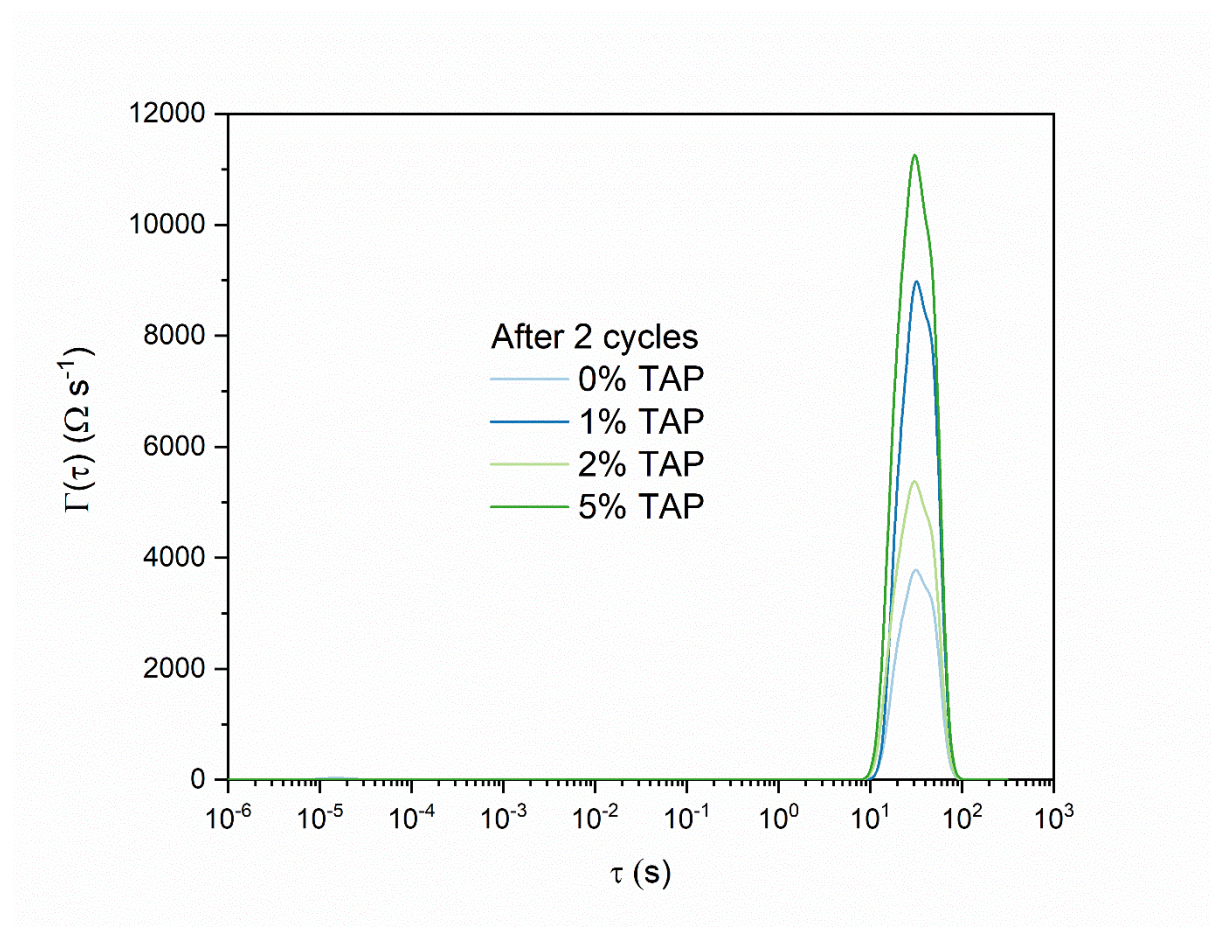


Figure S25: **The distribution functions of relaxation times (DRT) plots obtained from the EIS measurements on graphite electrodes after 2 cycles, related to Figure 5: The complete DRT data for the plots shown in Figure 5H.**

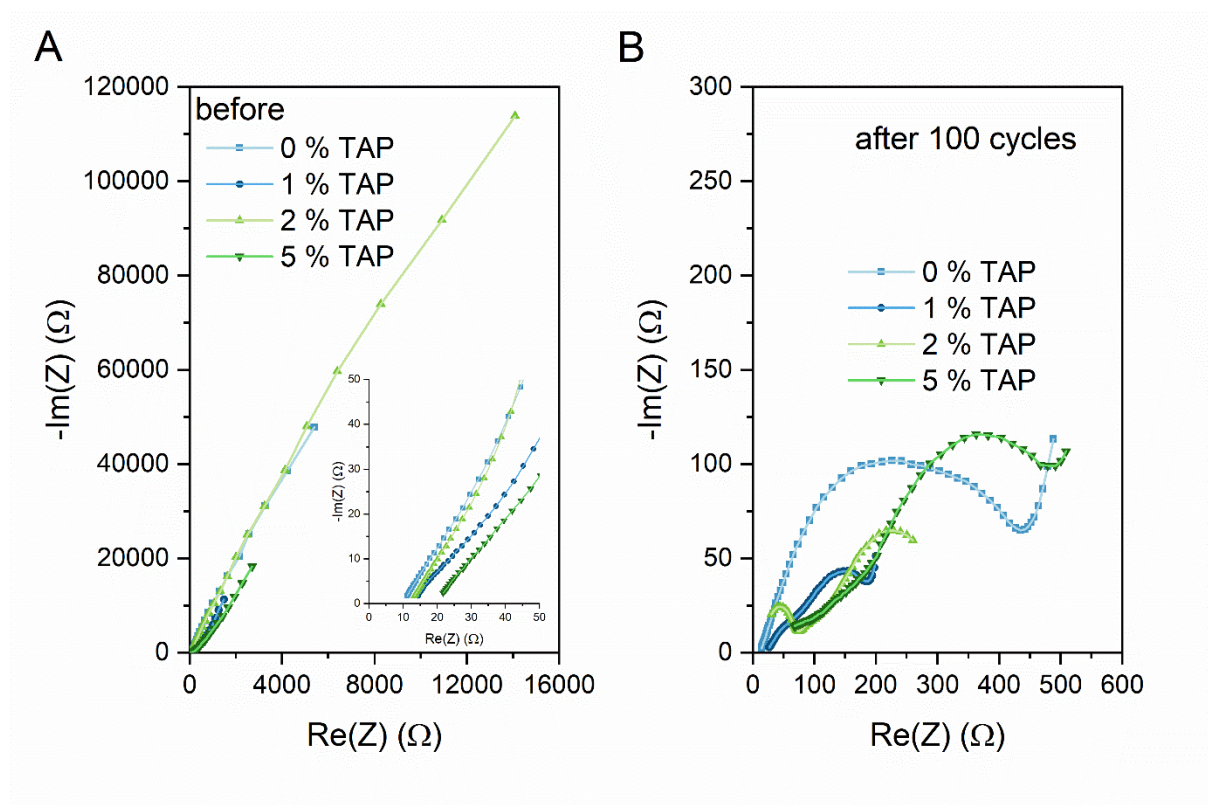


Figure S26: The EIS measurements on 2-electrode full-cell KDIBs after 100 charge-discharge galvanostatic cycles at  $50 \text{ mA g}^{-1}$  in 6 m KTFSI DMC electrolyte with different amounts of TAP additives, *related to Figure 5*: Nyquist diagrams of cells (A) before galvanostatic cycling, and (B) after 100 cycles

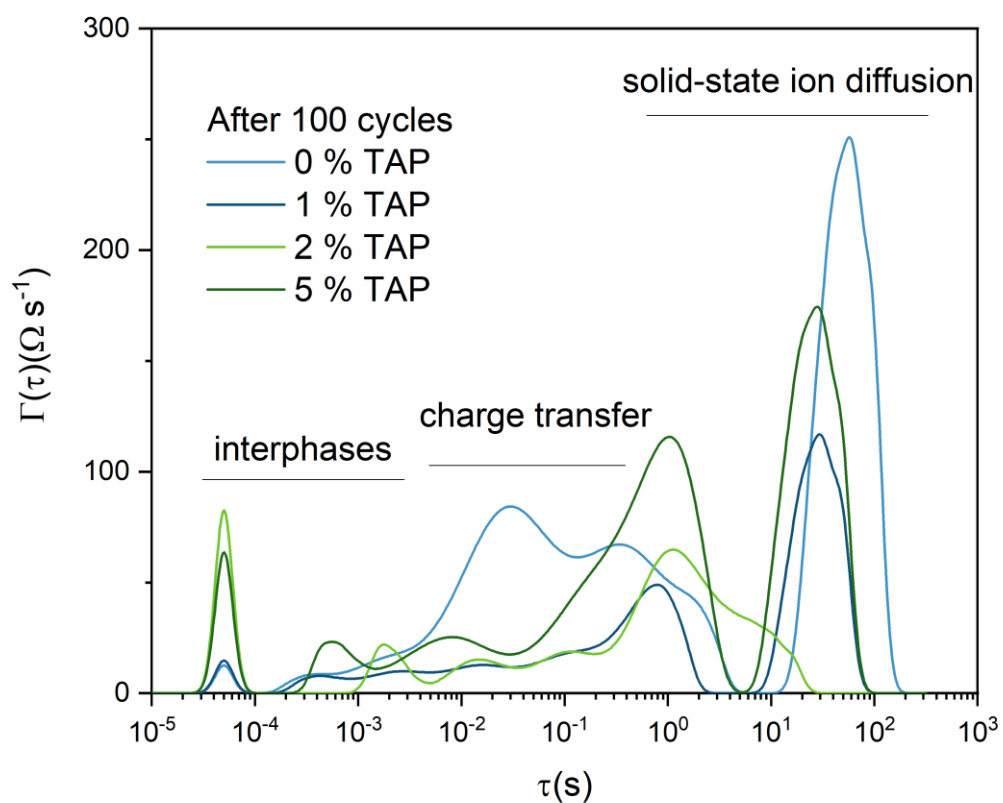


Figure S27: **The distribution functions of relaxation times (DRT) plots obtained from the EIS measurements on MoS<sub>2</sub>-graphite full-cell KDIB after 100 cycles, related to Figure 5:** DRT plots obtained for the EIS data in Figure S22

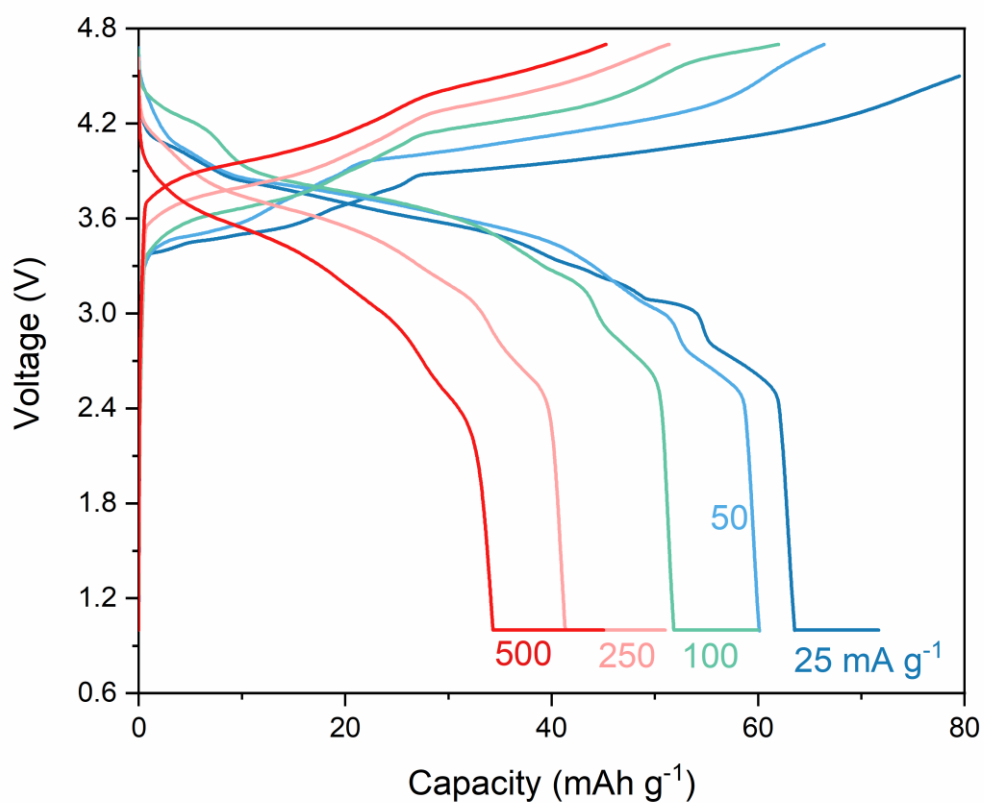


Figure S28: Rate capability tests on the MoS<sub>2</sub>-natural graphite KDIB using a 6 m KTFSI DMC electrolyte containing 2 % TAP, related to Figure 6: The galvanostatic curves for the full-cell KDIB cycled at 25 to 500 mA g<sup>-1</sup>

Table S1: Electrochemical performance of potassium-based dual-ion batteries with various active materials and electrolytes

Cell type	Positive electrode	Negative Electrode	Electrolyte	Average discharge voltage (V) or voltage range (V) vs K <sup>+</sup> /K	Capacity (mAh g <sup>-1</sup> )/current (mA g <sup>-1</sup> )	Coulombic efficiency (%) (cycle number)	References
Half-cell	Natural graphite flakes (Alfa Aesar®)	Potassium metal	5 M KFSI in DMC-EC (1:1 v/v)	4.7	~98/50	~90 (1 <sup>st</sup> ), ~96 (2 <sup>nd</sup> ) and ~99 (5 <sup>th</sup> )	2
Half-cell	Graphite flakes	Potassium metal	0.3 M KFSI+0.5 M KPF <sub>6</sub> in DMC-EC-EMC (2:3:5 by weight)	4.65	~100/50	~77 (1 <sup>st</sup> ), ~82 (2 <sup>nd</sup> ) and ~97 (50 <sup>th</sup> )	3
Half-cell	Graphite	Potassium metal	5.2 m KFSI in tetramethylene sulfone	3 to 5.4	~84/200	~91	4
Full-cell	Nano-graphite	Nano-graphite	0.8 M KPF <sub>6</sub> in DMC-EC (1:1 v/v)	3.96	~62/100	~60 (2 <sup>nd</sup> ), ~80 (10 <sup>th</sup> ) and ~90 (20 <sup>th</sup> )	5
Full-cell	Synthetic graphite (KS6L, Imerys®)	Synthetic graphite (KS6L, Imerys®)	3.5 M KFSI in EMC	3.4 to 5	~50/50	~70 (1 <sup>st</sup> ), ~85 (2 <sup>nd</sup> ) and ~95 (200 <sup>th</sup> )	6
Full-cell	Expanded graphite	Meso-carbon micro-bead	1 M KPF <sub>6</sub> in DMC-EC-EMC (4:3:2 by volume)	4.5	~61/100	~40 (1 <sup>st</sup> ), ~50 (2 <sup>nd</sup> ), ~70 (10 <sup>th</sup> ), and ~95 (100 <sup>th</sup> )	7
Full-cell	Synthetic graphite (KS6L, Imerys®)	Synthetic graphite (KS6L, Imerys®)	Pyr <sub>14</sub> TFSI + 0.3 M KTFSI + 2 wt% ethylene sulfite	3.4 to 5	~47/50	~65 (1 <sup>st</sup> ), ~81(2 <sup>nd</sup> ), and ~97(50 <sup>th</sup> )	8
Full-cell	Expanded graphite	Sn foil	1 M KPF <sub>6</sub> in DMC-EC-EMC (3:4:2 by volume)	3 to 5	~67/50	~43 (1 <sup>st</sup> ), ~50(2 <sup>nd</sup> ), and ~85(300 <sup>th</sup> )	9
Full-cell	Graphite	Sn foil	6.6 molal KFSI in trimethyl phosphate	4 or 3 to 5.2	~96/200	~70 (1 <sup>st</sup> ), ~70(2 <sup>nd</sup> ), and ~75(10 <sup>th</sup> )	10
Full-cell	Graphite	Hard carbon	0.8 M KPF <sub>6</sub> in DEC-EC (1:1 v/v)	3.75 or 3 to 5	~67/100	NA (1 <sup>st</sup> ), ~84(2 <sup>nd</sup> ), and ~98(100 <sup>th</sup> )	11
Full-cell	Expanded graphite	Dipotassium terephthalate	1 M KPF <sub>6</sub> in DMC-EC-EMC (3:4:2 by volume)	2 or 0.5 to 4	~68/200	~80-85	12
Full-cell	Graphite	Graphite	5.2 m KFSI in tetramethylene sulfone	4.25 or 3 to 5.4	~83/100	~85-89	4
Full-cell	Graphite	MoS <sub>2</sub> flakes	6 m KTFSI in DMC + 1 to 5 weight % triallyl phosphate	3.7 or 1 to 4.7	~60-75/50	~53-57 (1 <sup>st</sup> ), ~95-97(20 <sup>th</sup> ), and ~97-98(100 <sup>th</sup> )	THIS WORK

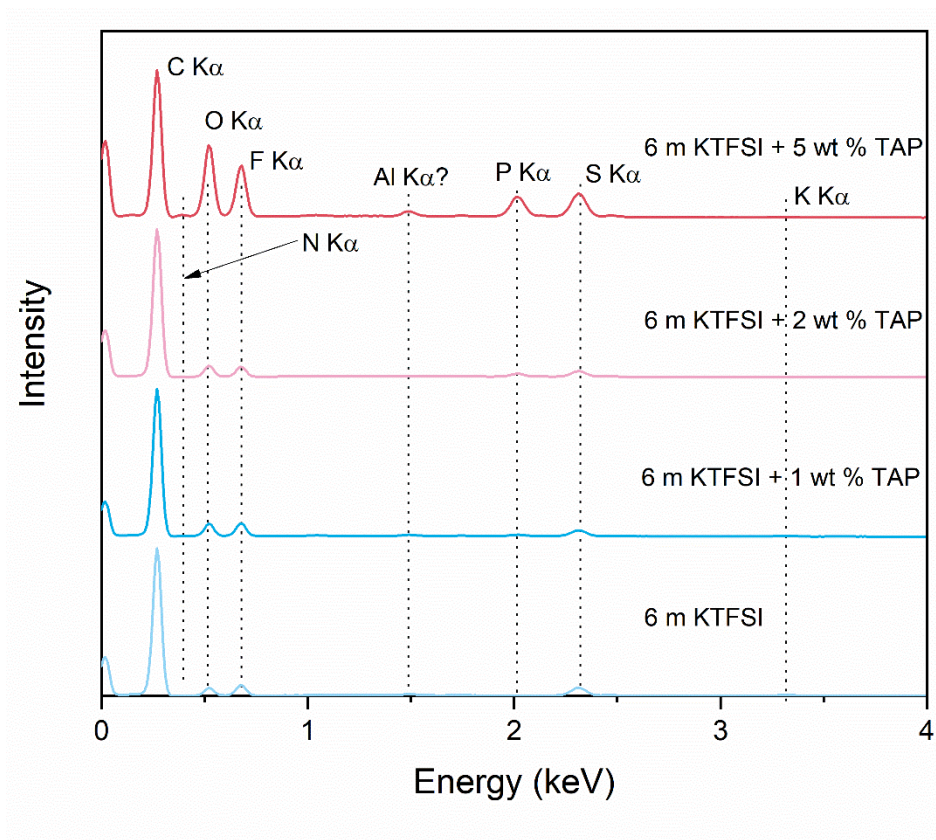


Figure S29: **Elemental composition of the surface of graphite electrodes cycled in concentrated electrolytes, related to Figure 7:** EDX spectra of graphite electrodes after 100 cycles in 6 m KTFSI-DMC electrolytes with and without TAP additives

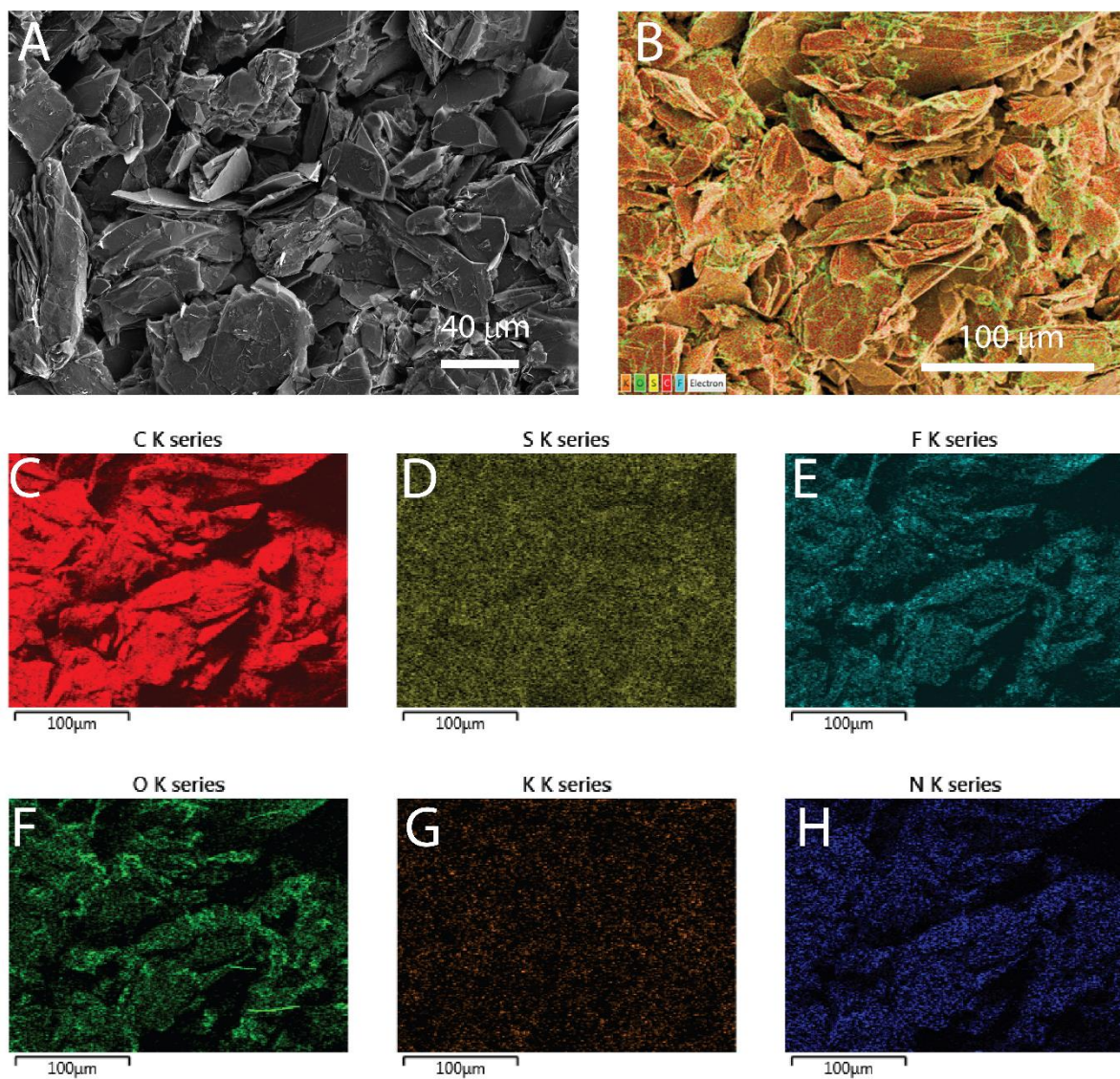


Figure S30: **Elemental composition and morphological features of graphite electrodes cycled in 6 m KTFSI-DMC with no additive, related to Figure 7:** A) SEM image, (B) SEM image with EDX maps overlaid, EDX elemental distribution of (C) carbon (D) sulfur, (E) fluorine, (F) oxygen, (G) potassium, and (H) nitrogen

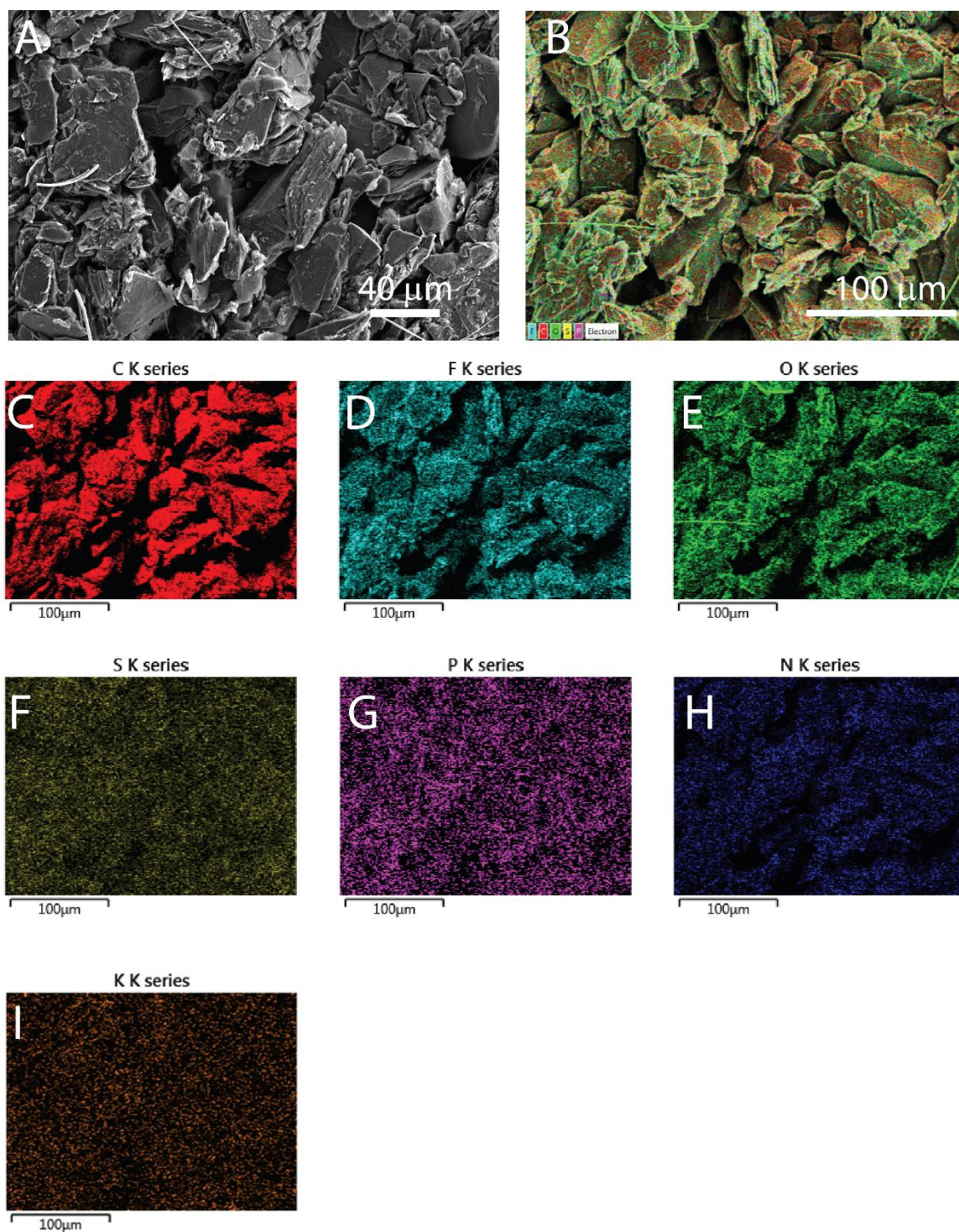


Figure S31: **Elemental composition and morphological features of graphite electrodes cycled in 6 m KTFSI-DMC with 1 wt % TAP additive, related to Figure 7:** A) SEM image, (B) SEM image with EDX maps overlaid, EDX elemental distribution of (C) carbon (D) sulfur, (E) fluorine, (F) oxygen, (G) phosphorus, (H) nitrogen, and (I) potassium

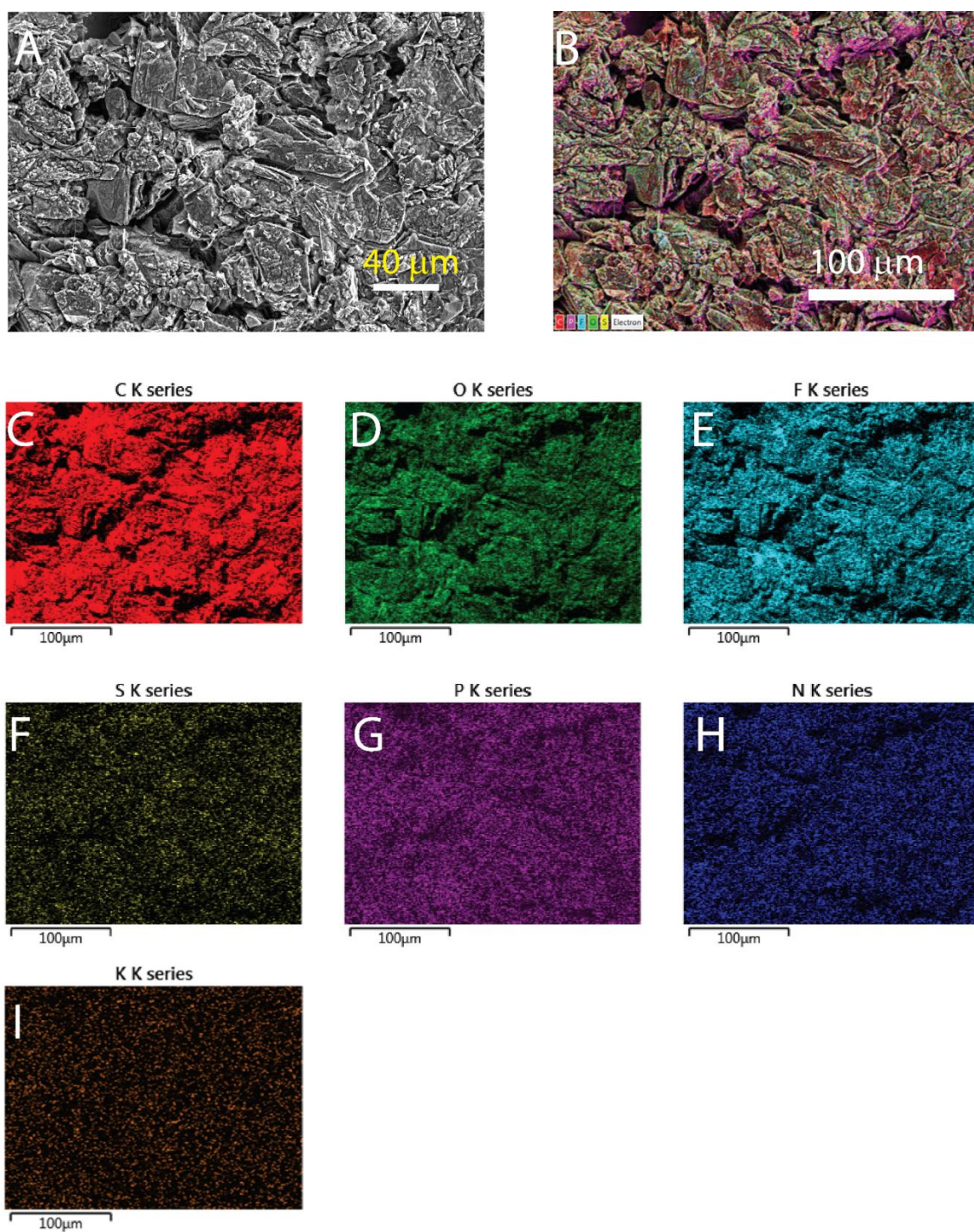


Figure S32: **Elemental composition and morphological features of graphite electrodes cycled in 6 m KTFSI-DMC with 5 wt % TAP additive, related to Figure 7:** A) SEM image, (B) SEM image with EDX maps overlaid, EDX elemental distribution of (C) carbon (D) sulfur, (E) fluorine, (F) oxygen, (G) phosphorus, (H) nitrogen, and (I) potassium

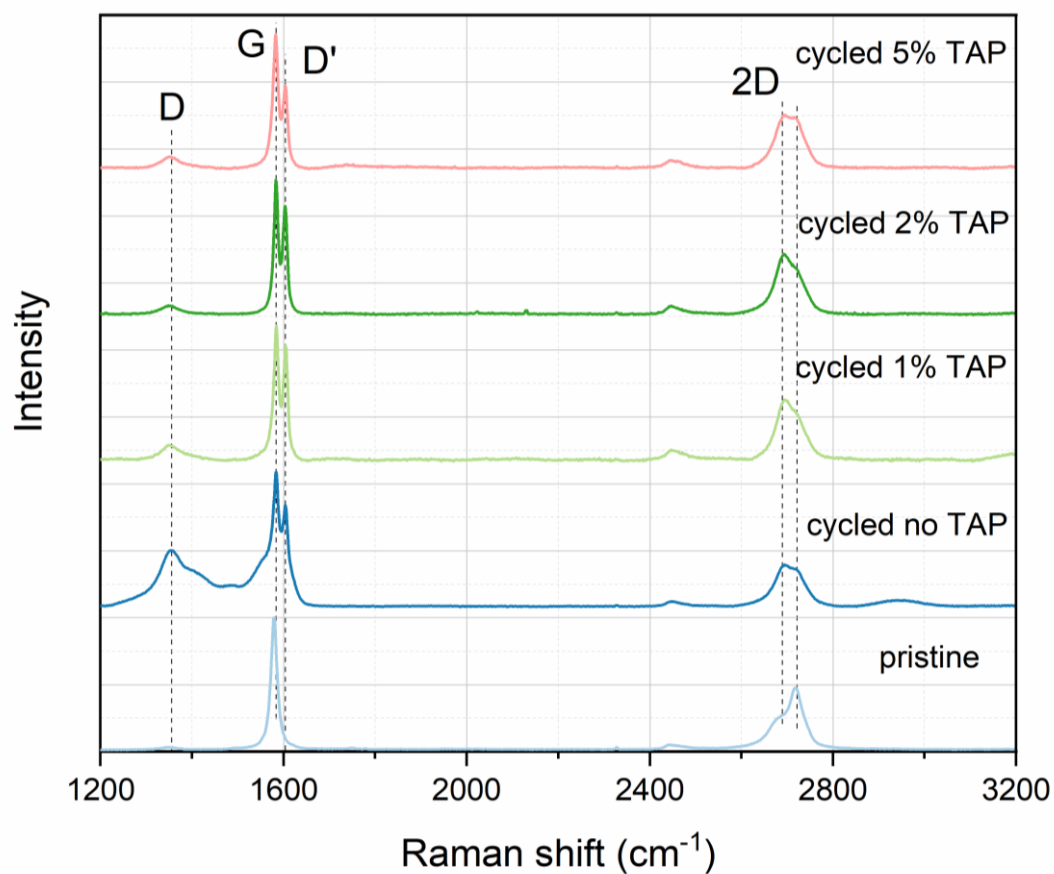


Figure S33: **Analysis of structural changes in natural graphite after cycling in 6 m KTFSI with and without TAP additives, related to Figure 5 and Figure 7:** Raman spectra of graphite electrodes after 100 cycles showing impact of extended cycling on the structure of graphite

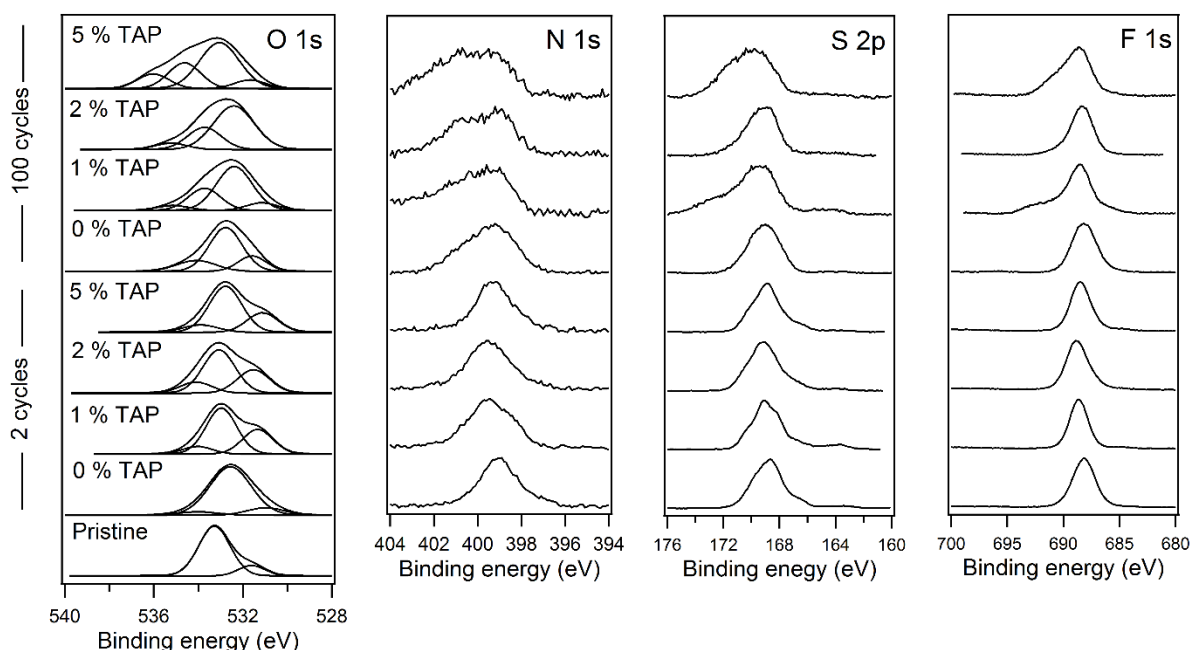


Figure S34: **A triallyl phosphate additive forms a polymeric CEI on graphite particles based on XPS analyses which helped explore the impact of different amounts of TAP additives in 6 m KTFSI-DMC electrolyte on the nature of the CEI formed on graphite electrodes, Figure 8:** The O1s, N1s, S2p and F 1s XPS of pristine graphite electrodes and electrodes extracted after 2 and 100 cycles

**Note S2: Evaluation of CEI thickness on cycled graphite based on XPS data, related to Figure 8:**

A rough estimate of the CEI layer thickness can be computed using empirical relation developed for oxide and polymer thin films on flat substrates<sup>13,14</sup>:

$$d = \lambda_{CEI} \sin(\theta) \ln \left( \frac{N_{sub} \lambda_{sub} I_{CEI}}{N_{CEI} \lambda_{CEI} I_{sub}} + 1 \right)$$

where  $\lambda_{CEI}$  and  $\lambda_{sub}$  stand for, respectively, the inelastic mean free path (IMFP) in the CEI layer and the graphite substrate,  $I_{CEI}$  and  $I_{sub}$  are the intensities of the CEI and graphite peaks,  $N_{CEI}$  and  $N_{sub}$  are the densities of the CEI and graphite layers, and  $\theta$  represents the photoelectron emission angle. IMFP values were extracted from the NIST database.<sup>15</sup> Since the CEI is non-uniform and no data is provided specifically for poly(triallyl phosphate) data available for polyethylene were used in the calculation. The IMFP for polyethylene is 4.36 nm<sup>16,17</sup>. For graphite the IMFP values determined by Gries et al., 2.24 nm<sup>18</sup>, and Lesiak et al., 2.84 nm<sup>19</sup> can be used in the calculation. The densities of the organic CEI was set to 0.94 g cm<sup>-3</sup> (same as for polyethylene) and for graphite to 2.2 g cm<sup>-3</sup>. The emission angle is 90°. The integrated area of the C 1s peak in the CEI layer is compared to that of the graphite substrate (see table below).

Sample	C-H (counts)	Graphite (counts)
2 cycles, 0 % TAP	111141	377365
2 cycles, 2 % TAP	188694	133394
100 cycles, 0 % TAP	10062	21256
100 cycles, 2 % TAP	16904	5355

Accordingly, estimates of the CEI thickness on graphite electrodes cycled in the 6 m KTFSI-DMC electrolyte with 0 and 2% TAP after 2 and 100 cycles are, respectively, given in the following table:

Sample	CEI thickness (nm)
2 cycles, 0 % TAP	1.61
2 cycles, 2 % TAP	5.01
100 cycles, 0 % TAP	2.37
100 cycles, 2 % TAP	7.67

The calculation is further supported by sputtering experiments (with a monatomic Ar<sup>+</sup> source operated at 5 keV) shown in Figure S35 and Figure S36. Sputtering under these conditions for 100 s already results in the removal of the most part of the signal related to CEI and surface salt traces, as may be seen in the following figures. However, this energetic Ar<sup>+</sup> milling procedure damages the highly sensitive CEI and results also in the alteration of the surface composition; hence these results can only be used as qualitative evidence supporting the calculation presented previously.

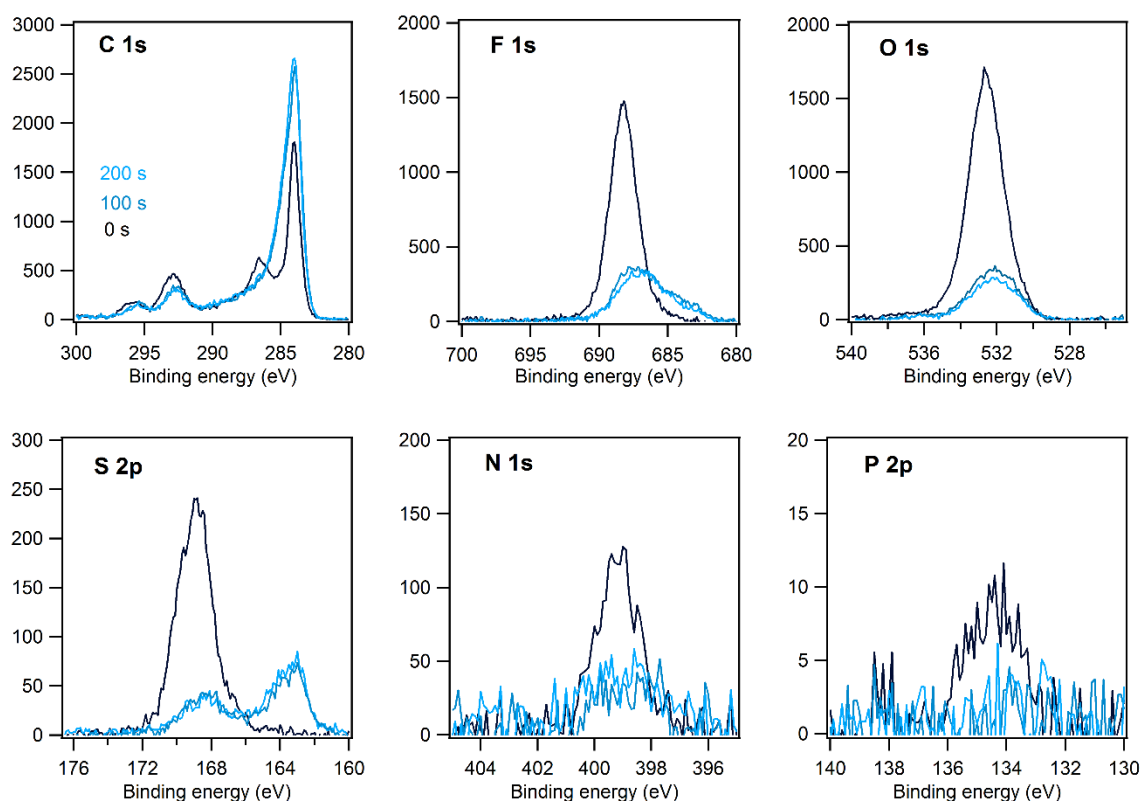


**Figure S35: Sputtering and XPS analysis of the CEI formed on graphite electrodes cycled in 6 m KTFSI DMC electrolyte with no TAP additive, related to Figure 8:** The C 1s, F 1s, O 1s, S 2p, N 1s and P 2p core-level spectra of graphite cathodes cycled in 6 m KTFSI in DMC with 0 % TAP additive and extracted at the discharged state after 2 cycles. Spectra have been recorded at the same spot prior to sputtering (0 s) and after sputtering for 100 s and 200 s.

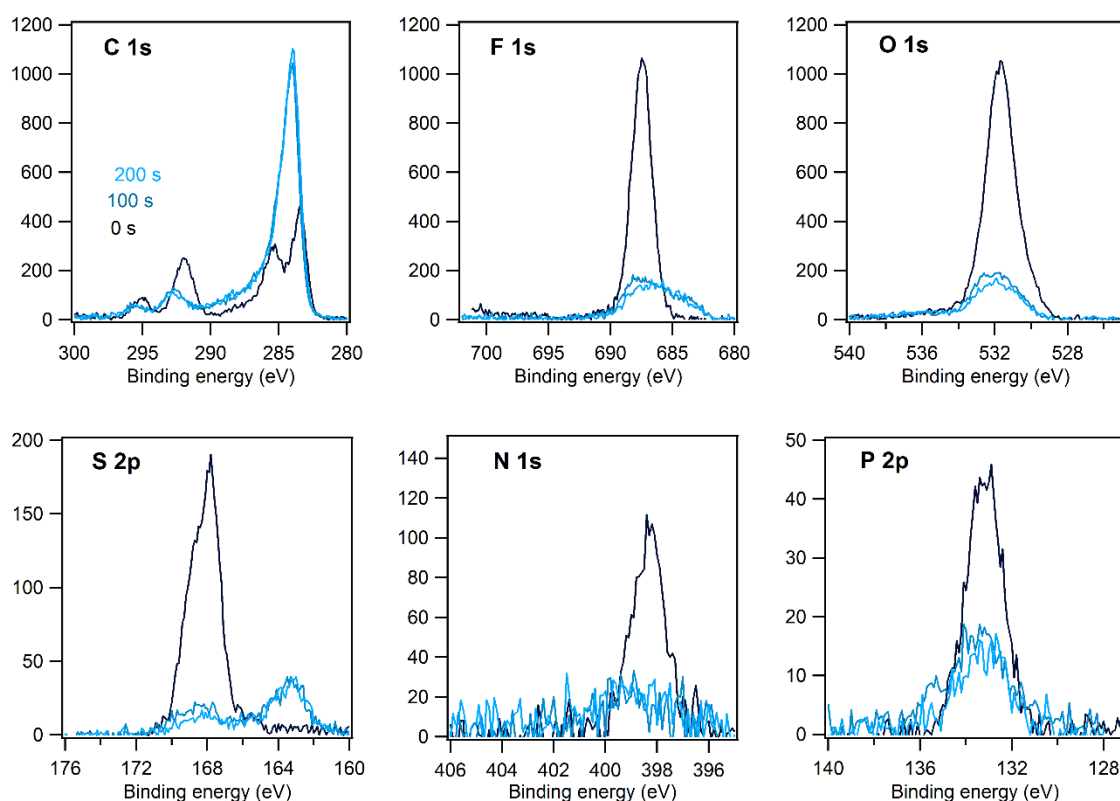


Figure S36: **Sputtering and XPS analysis of the CEI formed on graphite electrodes cycled in 6 m KTFSI DMC electrolyte with 2 % TAP additive, related to Figure 8:** The C 1s, F 1s, O 1s, S 2p, N 1s and P 2p core-level spectra of graphite cathodes cycled in 6 m KTFSI in DMC with 2 % TAP additive and extracted at the discharged state after 2 cycles. Spectra have been recorded at the same spot prior to sputtering (0 s) and after sputtering for 100 s and 200 s.

## References

1. Schmuelling, G., Placke, T., Klopsch, R., Fromm, O., Meyer, H.-W., Passerini, S., and Winter, M. (2013). X-ray diffraction studies of the electrochemical intercalation of bis(trifluoromethanesulfonyl)imide anions into graphite for dual-ion cells. *Journal of Power Sources* 239, 563-571. <https://doi.org/10.1016/j.jpowsour.2013.03.064>.
2. Kravchyk, K.V., Bhauriyal, P., Piveteau, L., Guntlin, C.P., Pathak, B., and Kovalenko, M.V. (2018). High-energy-density dual-ion battery for stationary storage of electricity using concentrated potassium fluorosulfonylimide. *Nature Communications* 9, 4469. 10.1038/s41467-018-06923-6.
3. Tan, H., Zhai, D., Kang, F., and Zhang, B. (2021). Synergistic PF<sub>6</sub><sup>-</sup> and FSI<sup>-</sup> intercalation enables stable graphite cathode for potassium-based dual ion battery. *Carbon* 178, 363-370. <https://doi.org/10.1016/j.carbon.2021.03.027>.

4. Li, X., Ou, X., and Tang, Y. (2020). 6.0 V High-Voltage and Concentrated Electrolyte toward High Energy Density K-Based Dual-Graphite Battery. *Advanced Energy Materials* 10, 2002567. <https://doi.org/10.1002/aenm.202002567>.
5. Fan, L., Liu, Q., Chen, S., Lin, K., Xu, Z., and Lu, B. (2017). Potassium-Based Dual Ion Battery with Dual-Graphite Electrode. *Small* 13, 1701011. 10.1002/smll.201701011.
6. Münster, P., Heckmann, A., Nölle, R., Winter, M., Beltrop, K., and Placke, T. (2019). Enabling High Performance Potassium-Based Dual-Graphite Battery Cells by Highly Concentrated Electrolytes. *Batteries & Supercaps* 2, 992-1006. <https://doi.org/10.1002/batt.201900106>.
7. Ji, B., Zhang, F., Wu, N., and Tang, Y. (2017). A Dual-Carbon Battery Based on Potassium-Ion Electrolyte. *Advanced Energy Materials* 7, 1700920. 10.1002/aenm.201700920.
8. Beltrop, K., Beuker, S., Heckmann, A., Winter, M., and Placke, T. (2017). Alternative electrochemical energy storage: potassium-based dual-graphite batteries. *Energy & Environmental Science* 10, 2090-2094. 10.1039/C7EE01535F.
9. Ji, B., Zhang, F., Song, X., and Tang, Y. (2017). A Novel Potassium-Ion-Based Dual-Ion Battery. *Advanced Materials* 29, 1700519. 10.1002/adma.201700519.
10. Ou, X., Li, J., Tong, X., Zhang, G., and Tang, Y. (2020). Highly Concentrated and Nonflammable Electrolyte for High Energy Density K-Based Dual-Ion Battery. *ACS Applied Energy Materials* 3, 10202-10208. 10.1021/acsaem.0c01993.
11. Chen, C., Wu, M., Wang, Y., and Zaghib, K. (2019). Insights into pseudographite-structured hard carbon with stabilized performance for high energy K-ion storage. *Journal of Power Sources* 444, 227310. <https://doi.org/10.1016/j.jpowsour.2019.227310>.
12. Yu, A., Pan, Q., Zhang, M., Xie, D., and Tang, Y. (2020). Fast Rate and Long Life Potassium-Ion Based Dual-Ion Battery through 3D Porous Organic Negative Electrode. *Advanced Functional Materials* 30, 2001440. <https://doi.org/10.1002/adfm.202001440>.
13. Alexander, M.R., Thompson, G.E., Zhou, X., Beamson, G., and Fairley, N. (2002). Quantification of oxide film thickness at the surface of aluminium using XPS. *Surface and Interface Analysis* 34, 485-489. <https://doi.org/10.1002/sia.1344>.
14. Ton-That, C., Shard, A.G., and Bradley, R.H. (2000). Thickness of Spin-Cast Polymer Thin Films Determined by Angle-Resolved XPS and AFM Tip-Scratch Methods. *Langmuir* 16, 2281-2284. 10.1021/la990605c.
15. Powell, C.J., and Jablonski, A. (1999). NIST Electron Inelastic-Mean-Free-Path Database 71, Version 1.0.
16. Tanuma, S., Powell, C.J., and Penn, D.R. (1994). Electron Inelastic Mean Free Paths in Organic Materials

Especially for Polyethylene and Guanine. *Hyomen Kagaku* 15, 175-180. 10.1380/jsssj.15.175.

17. Tanuma, S., Powell, C.J., and Penn, D.R. (1994). Calculations of electron inelastic mean free paths. V. Data for 14 organic compounds over the 50–2000 eV range. *Surface and Interface Analysis* 21, 165-176. <https://doi.org/10.1002/sia.740210302>.
18. Gries, W.H. (1996). A Universal Predictive Equation for the Inelastic Mean Free Pathlengths of X-ray Photoelectrons and Auger Electrons. *Surface and Interface Analysis* 24, 38-50. [https://doi.org/10.1002/\(SICI\)1096-9918\(199601\)24:1<38::AID-SIA84>3.0.CO;2-H](https://doi.org/10.1002/(SICI)1096-9918(199601)24:1<38::AID-SIA84>3.0.CO;2-H).
19. Lesiak, B., Jablonski, A., Prussak, Z., and Mrozek, P. (1989). Experimental determination of the inelastic mean free path of electrons in solids. *Surface Science* 223, 213-232. [https://doi.org/10.1016/0039-6028\(89\)90735-8](https://doi.org/10.1016/0039-6028(89)90735-8).